Multifunctional Self-Assembled Monolayers for Organic Field-Effect Transistors

Nathan Cernetic

A dissertation

submitted in partial fulfillment of the

requirements for the degree of

Doctor of Philosophy

University of Washington

2016

Reading Committee:

Alex Jen, Co-Chair

Hong Ma, Co-Chair

Christine Luscombe

Program Authorized to Offer Degree:

Materials Science and Engineering

University of Washington

Abstract

Multifunctional Self-Assembled Monolayers for Organic Field-Effect Transistors

Nathan Cernetic

Chair of the Supervisory Committee:
Professor Alex Jen
Professor Hong Ma
Materials Science and Engineering

Organic field effect transistors (OFETs) have the potential to reach commercialization for a wide variety of applications such as active matrix display circuitry, chemical and biological sensing, radio-frequency identification devices and flexible electronics. In order to be commercially competitive with already at-market amorphous silicon devices, OFETs need to approach similar performance levels. Significant progress has been made in developing high performance organic semiconductors and dielectric materials. Additionally, a common route to improve the performance metric of OFETs is via interface modification at the critical dielectric/semiconductor and electrode/semiconductor interface which often play a significant role in charge transport properties. These metal oxide interfaces are typically modified with rationally designed multifunctional self-assembled monolayers.

As means toward improving the performance metrics of OFETs, rationally designed multifunctional self-assembled monolayers are used to explore the relationship between surface energy, SAM order, and SAM dipole on OFET performance. The studies presented within are (1) development of a multifunctional SAM capable of simultaneously modifying dielectric and metal surface while maintaining compatibility with solution processed techniques (2) exploration of the relationship between SAM dipole and anchor group on graphene transistors, and (3) development of self-assembled monolayer field-effect transistor in which the traditional thick organic semiconductor is replaced by a rationally designed self-assembled monolayer semiconductor. The findings presented within represent advancement in the understanding of the influence of self-assembled monolayers on OFETs as well as progress towards rationally designed monolayer transistors.

TABLE OF CONTENTS

List of Figures iv

List of Tables vi

Chapter 1. Introduction 1

Chapter 2. Introduction to Organic Field-Effect Transistors and Self-Assembled Monolayers 3

2.1 Introduction to Organic Field-Effect Transistors 3

2.1.1 OFET Device Architecture 3

2.1.2 OFET Working Principle 5

2.1.3 Charge Transport in Organic Semiconductors 8

2.1.4 OFET Transfer and Output Characteristics and Key Parameter Determination 10

2.2 Introduction to Self-Assembled Monolayers 13

2.2.1 Archetype of a Self-Assembled Monolayer 13

2.2.2 SAM Anchor Group 13

2.2.3 SAM Alkyl Spacer Unit 18

2.2.4 SAM Functional Head Group 19

2.2.5 Assembly of Phosphonic Acid Based SAMs 22

2.2.6 Importance of Solvent on SAM Assembly 24

Chapter 3. Bottom-Contact n-Type Organic Field Effect Transistors Achieved via Simultaneous Modification of Electrode and Dielectric Surfaces 25

3.1 Introduction 26

3.2 Experimental 27

3.2.1 Synthesis of 6-phenoxyhexylphosphonic acid (Ph6PA) 27

3.2.2 Device Fabrication 29

3.3 Results and Discussion 30

3.3.1 Rationale of SAM Molecular Design 30

3.3.2 Characterization of SAM Treated Surfaces (AFM and Contact Angle) 31

3.3.3 Spectral Characterization of SAM Treated Surfaces (NEXAFS) 32
3.3.4 Top- and Bottom-Contact OFET Device Performance 33
3.3.5 Device Contact Resistance 37
3.4 Conclusion 39
Chapter 4. Understanding the Role of Self-Assembled Monolayers on Graphene Transistors 40
4.1 Influence of Self-Assembled Monolayer Binding Group on Graphene Transistors 41
4.1.1 Introduction 41
4.1.2 Experimental 43
4.1.3 Results and Discussion 44
4.1.4 Conclusion 50
4.2 Systematic Doping Control of CVD Graphene Transistors with Functionalized Aromatic Self-Assembled Monolayers 51
4.2.1 Introduction 51
4.2.2 Experimental 53
4.2.3 Results and Discussion 55
4.2.4 AFM and Contact Angle Goniometry of SAMs 56
4.2.5 Conclusion 67
Chapter 5. Enhanced Performance of Self-Assembled Monolayer Field-Effect Transistors with Top-Contact Geometry through Molecular Tailoring, Heated Assembly and Thermal Annealing 68
5.1 Introduction 69
5.2 Experimental 70
5.2.1 Synthesis of SAM Molecules 70
5.2.2 SAM Assembly and Device Fabrication 79
5.2.3 AFM and Contact Angle Goniometry 81
5.2.4 X-ray Photoelectron Spectroscopy 81
5.2.5 Near-Edge X-ray Absorption Fine Structure Spectroscopy (NEXAFS) 81
5.3 Results and Discussion 82
5.3.1 Impact of Thermal Annealing on SAMFETs 84

5.3.2 Impact of SAM Immersion Assembly Temperature 88
5.3.3 NEXAFS Characterization of SAMs and Impact of Annealing 94
5.3.4 SAMFET Comparison With or Without Methylthio Functional Group 96
5.3.5 SAMFET Contact Resistance 98
5.3.6 Low Voltage SAMFETs 99
5.4 Conclusion 103
Bibliography 104

LIST OF FIGURES

Figure 2.1. Different Device Architectures of Organic Field-Effect Transistors. 4
Figure 2.2. Idealized energy level diagram of an organic field-effect transistor 7
Figure 2.3. Theoretical calculations of relationship between transfer integral of tetracene and molecular packing 9
Figure 2.4. Representative transfer and output characteristic electrical curves of a standard pentacene OFET 10
Figure 2.5. Mechanism for formation of silane-based SAM on a metal oxide surface. ... 15
Figure 2.6. Mechanism for formation of phosphonic acid based SAM on a metal oxide surface with varying Lewis acidity. 17
Figure 3.1. Synthesis of 6-phenoxyexylphosphonic acid. 27
Figure 3.2. Device architecture and molecular structure of Ph6PA SAM 29
Figure 3.3. NEXAFS carbon K-edge spectra acquired at 30° and 80° from Ph6PA 32
Figure 3.4. Electrical characteristics of OFETs fabricated in this study. 35
Figure 3.5. AFM Morphology of C_{60} and PCBM based on SAM treatment and device architecture. 36
Figure 3.6. Contact resistance and electron mobility of fabricated devices based on device architecture and semiconductor. 37
Figure 4.1. SAM structure and representative morphology. 42
Figure 4.2. Raman spectrum for graphene on SAMs used in this study. 45
Figure 4.3. Graphene transistor schematic and transfer characteristics. 46
Figure 4.4. Averaged charge neutrality point and mobility of graphene transistors 47
Figure 4.5. Chemical structure of SAMs and representative AFM morphology. 55
Figure 4.6. Raman spectra of graphene on SAM signifying high quality graphene. 58
Figure 4.7. Influence of SAM dipole on graphene work function and shift in C 1s binding peak from XPS. 60
Figure 4.8. Graphene transistor schematic and transfer curve 62

Figure 4.9. Schematic showing the total influence of SAM and metal electrode on graphene transistors. 66
Figure 5.1. Synthesis of 2-(4-methylthiobutyl)terthiophenyltrimethyltin. 70
Figure 5.2. Synthesis of 11-(4-methylthiobutylquaterthiophenyl)undecylphosphonic acid.74
Figure 5.3. Synthesis of 12-(4-methylthiobutylquaterthiophenyl)dodecylphosphonic acid.77
Figure 5.4. SAM semiconductor structure and high-voltage SAMFET device schematic.82
Figure 5.5. Transfer characteristics of high-voltage MTB4TC12 SAMFETs with various annealing conditions. 84
Figure 5.6. High-voltage transistor performance parameters for a) hole mobility and b) threshold voltage based on SAM semiconductor and annealing route 85
Figure 5.7. Representative morphology of Au on top of MTB4TC11 SAM assembled on AlO_x measured by AFM with different annealing conditions..... 87
Figure 5.8. Representative morphology of semiconductor SAMs assembled on AlO_x/300 nm SiO_2/Si substrates at 25 °C and 120 °C..... 89
Figure 5.9. Hole mobility of high voltage SAMFETs with either MTB4TC11 or MTB4TC12 SAM semiconductor assembled at 25 °C or 120 °C. 91
Figure 5.10. Average transistor performance characteristics of high voltage SAMFETs with MTB4TC12 SAM semiconductor prepared via immersion assembly at 25 °C, 60 °C, 90 °C, and 120 °C..... 92
Figure 5.11. Electrical characteristics of high voltage SAMFETs that have been annealed after electrode deposition with MTB4TC11 semiconductor SAM 93
Figure 5.12. NEXAFS C K-edge spectra from unannealed and annealed samples of MTB4TC11 94
Figure 5.13. AFM image of MTB4TC12 on a HfO_2/300 nm SiO_2/Si dielectric stack assembled at 120 °C 97
Figure 5.14. Comparison of hole mobility and contact resistance of high voltage SAMFETs consisting of MTB4TC11, MTB4TC12, and B4TC11 assembled on HfO_2. 98
Figure 5.15. Characterization of metal-insulator-metal junctions for determination of HfO_2 current density and capacitance. 100
Figure 5.16. Electrical characterization of low voltage MTB4TC12 based SAMFETs. 102

LIST OF TABLES

Table 3.1. Averaged performance data of C_{60} and PCBM OFETs 34

Table 4.1. Summarized data from this study contained dipole moment, contact angle, work function shift, charge neutrality point, and mobility. 57

Table 5.1. Atomic composition (in atomic %) and intensity ratio derived from XPS spectra of MTB4TC12 SAM semiconductor assembled at different temperature…. 90

Table 5.2. NEXAFS tilt angle calculations based on SAM semiconductor, annealing condition, and presence of Au…. 95

ACKNOWLEDGEMENTS

First, I would like to express my sincere appreciation and gratitude towards my advisors Professor Alex Jen and Professor Hong Ma for mentoring me for the last five and a half years. Without your advice and effort to guide me in the right direction this work would not have been possible. I thank Professor Christine Luscombe and Professor M. P. Anantram for being on my supervisory committee. I thank current and former Jen group colleagues, in particular Dr. Orb Acton, Dr. Tae-Wook Kim, Daniel Hutchins, Dr. Chu-Chen Chueh, Dr. Sei-Hum Jang, Dr. Jingdong Luo, Spencer Williams, Po-Wei Liang, Dr. Jingyu Zou, and Ting Zhao. Furthermore, I thank my collaborators, for without which much of this work would not have been possible, Professor Tobias Weidner (Max Planck Institute for Polymer Research, Germany), Professor Joe E. Baio (Oregon State University), Professor Xiaodong Xu, Dr. Sanfeng Wu, Dr. Joshua A. Davies, and Dr. Benjamin W. Krueger.

Finally I want to thank my family for both their emotional and financial support. I thank my parents for always encouraging me to pursue my dreams and standing by my side. I also express my deepest gratitude to my better half, Quy, who through the many trials and tribulations of not only graduate school, but also life, has always been there for me. Without her, this dissertation would not have been possible.

DEDICATION

To my wife Quy

Chapter 1. INTRODUCTION

Organic electronics show potential to replace many traditional inorganic electronic counterparts ranging from photovoltaic cells, light-emitting diodes, and in certain cases transistors. This potential stems from advantages of organic devices due to cheaper processing conditions, such as low temperature requirements, rapid, scalable processing techniques like inkjet printing, and the ability to tailor device properties based on molecular and structural design. However, one of the key challenges is controlling the interfaces between differing device layers in order to maximize performance. Interfaces of different materials are commonly not compatible with each other due to but not limited to a differences in surface energy, electrostatic interactions, electronic structure, or morphology. This degradation of compatibility between different interfaces can significantly hinder device performance and in particular and disrupt charge transport by creating interface trap states. This interface incompatibility is particularly disruptive when an organic device layer meets an inorganic one which is common for most organic electronic device architectures as an inorganic dielectric is typically used. Additionally, metals such as gold, silver, and aluminum are commonly used as electrodes to facilitate charge transport. These typical inorganic materials clash with the organic semiconducting materials used to achieve the designed electronic effect such as charge separation and recombination in photovoltaics and field-effect charge transport in transistors.

Self-assembled monolayers are now ubiquitously used to modify these organic/inorganic interfaces in order to limit or even control their detrimental effects on charge transport. Recent progress has also expanded the role of SAMs from a passive interfacial modifier to potentially serve as an active device layer to replace traditional dielectrics and semiconductors in organic field-effect transistors (OFETs). For example, the development of hybrid dielectrics, which are comprised of an ultra thin high-k metal oxide layer in conjunction with a SAM, enables low-voltage high-performance operation of organic transistors. Self-assembled monolayer field-effect transistors (SAMFETs) are a promising concept that uses rationally designed π-conjugated SAMs as the semiconductor of a transistor. This concept works in principle because charge transport in an organic semiconductor based FET occurs in the first few monolayers closest to the dielectric. SAMFETs are believed to have a broad appeal for organic semiconductor device applications due

to their low-cost processing, reduced material quantity needed compared to tradition organic thin film transistors and ability to be used toward flexible electronics and sensing applications. This dissertation will discuss the use of self-assembled monolayers to control the interfacial properties, and ultimately device properties of organic field-effect transistors and the use of SAMs as a semiconductor replacement for OFETs.

This dissertation is divided into four chapters. Chapter 2 aims to introduce the reader to organic field-effect transistors (OFET) and self-assembled monolayers (SAM). The working principles of OFETs and charge transport are briefly described. In addition the use of SAMs and their applications as interfacial materials are discussed. Chapter 3 presents the results and development of a SAM compatible with bottom-contact n-type OFETs that are both solution processed and thermally deposited. Chapter 4 presents the results of several projects looking at the influence of SAMs on graphene transistors. The first project shows that the dipole and order of the SAM binding group can play a critical role on the position of the charge neutrality point. The second project is a systematic study of the influence of SAM dipole on the position of graphene charge neutrality point. It is found that the total doping environment from both the SAM dipole and also metal electrode must be considered in order to predict the position of graphene charge neutrality point. Chapter 5 presents a series of processing and molecular design steps to significantly enhance the performance of a self-assembled monolayer field-effect transistor. The mobility performance metric for this SAMFET is improved by over 3 orders of magnitude.

Chapter 2. INTRODUCTION TO ORGANIC FIELD-EFFECT TRANSISTORS AND SELF-ASSEMBLED MONOLAYERS

2.1 Introduction to Organic Field-Effect Transistors

2.1.1 *OFET Device Architecture*

An organic field-effect transistor can be described as a three-terminal voltage controlled current source. This consists of highly conductive source, drain, and gate electrodes, an organic semiconductor layer, and a gate dielectric. Superficially, the device architecture can be simplified and described as a "metal/insulator/metal" capacitor in which the source electrode, semiconductor layer, and drain electrode can be considered as one of the "metal" layers, while the gate dielectric and gate electrode could be described as the insulator and other metal respectively. This means that, so long as the gate dielectric is sandwiched between the two "metal" layers a field-effect transistor can be formed. This gives rise to four different possible device architectures for an OFET as seen in Figure 2.1 which each have their own respective advantages and disadvantages.

The four main variants of organic field-effect transistors device architectures are bottom-gate top-contact (BG-TC), bottom-gate bottom-contact (BG-BC), top-gate top-contact (TG-TC), and top-gate bottom-contact (TG-BC). For BG-TC architecture, the gate electrode is first deposited on the substrate or a global gate electrode, such as degenerately doped silicon, is used which acts as both the gate electrode and substrate. Subsequently, the dielectric, semiconductor, and source/drain electrodes are consecutively deposited. The difference between BG-TC and BG-BC is that the source/drain electrodes for TC electrodes are deposited on top of the semiconductor while for BC electrodes the source/drain electrodes are deposited on top of the dielectric. For TG-TC architecture, the semiconductor is first deposited on a substrate which is consecutively followed by the source/drain electrodes, gate dielectric, and gate electrode. The difference between TG-TC

and TG-BC is similar for the bottom-gate variant in which the TC electrodes are deposited on top of the semiconductor while BC electrodes are first deposited on the substrate followed by the semiconductor. The specific architecture chosen is usually decided after careful consideration of a variety of factors such as material limitation, cost, and application.

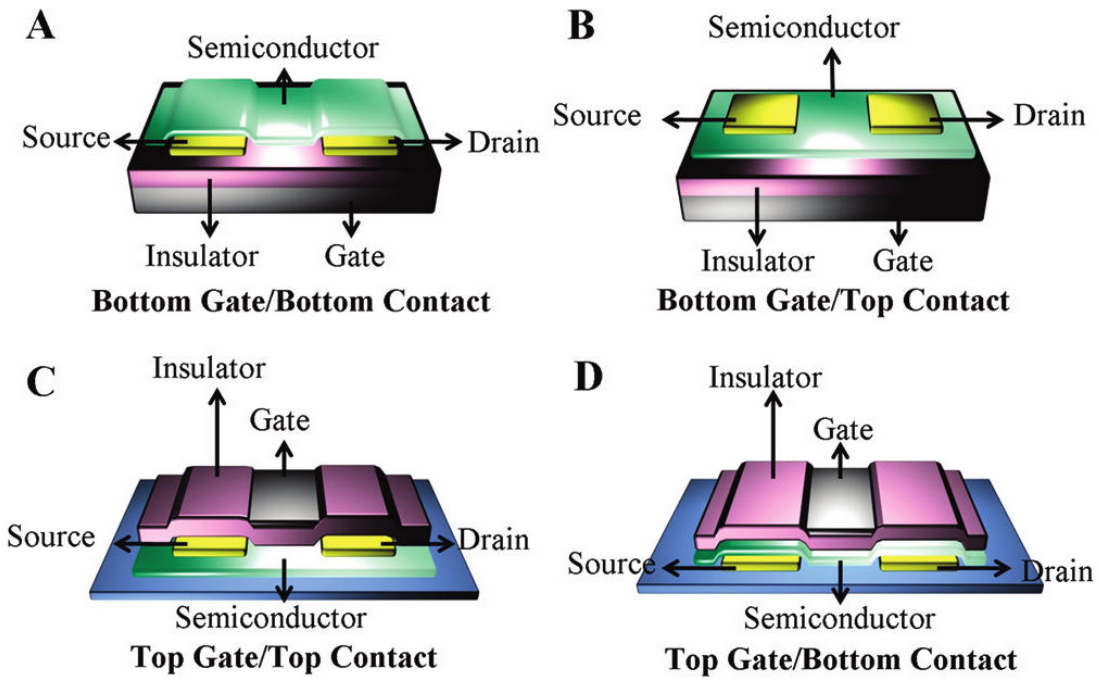

Figure 2.1. Different Device Architectures of Organic Field-Effect Transistors. (a) Bottom gate, bottom contact (BG-BC) (b) bottom gate, top contact (BG-TC) (c) top gate, top contact (TG-TC) and (d) top gate, bottom contact (TG-BC). Reprinted with permission from [1]. Copyright 2010, American Chemical Society.

The OFET device architecture is chosen based on a variety of factors such as its impact on transistor performance, the material system used, compatibility with existing processing infrastructure, and stability in ambient conditions. For example, the inherent instability of organic anions in the presence of air or water [2-4] makes many n-type OFETs unstable when operating under ambient conditions. This instability can be alleviated with a top-gate device architecture as the dielectric on top of the semiconductor will act as an encapsulating layer of the semiconductor.

However, it is important to note that this type restricts the material systems available for use since usually both the organic semiconductor and dielectric are deposited by solution processing. In this case, the dielectric/semiconductor layers would need to use orthogonal solvents which dissolve one material and not the other [5].

The performance of the OFET can also be significantly affected by the chosen device architecture. For example, the morphology of the semiconductor layer may be affected by the morphological and/or surface energy difference at source/drain electrode and dielectric interface. The morphological step height may lead to the addition of defects within the semiconductor at the electrode, semiconductor, and dielectric triple interface by disrupting the order and crystallinity of the semiconductor. Additionally, semiconductor defects may be generated by the differing surface energy of electrode and dielectric due to its influence on the morphology of the semiconductor. Furthermore, the surface dipole of the metal electrode may also have an effect at the semiconductor/electrode interface. These factors can contribute to a charge injection barrier that can impede the exchange of charge carriers between the source/drain electrodes and semiconductor. This charge injection barrier is exacerbated by coplanar device architectures, BG-BC and TG-TC, which have metal electrodes directly in line with the first few layers of the semiconductor closest to the dielectric. Thus coplanar device architectures change the semiconductor morphology at the electrode/semiconductor interface closest to the dielectric which is primarily where charge carrier transport in OFETs occurs. On the other hand, staggered OFET device structures BG-TC and TG-BC are less affected by these factors due to either the semiconductor being deposited before the electrodes (BG-TC) or there being a significant distance between the electrodes and the semiconductor/dielectric interface (TG-BC) [6-8]. Overall, the chosen device architecture is based on a compromise of various factors.

2.1.2 *OFET Working Principle*

In principle, an organic field-effect transistor is voltage controlled current source. As shown in Figure 2.1 an OFET is a three terminal device in which the amount of current that flows between the source and drain electrodes (drain-source current, I_{ds}) can be controlled by an applied bias between the gate and source (gate-source voltage, V_{gs}) and drain and source (drain-source voltage, V_{ds}). While the mechanism of charge transport in the organic semiconductor is different than that

of an inorganic semiconductor, the working principle of an OFET is generally described similarly to that of an inorganic MOSFET due to the similar device architecture. The exact operation principle will be briefly described here in context of OFETs, however a more detailed analysis is available from the authoritative text on semiconductor devices by Sze and Ng. Additionally, it is important to note here that generally OFETs, unlike most MOSFETs, operate in accumulation mode. This means that for OFETs there typically exists little to no mobile charge intrinsically available in the organic semiconductor. Thus these devices are described as "normally off" and the drain-source current is in the OFF, or low-current-state, when a small or zero drain-source and gate-source bias is applied.

The operation of an OFET is simplistically described in Figure 2.2 and is directly related to the applied drain-source and gate-source bias [9]. For n-channel (p-channel) operation a gate-source voltage greater (less than) zero is applied which causes the accumulation of a sheet of mobile electrons (holes) at the semiconductor/dielectric interface. This sheet of mobile charge carriers is generated by the electric field from the gate-source potential and causes the semiconductor LUMO (HOMO) to shift down (up) in energy and align with the Fermi level of the source/drain electrode. Once the LUMO of the organic semiconductor is aligned with the metal Fermi level electrons are able to flow from the source contact into the LUMO thus generating a sheet of mobile charge carriers. Conversely, for p-type operation, after Fermi level alignment electrons flow from the semiconductor into the source-contact leaving positively charged holes in the semiconductor. Upon application of an appropriate drain-source voltage, the electric field generated causes the respective charge carriers to flow from source to drain and drain-source current increases linearly until pinch-off occurs which will be described in greater detail in section 2.1.5.

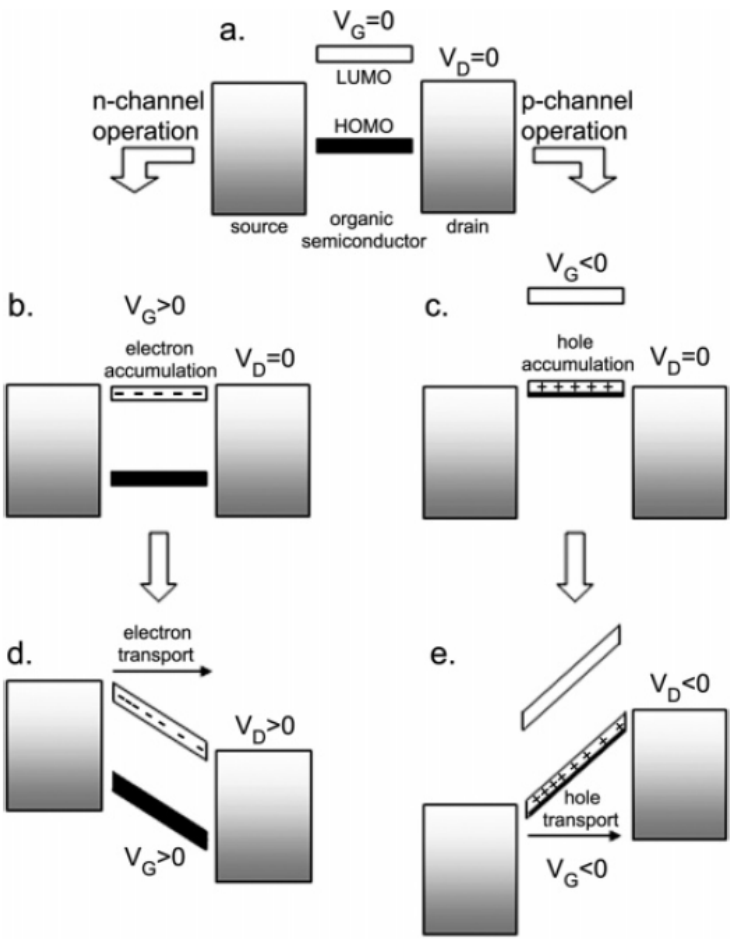

Figure 2.2. Idealized energy level diagram of an organic field-effect transistor at (a) V_G = 0 and V_D = 0. Demonstrates the principle of field-effect transistor operation for the case of electron accumulation (b) and transport (d) and hole accumulation (c) and transport (e). Reprinted with permission from [9]. Copyright 2004, American Chemical Society.

2.1.3 *Charge Transport in Organic Semiconductors*

Performance as determined by charge carrier mobility of organic field-effect transistors has steadily increased since the 1980's polythiophenee based OFET hole mobility of 10^{-5} cm^2 V^{-1} s^{-1} [10] to more recent values ranging from 43 cm^2 V^{-1} s^{-1} for single crystal rubrene [11] and 31.3 cm^2 V^{-1} s^{-1} for benzothieno[3,2-b][1]benzothiophene [12] based OFETs. These significant performance improvements are a result of a multipronged approach by the scientific community to develop novel organic semiconductors, optimize device fabrication and processing conditions, interface engineering at the device level, improvements in material purity, and advancements in testing conditions [13]. This section will briefly cover the basic principles of charge transport in organic semiconductors. However, more detailed analysis and review of design rules for high performance organic semiconductors are detailed elsewhere [1, 13-16].

At the most basic level, organic semiconductors can be described as a molecule or polymer backbone with alternating single and double carbon-carbon bonds known as conjugation. The carbon double bonds form sp^2 hybrid oribtals which produce three covalent σ bonds within a plane and leaves a nonhybridized out-of-plane p_z orbital. Overlap of p_z orbitals with adjacent carbons can form π orbitals which become delocalized over the molecule or portions of the polymer backbone. The filled π bonding orbitals form the valence states, more commonly known as the highest occupied molecular orbital (HOMO), and the empty π* antibonding orbitals form the conduction states, more commonly known as the lowest unoccupied molecular orbital (LUMO) [17].

At room temperature charge carrier mobility of organic materials is determined by a thermally activated polaronic hopping transport process [18]. Charge carriers are believed to be localized over a single molecular unit due to strong electron-phonon coupling [19, 20]. The two key parameters that determine the effectiveness of this transport process are known as the transfer integral (t) and the reorganization energy (λ). The transfer integral is related to the electronic coupling between adjacent molecules and is dependent on molecular packing contributions such as π orbital overlap, π-π stacking distance, and intermolecular interactions. Figure 2.3 shows the results of theoretical calculation to determine the evolution of the transfer integral with relationship to molecular spacing, tilt angle, and displacement. The reorganization energy is related to internal

and external contributions. Internal reorganization energy is related to molecular deformations upon charging and is dependent on molecular rigidity, conjugation length, etc. External reorganization energy is related to changes in the surrounding media related to charge transfer. In order to achieve the highest charge carrier mobility it is necessary to have both a large transfer integral and a small reorganization energy.

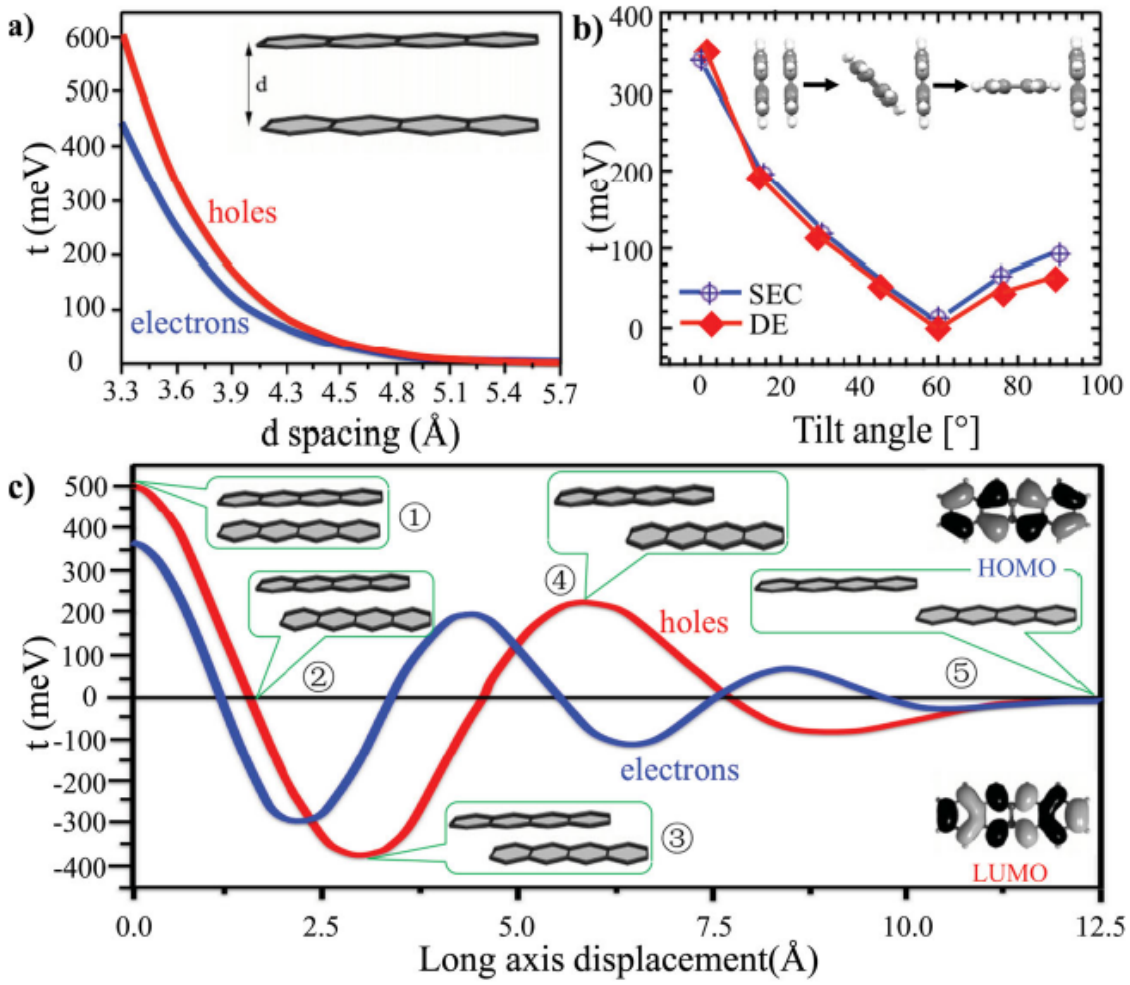

Figure 2.3. Theoretical calculations of relationship between transfer integral of tetracene and molecular packing. Evolution of transfer integral with relationship between (a) d spacing (b) molecule tilt angle base calculated by SEC (site-energy correction) and DE (direct evaluation) and (c) long axis displacement. Reprinted with permission from [13]. Copyright 2014, Wiley-VCH Verlag GmbH & Co. KGaA.

2.1.4 *OFET Transfer and Output Characteristics and Key Parameter Determination*

Organic field-effect transistors have several figures of merit used to describe their performance. The most often compared value is that of the charge carrier mobility (μ). Charge carrier mobility is described as the velocity of a charge carrier (hole or electron) in response to an applied electric field with units of measurements typically expressed as $cm^2\ V^{-1}\ s^{-1}$. The mobility of OFETs is most commonly compared to that of amorphous silicon (~1 $cm^2\ V^{-1}\ s^{-1}$) which is now commonly surpassed by benchmark OFETs [15]. The threshold voltage (V_{th}) is the gate-source voltage at which mobile charge carriers can be injected into the semiconductor. This value is influenced by several factors such as the energy mismatch between metal electrode and semiconductor which causes the generation of a dipole and band bending in the organic semiconductor, hole or electron traps at the electrode/semiconductor or semiconductor/dielectric interface, impurities, etc [9]. The on/off current ratio (I_{ON}/I_{OFF}) is the difference in drain-source current of the OFET comparing on and off states. Finally, the subthreshold swing, S is a measure of the exponential behavior of the drain-source current as a function of gate-source voltage. Subthreshold swing is expressed in units of mV dec^{-1} and essentially describes how quickly, or rather over what voltage range, the device turns on.

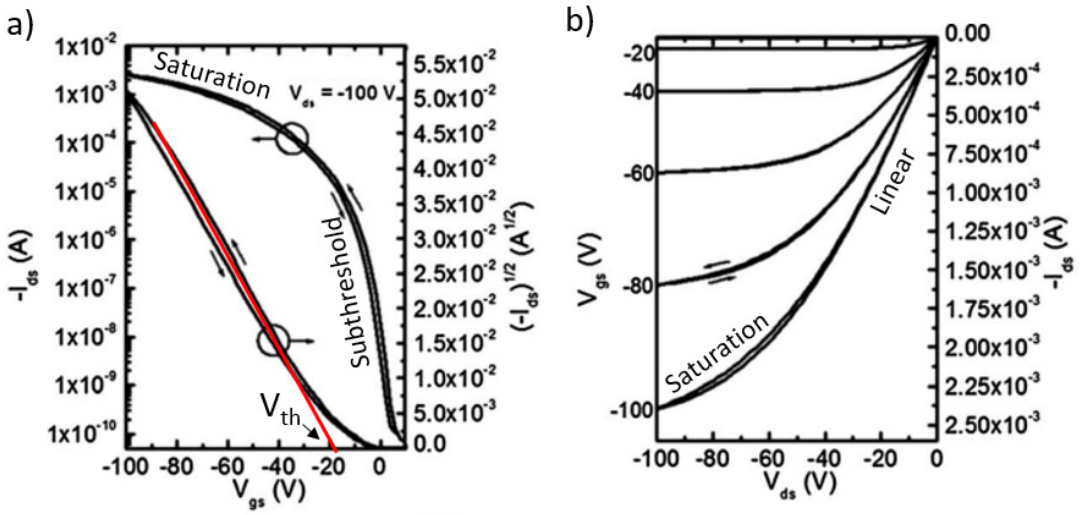

Figure 2.4. Representative transfer and output characteristic electrical curves of a standard pentacene OFET. (a) Transfer and (b) output series of electrical curves for pentacene based OFET with 300 nm SiO_2 dielectric.

Electrical measurements of OFETs typically follow a standard sequence of events in order to properly determine the performance parameters. Firstly, the capacitance and voltage limitations of the gate dielectric must be determined. This is typically done by measuring the capacitance-voltage (C-V) characteristics of a metal-insulator-metal (MIM) device where the insulator is the same insulator used in the OFET device architecture. The C-V characteristics will measure the capacitance of the dielectric used which will be necessary for determination of the OFET mobility. Additionally, current density versus voltage measurements will allow for one to determine the general voltage range that has minimal leakage current for the OFET device. Once the C-V measurement has been completed, the measurement can be compared to the expected value based on known parameters of the dielectric. For a parallel plate capacitor (MIM) the capacitance is related as followed:

$$C_{ox} = \frac{\varepsilon_r \varepsilon_o}{d} \qquad (Eq. 2.1)$$

where C_{ox} is the capacitance per unit area (F cm^{-2}), ε_r is the relative dielectric constant (3.9 for SiO_2), ε_0 is the permittivity of free space, and d is the thickness of the dielectric. From this equation we can see that C_{ox} can be controlled by either changing the relative dielectric constant by using a different insulator or by reducing the thickness of the dielectric. The operating voltage of the OFET can be decreased by increasing the capacitance as shown by the next equation.

One the capacitance is known, the output series of electrical characteristic curves are determined by holding V_{gs} constant and varying V_{ds} while measuring I_{ds} as seen in Figure 2.4b. This measurement is done consecutively with V_{gs} changing over the voltage range measured previously that allows for minimal leakage current (I_{gs}). Once this measurement is completed, V_{ds} is chosen based on the voltage at which I_{ds} is saturated for every V_{gs} value. In the case of Figure 2.4b, this would be at a V_{ds} value of -100 V. The transfer electrical measurement can then be performed by holding V_{ds} constant and measuring the drain-source current in response to a changing gate-source voltage as seen in Figure 2.4a. The mobility of the OFET can be determined in either the linear or saturation regimes of the electrical measurements. The device operation equations can be described in the same manner of inorganic MOSFETs described elsewhere [21].

The relationship between I_{ds}, V_{ds}, and V_{gs} in the linear regime can be described as follows:

$$I_{ds,lin} = \frac{W}{L} C_{ox} \mu_{lin} \left[\left(V_{gs} - V_{th} \right) - \frac{V_{ds}}{2} \right] V_{ds} \qquad (Eq. 2.2)$$

The relationship between I_{ds}, V_{ds}, and V_{gs} in the saturation regime can be described as follows:

$$I_{ds,sat} = \frac{W}{2L} C_{ox} \mu_{sat} \left(V_{gs} - V_{th} \right)^2 \qquad (Eq. 2.3)$$

Where W is the channel width, L is the channel length, C_{ox} is the capacitance per unit area of the dielectric, μ_{lin} is the charge carrier mobility in the linear regime, and μ_{sat} is the charge carrier mobility in the saturation regime of the electrical measurements. The charge carrier mobility can thus be determined in the saturation regime from the slope of the $(|I_{ds,sat}|)^{1/2}$ vs. V_{gs}. Additionally, the threshold voltage can be determine as the x-intercept of the linear region in the $(|I_{ds,sat}|)^{1/2}$ vs. V_{gs} plot.

2.2 Introduction to Self-Assembled Monolayers

2.2.1 *Archetype of a Self-Assembled Monolayer*

A self-assembled monolayer (SAM) is a rationally designed molecular system that is typically comprised of three parts: (1) a reactive binding site, or anchor group, that will adhere to a particular surface via chemisorption, (2) a middle spacer unit that is generally composed of an alkyl group, and (3) a functional head group. Each element of a SAM provides a specific, designed purpose which together create the multifunctional properties of the completed self-assembled monolayer.

2.2.2 *SAM Anchor Group*

In order to functionalize a chosen surface with a SAM, it is critical to select an appropriate anchor group which allows for chemisorption of the SAM to the intended surface. The mechanism and kinetics of chemisorption is of course dependent on this chosen moiety and plays a critical role in determining the quality of the assembled monolayer. For example, SAMs with a phosphonic acid based anchor group readily assemble on activated Al_2O_3 [22] while the formation of a reasonably dense monolayer on SiO_x requires the use of a specialized assembly technique [23] due to the limited reaction kinetics. In the same manner, Ting et al. showed that the quality of SAM on HfO_2 depends strongly on the chosen anchor group. In their study, assembly of octadecyclphosphonic acid (ODPA) and steric acid (SA) were compared using the same processing conditions [24]. The results showed that ODPA was significantly denser due to its higher static water contact angle even though morphology measured by atomic force microscopy was comparable. This difference in SAM quality most likely stems from the difference in acidity between phosphonic acid (pKa ~2) and carboxylic acid (pKa ~4) which will be further elaborated later in this section. Thus, in order to form a dense monolayer it is critical to select a proper anchor group for the surface that is desired to be modified.

2.2.2.1 *Thiol-based SAMs for Assembly on Transition Metals*

One of the most common electrode materials, gold, is typically functionalized by SAMs with a thiol anchor group which is chosen due to sulfur's strong affinity towards transition metal surfaces. This affinity most likely derives from sulfurs ability to form multiple bonds with a transition metal surface [25]. The chemical binding mechanism for a thiol-based SAM to gold can be considered as an oxidative reaction followed by a reductive elimination of hydrogen as described in detail elsewhere [26]. This reaction results in the binding of the thiolate to the gold surface with a strength of approximately 40 kcal mol^{-1} with a byproduct of most likely hydrogen gas [27]. In addition to gold, thiol-based SAMs have been shown to functionalize other transition metal surfaces such as Ag [28], Cu [29], Pt [30], Hg [31], and Fe [32]. However, typically for OFETs thiol-based SAMs are limited to the functionalization of Au electrodes as more suitable systems such as phosphonic acid are available for the modification of the metal oxide dielectric and native oxide present at the surface of common metal electrodes such as Al, Ag, and Cu.

2.2.2.2 *Silane-based SAMs for Assembly on Silicon Dioxide*

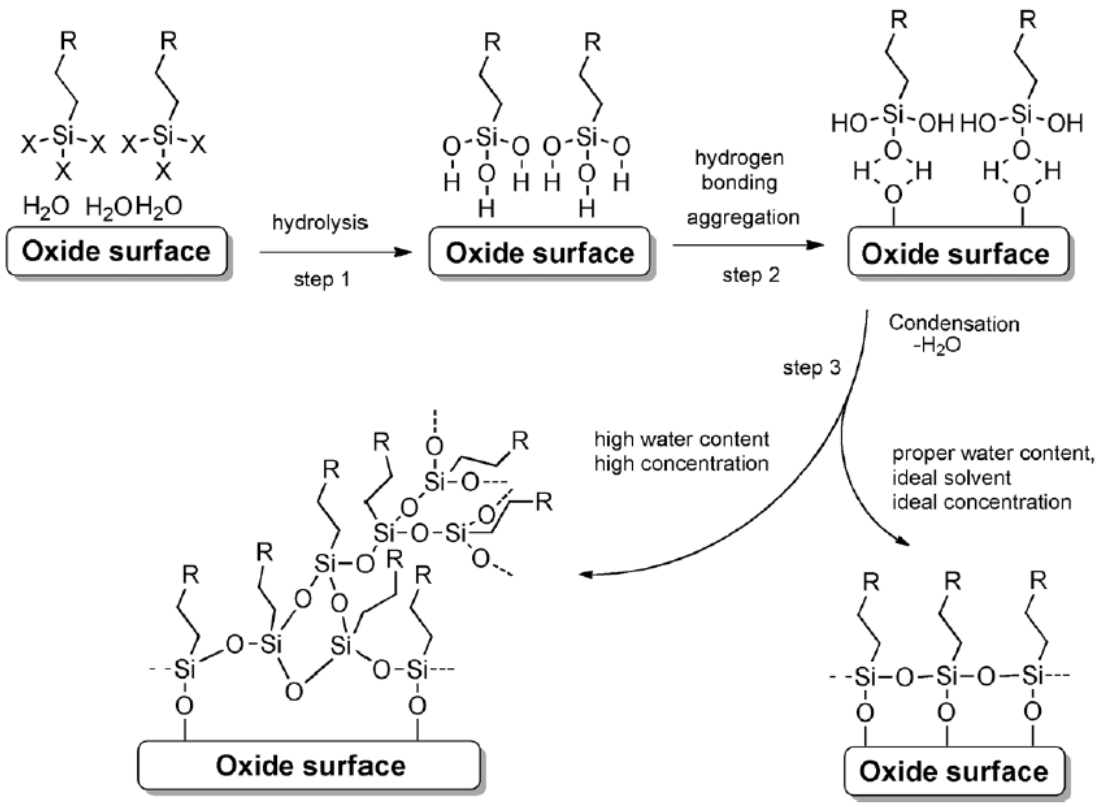

Figure 2.5. Mechanism for formation of silane-based SAM on a metal oxide surface. Step 3 condensation reaction shows the results of water content or poor SAM assembly conditions. Reprinted with permission from [33]. Copyright 2014, Wiley-VCH Verlag GmbH & Co. KGaA.

Silane-based SAMs are the most common anchor group used to bind to the most common dielectric surface, SiO_2, used in field-effect transistors. The main driving force for silanes is the formation of polysiloxane which is formed at the inorganic/organic interface and links each SAM molecule to its adjoining neighbor as well as linking the molecule to the metal oxide surface. This is characterized as a three step procedure as seen in Figure 2.5. Firstly, the silane-based SAM molecule is hydrolyzed by the water present at the silicon oxide surface which results in the molecule being hydrogen bonded to the polar oxide surface. At this stage, since the entire surface is hydroxylated, the SAM is able to freely move on the substrate surface and as such aggregation

driven by intermolecular forces such as van der Waals, hydrogen-bonding, or dipole-dipole occurs. Once aggregated the molecule is significantly less mobile and a final condensation reaction occurs in which Si-OH groups become Si-O-Si. This reaction occurs not only at the substrate/SAM interface but also between individual SAM molecules [33].

One of the downsides to this type of chemical reaction is that it makes the SAM very sensitive to water and subsequently any moisture present in ambient conditions. The presence of moisture makes it possible for these silane-based SAMs to react with each other causing issues with homocondensation [34] subsequently, that makes it difficult to reliably reproduce results in ambient conditions due to the ever changing environmental conditions. Another factor that limits the uses of silane-based SAM molecules is that the driving force is limited by the amount of surface hydroxyl groups present on the metal oxide surface [35]. A lack of hydroxyl groups will directly impact the quality of the silane-based SAM and can significantly hinder SAM packing density. Due to these drawbacks, attention from silane-based SAMs has shifted towards phosphonic acid based SAMs for the purpose of metal oxides intended to be used in OFETs which will be discussed in the next section.

2.2.2.3 *Phosphonic Acid-based SAMs for Assembly on Metal Oxide Surfaces*

On the other hand, phosphonic acid (PA) based SAMs are able to modify most metal oxides without the limitation that stifles silane-based SAMs. PA SAM molecules moisture stability and lack of homocondensation [34] makes them ideal molecular system for reliably producing high quality densely packed SAMs. The assembly mechanism of PA SAM molecules is dependent on the characteristics of the metal oxide surface. The two routes are described in detail in Figure 2.6. However, since most PA-based SAMs result in bidentate binding on metal oxides and metal oxide substrates for OFETs are typically pre-treated by air plasma or UV/O_3 to clean and hydroxylate the substrate surface, focus will be paid to route 2 which is substrates of low Lewis acidity. For surfaces of low Lewis acidity, PA based SAMs are expected to initially coordinate via hydrogen bonding between surface M-OH groups and P-OH. This is then followed by an acid-base condensation reaction. The acidic SAM will react with the basic surface to form a chemically bound molecule to the surface with water as a byproduct. The P-O groups of the SAM molecule will bond with the surface to form, for example, Al-O-P. Typically, phosphoric acids form via

bidentate [23] due to both of the OH groups binding with the metal oxide surface. A strength of this type of interaction is the fact that since phosphoric acid SAMs supply their own OH moieties they are not limited by the surface hydroxyl group, however the reaction rate is strongly dependent on the metal surface hydroxyl count [36].

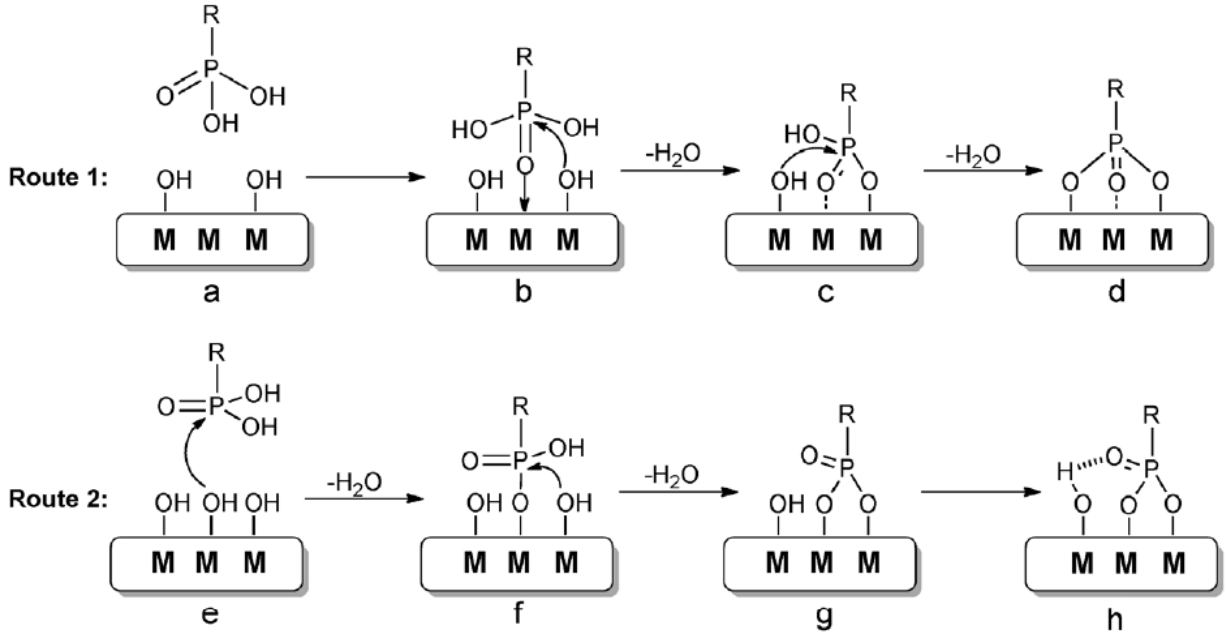

Figure 2.6. Mechanism for formation of phosphonic acid based SAM on a metal oxide surface with varying Lewis acidity. 1) Route for Lewis acidic metal oxides and 2) route for poorly Lewis acidic metal oxides. Reprinted with permission from [33]. Copyright 2014, Wiley-VCH Verlag GmbH & Co. KGaA.

One drawback to phosphoric acid based SAMs is that the relative basicity of a metal oxide surface plays a role in assembly conditions. For example, silanol (Si-OH) present on the surface of SiO_2 is contains mixed acidic and basic surface hydroxyl orientations with pK_a of approximately 4.5 and 8.5 respectively [37] making the reaction between phosphonic acid based SAMs and Si-OH unfavorable. Due to this fact phosphoric acid based SAMs are generally unable to form dense monolayers on silicon oxide surfaces. However, other typical dielectric systems such as aluminum oxide and hafnium oxide readily form monolayers these acid based SAMs. Table 2.1 summarizes the expected pK_a of various acidic SAMs used for assembly as well as expected pK_a of different

metal oxide surfaces. Understanding the chemical interactions for chemisorption to different surfaces is important as it will allow for tailoring of molecular design to form a densely packed monolayer based on desired device structure.

2.2.3 *SAM Alkyl Spacer Unit*

While not all SAMs are designed with a spacer unit, the majority of SAMs whose intention is to achieve as dense and well-ordered monolayer as possible typically utilize some length alkyl group. The most ordered SAMs forego the functional head group and solely consist of an anchor group and long chain alkyl group. Such design choices are made due to the additive nature of the van der Waals interaction between alkyl groups. The expected interaction energy between adjacent CH_2 groups is between 1-2 kcal mol^{-1} [38]. While individually miniscule compared to the SAM anchor group interaction with the modified surface, the additive nature of the van der Waals forces are able to reach a near equivalent strength dependent on the SAM molecule design. For example, the total contribution of van der Waals forces for the entire chain of decanethiol on Au(111) was found to be comparable to the Au-S functionalization which binds the SAM to the Au surface [39]. Furthermore, it has been found by Hotchkiss et al. that the binding energy of octylphosphonic acid (C8) and octyldecylphosphonic acid (C18) to an ITO surface was about 20 kcal mol^{-1} and 40 kcal mol^{-1} respectively indicating the significant role that the length of alkyl spacer group plays on total adhesion energy [40]. Due to this strong additive interaction, as the length of the alkyl group increases, the relative SAM order also increases. This is particularly important to note for SAMs which are to be used in a hybrid dielectric platform which require well-ordered SAMs for minimal leakage current. A hybrid dielectric platform is a low-voltage platform consisting of an ultra-thin high-k dielectric combined with a SAM. Acton et al. found that as the SAM alkyl group increased, the relative SAM order also increased as determined by the CH_2 vibrational peaks measured by ATR-FTIR [41] while Jedaa et al. showed that current density improved as alkyl length increased when used in a hybrid dielectric platform [42]. Additionally, Bao et al. showed the assembly of a near crystalline silane based SAM with an 18 carbon alkyl group [43] which resulted in high performance OFETs. While the SAM spacer unit is an important element to enhance SAM order and packing density, it is critical to keep in mind the intended application of the SAM. For

example, as the SAM order increases, its ability to serve as a functional component of a hybrid dielectric system increases. However, as the length of the SAM increases from additional CH_2 groups, the insulating alkyl group will act as a charge injection barrier due should the SAM be intended to be a metal electrode modifier. Such an effect has been well studied by the Jen group where an acceptable trade off limit between SAM order and added resistance has been found to be around 1 nm thick [44, 45].

2.2.4 *SAM Functional Head Group*

SAMs provide a valuable tool of being able to control the surface energy of a modified surface. This can be useful not only to enable solution processing of materials such as the organic semiconductors, but also for controlling the morphology of the material system used. For example, Acton et al. showed that it is possible to selectively pattern the organic semiconductor by using SAMs to create one region which is hydrophobic and another which is hydrophilic. Upon spin-casting the organic semiconductor, a thin film would only be present on the area with a hydrophilic SAM This is enabled by using a fluorinated alkyl group to create an area of low surface energy and a phenoxy head group for a high surface energy area. The resulting effect is a pre-patterned organic semiconductor upon spin-casting [46]. Additionally, it has been found that the orientation of certain organic semiconductor material systems are dependent on surface energy of which they are deposited. Novak et al. found that SAMs with high and low surface energy respectively induced a face-on or edge-on growth of dihexylquaterthiophene semiconductor respectively [47]. Such different growth modes influenced OFET mobility with the low surface energy resulting in slightly enhanced mobility.

In addition to controlling surface energy, the functional head group of SAMs can be designed to influence the work function of metals and the position of the threshold voltage of an OFET based on a built-in electric field generated by the SAM dipole. Bert de Boer et al. has shown that the work function of gold and silver electrodes can be tuned over a range of 1.7 eV using aliphatic and perfluorinated alkane thiol based SAMs. Such control over work function allowed not only for the reduction of charge carrier injection, but additionally allowed for the ability to completely suppress conduction of one type of charge carrier [48]. More recently, SAMs have been used to modify the work function of the semimetal graphene which is a promising transparent electrode

material for OFETs amongst other applications. Park et al. has shown the ability to tune the work function of monolayer graphene on top of a SAM by 0.6 eV when enabled enhanced charge carrier injection and resulted in increased transistor mobility [49]. Additionally, within this dissertation, it shown that simple aromatic phosphonic acid based SAMs can systematically control the work function of graphene [50].

The dipole of the SAM functional head group is additionally able to control the position of the threshold voltage of OFETs. Such control is important for the integration of OFETs in digital circuits which require precise control of input voltage. Zschieschang et al. has shown that using a two different SAMs with opposing dipoles blended in different ratios allows for extremely précising tuning of threshold voltage in OFETs [51]. A more comprehensive study by Salinas et al. has shown using density functional theory to calculate the individual dipole components of each SAM that the SAM dipole component is directly and linearly related to the shift in threshold voltage. The dipole of the SAM generates a built-in voltage whose relationship is found to be as follows:

$$V_{SAM} = \frac{N\mu_z}{\varepsilon_0 \varepsilon_{SAM}} \qquad (Eq. 2.4)$$

Where N is the packing density of the SAM, μ_z is the dipole moment along the molecular axis, ε_0 is the permittivity of free space, and ε_{SAM} is the relative permittivity of the SAM. The total shift in threshold voltage is then related to the number of charge carriers induced by the SAM which is dependent on the total capacitance of the dielectric stack and can be described as follows:

$$\Delta V_{TH,SAM} = \frac{Q_{SAM}}{C_{total}} = \frac{C_{SAM}}{C_{total}} V_{SAM} \qquad (Eq. 2.5)$$

Where Q_{SAM} is the number of charge carriers induced by the SAM, C_{total} is the total capacitance of the dielectric stack and C_{SAM} is the capacitance of the SAM itself.

While dipolar SAMs are commonly used to control the threshold of OFETs, the origin of this voltage shift is still debated. Yoonyoung Chung et al. argues that the SAM dipole can cause band bending of the organic semiconductors' HOMO and LUMO levels making it easier or more difficult for charge transport to occur by effectively adjusting the electron affinity of the

semiconductor. Such a potential, induced by the SAM dipole must therefore be overcome which results in the shift of threshold voltage [52]. It is important to note that such a relationship between self-assembled monolayers and the threshold voltage shift only holds true for a certain limited low voltage range of operation. Once the capacitance of the system starts playing a larger role, it is argued that the mechanism of shift in threshold voltage is different. Gholamrezaie et al. recently showed using scanning kelvin probe microscopy that charge trapping induced by the dipolar SAMs at the SAM/semiconductor interface is responsible for the shift in threshold voltage [53]. However, the exact relationship between SAM dipole and trapped interface charges remain unstudied. Overall, the SAM functional head group can be designed for precise control of the metal work function and transistor threshold voltage.

More recently, researchers have taken high performance small molecule organic semiconductors and used them as a functional head group. After overcoming the difficulty of processing such a material system, this allows for the fabrication of self-assembled monolayer field-effect transistors (SAMFETs). SAMFETs are a promising concept that uses rationally designed π-conjugated SAMs as the semiconductor of a transistor. This concept works in principle because charge transport in an organic semiconductor based FET occurs in the first few monolayers closest to the dielectric [54, 55]. SAMFETs are believed to have a broad appeal for organic semiconductor device applications due to their low-cost processing, reduced material quantity needed compared to tradition organic thin film transistors and ability to be used toward flexible electronics and sensing applications. Significant progress has been made through molecular design and novel device architecture to achieve a state-of-the-art hole mobility of around 10-^{2} cm^{2} V^{-1} s^{-1}. In this case, the functional head group serves as a semiconducting core of the molecular system. The most well studied systems are oligothiophene based SAMs which have been shown to reach hole mobility as high as 10^{-2} cm^{2} V^{-1} s^{-1} [56, 57]. Other material systems such as C_{60} [58-60] and perylene [61, 62] derivatives for n-type SAMFET performance and BTBT ([1]benzothieno3,2-b][1]benzothiophene) [63] and phenylene-thiophene [64] derivatives for p-type SAMFET performance have been studied. However, the performance of SAMFETs is not just limited to molecular design as processing can play a critical role. This is elaborated further in this dissertation where the impact of SAM assembly conditions and post-assembly conditions account for a difference in SAMFET mobility by up to three orders of magnitude [57]. While still in its infancy, semiconducting SAMs offer a promising application of SAMs for use as a

semiconductor replacement. The ultimate goal of a SAMFET would be to have a functional group semiconductor and a long spacer unit that is capable of acting as the device dielectric. In this manner, the majority of device layers for a monolayer transistor could be fabricated in a single step which would significantly reduce cost and processing time.

2.2.5 *Assembly of Phosphonic Acid Based SAMs*

The assembly conditions of self-assembled monolayers can vary significantly based on the type of system and molecule used, but herein the discussion will be limited to phosphonic acid (PA) based SAMs as they are the focus of this dissertation. The most commonly used assembly method for PA-based SAMs is known as immersion assembly. Typically a relatively low concentration of SAM (~0.1 mM) is dissolved in an organic solvent such as ethanol or tetrahydrafuran. The solution is then filtered and a clean hydroxylated substrate is placed within the solution. The substrate is then allowed to sit in the solution for 16-48 hours as the chemical reaction is allowed to proceed. Daniel K. Schwartz et al. has characterized the growth mechanism of octadecylphosphonic acid (ODPA) on sapphire which is described as nucleation and growth of islands until complete coverage is obtained [65]. Substrates are then cleaned to remove any non-covalently bound aggregate via rinsing or sonication in fresh solvent used for the initial dissolution. Depending on the SAM, sometimes a more vigorous cleaning procedure is needed for the removal of unbound surface aggregates. In this case, a mixture of the initial solvent and a slightly basic solvent such as trimethylamine (TEA) are mixed in a volume ratio of around 95:5 (main solvent: TEA) and the substrates are sonicated in said solution [66]. In this case, the basic TEA will interact with the unbound phosphonic acid anchor groups and allow for the removal of unbound aggregate.

One major disadvantage of immersion procedure is the extended assembly time which is generally not considered compatible with scalable operations. In order to alleviate this issue a higher concentration (> 1 mM) rapid assembly technique has been developed which utilizes either spin-casting or micro-contact printing. A spin-cast process procedure involves placing a SAM in solution, usually an order of magnitude or higher concentration than that used for immersion assembly, followed by spin-coating the SAM onto the substrate. The substrate is then annealed which allows the thin film SAM layer to fill in any voids or pin poles present [66]. The film is then cleaned leaving only behind the SAM that is chemically bound to the surface for the creation of a

uniform, densely packed monolayer. Stamping involves drop-casting SAM material onto a patterned PDMS stamp and then firmly pressing said stamp onto a substrate. The SAM then makes contact with only the areas which touch the substrate allowing for patterned SAM formation. A similar annealing/cleaning procedure used for spin-cast SAMs is then used to complete the monolayer formation [46]. The development of rapid, low-cost, high throughput methods of SAM assembly greatly enhances the potential for SAMs to be used as a medium of interface modification for commercial organic electronic devices.

While immersion, spin-casting, and micro-contact printing have been developed for the assembly of PA-based SAMs on typical metal oxides, an alternative technique has been developed for the assembly of such SAMs on SiO_2. As discussed previously, PA-based SAMs have limited reactivity with the surface silanol groups due to the mixed acidity of Si-OH (pK_a of about 4.5 and 8.5) [37]. The ratio of acidic and basic silanol groups is about 1:4 respectively [37] which explains the poor PA-based monolayer formation on SiO_2 surfaces. The exact origin of this bimodal acidity in silanol surfaces is still debated [67, 68], but recent theoretical calculations suggest one possible origin is related to the planarity of the silanol group which dictates whether it accepts or donates a hydrogen bond [69]. In order to assemble a PA-based SAM on SiO_2, an alternative approach known as tethering by aggregation and growth (T-BAG) has been developed by the Schwartz group [23]. This process involves suspending a substrate vertically in a high concentration (1 mM) solution of SAM in THF and allowing the solvent to solvent evaporate over 3 hours. The SAM then physisorbs to the substrate which is then annealed at 140 °C for 48 hours to induce chemisorption. After this process the substrate is cleaned in a similar manner as other methods with sonication to remove any unbound aggregates. This process has been further optimized and it has been found that the reaction depends highly on the relative humidity of the environment. According to Thissen et al. the reaction to form Si-O-P bidentate bonds between silanol and PA-based SAMs can occur in as little as 1 sec so long as relative humidity is kept below 16% [70]. This advancement in processing to allow for the rapid formation of PA-based SAMs on the most widely used oxide (SiO_2) in the electronics industry is invaluable towards progressing their commercial use.

2.2.6 *Importance of Solvent on SAM Assembly*

It is important to note that one critical factor for the assembly of SAMs is the solvent environment in which it is assembled. It has been reported that in order to form dense full coverage monolayers via spin-coating on an oxide surface the SAM solution should consist of a nonpolar solvent with a dielectric constant between 3 and 5 [43, 71]. It is argued that the polar phosphonic acid anchor group will become concentrated at the interface of the nonpolar solvent and hydrophilic substrate surface which allows for the assembly of a full coverage monolayer given a sufficiently high SAM concentration. It is speculated that when the chosen solvent has too high of a polarity the SAM will start to interact with the solvent and thus prevent the PA anchor group from interacting with the substrate surface. Alternatively it is suggested if the polarity is too low the polar anchor groups will interact with each other and form reverse micelles [43]. This has been further elaborated by Chen et al. who showed that the solvent interaction with the substrate surface plays a major role in determining the quality of the SAM formed [72]. However, while sufficiently important for the spin-casting technique of SAM assembly, it has recently been shown and is further described in this dissertation that the negative consequences of a polar solvent such as dimethyl sulfoxide can be overcome with the application of heat during assembly [57].

Chapter 3. BOTTOM-CONTACT N-TYPE ORGANIC FIELD EFFECT TRANSISTORS ACHIEVED VIA SIMULTANEOUS MODIFICATION OF ELECTRODE AND DIELECTRIC SURFACES

Low-voltage, n-type organic field effect transistors (OFETs) with simultaneously modified bottom-contact (BC) electrodes and dielectric were compared to their top-contact (TC) counterparts. The devices modified with 6-phenoxyhexylphosphonic acid (Ph6PA) self-assembled monolayer (SAM) showed similar performance, morphology, and contact resistance. Electron mobility of C_{60} devices were 0.21 and 0.32 $cm^2\ V^{-1}\ s^{-1}$ and [6,6]-phenyl-C61-butyric acid methyl ester (PCBM) devices were 0.04 and 0.06 $cm^2\ V^{-1}\ s^{-1}$ for TC and BC devices, respectively. Low contact resistance between 11 and 45 kΩ cm was found regardless of device architecture or n-type semiconductor used. This work shows it is possible to fabricate solution processable low-voltage bottom-contact devices with performance that is similar or better than their top-contact counterparts without the addition of complex and time-consuming processing steps. A modified version of this chapter can be found published as a peer-reviewed article in Organic Electronics [44].

3.1 INTRODUCTION

Organic field effect transistors (OFETs) have the potential to reach commercialization for a wide variety of applications such as active matrix display circuitry [73-75], chemical and biological sensing [76, 77], radio-frequency identification (RFID) devices [78] and flexible electronics [79]. In order to be commercially competitive with already at-market amorphous silicon devices, OFETs need to approach similar performance levels by achieving mobility greater than 1 cm^2 V^{-1} s^{-1} while under low voltage operation. Significant process has been made in developing high performance organic semiconductors (OSCs) [80, 81] and dielectric materials [82-84]. However, these devices usually employ top-contact (TC) geometry, which is not compatible with conventional photolithography typically due to the incompatibility between the photoresist developer and stripper which can cause degradation of the OSCs. Bottom-contact (BC) organic devices are generally not used due to diminished performance compared to TC devices resulting from the incompatibility between the OSC and the metal electrode and dielectric interfaces [85, 86]. Using self-assembled monolayers (SAMs), one is able to enhance BC OFET device performance by controlling OSC morphology [87-89] or modifying the electronic structure at the metal/semiconductor interface [90-92].

Recently it has been shown that through a simple spin-cast procedure one is able to simultaneously modify the source/drain metal electrodes and metal oxide dielectric with simple alkyl phosphonic acid SAMs [45]. This dual modification allows for the passivation of surface hydroxyl groups that can act as electron traps at the dielectric interface [93], a reduction of Frölic polaron formation between charge carriers in the OSCs [94] caused by the SAM acting as a physical buffer against the induced ionic polarization from a high-k material used for low-voltage applications [41] as well as reduction of the source/drain contact resistance due to SAM-modified metal/OSC interface [95]. However, alkylphosphonic acid SAMs are not compatible with solution-processable small-molecule OSCs due to the low surface energy of methyl-terminated SAMs which causes limited surface wettability. In particular, soluble small-molecule OSCs, such as [6,6]-phenyl-C61-butyric acid methyl ester (PCBM), are typically unable to form thin films on low surface energy substrates resulting in significantly reduced or no device performance [41].

In this chapter we investigate the effect of 6-phenoxylhexylphosphonic acid (Ph6PA) SAM on top- and bottom-contact low-voltage n-type organic OFETs. C_{60} and PCBM were chosen as the

semiconductors in order to compare the effect that Ph6PA SAM plays on OFET device performance, morphology, and contact resistance on solution-processed and thermally evaporated small-molecule n-type materials.

3.2 EXPERIMENTAL

3.2.1 *Synthesis of 6-phenoxyhexylphosphonic acid (Ph6PA)*

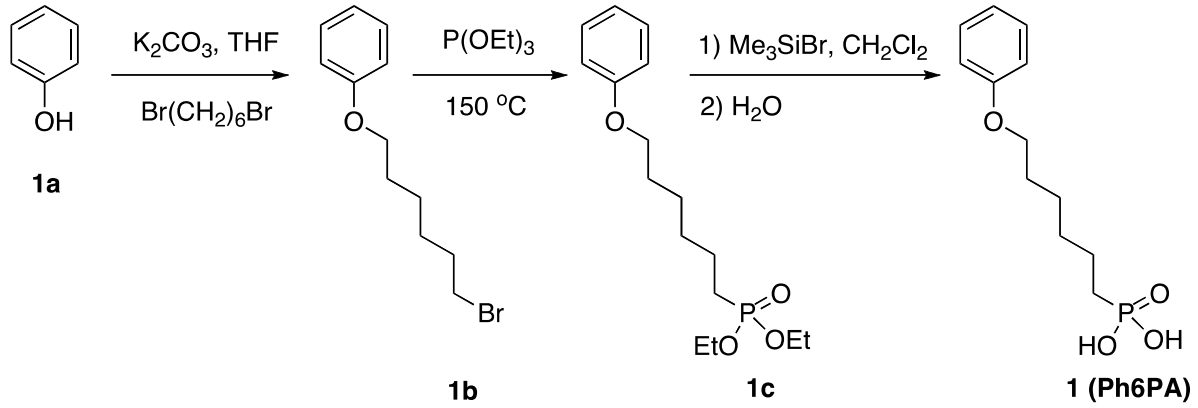

Figure 3.1. Synthesis of 6-phenoxyexylphosphonic acid. Reprinted with permission from [44]. Copyright 2012, Elsevier Limited.

Synthesis of Ph6PA was completed by Professor Hong Ma. All chemicals were purchased from Aldrich or TCI America, and used as received unless otherwise specified. Tetrahydrofuran (THF) was distilled under nitrogen from sodium with benzophenone as the indicator. Methylene chloride was distilled over P_2O_5. ^1H NMR spectra (300 MHz) were taken on a Bruker-300 FT NMR spectrometer with tetramethylsilane (TMS) as internal reference. Elemental analysis was determined at QTI (Whitehouse, NJ). ESI-MS spectra were obtained on a Bruker Daltonics Esquire Ion Trap Mass Spectrometer.

6-Bromohexoxybenzene (1b): To a solution of phenol (1.88 g, 20.0 mmol) and 1,6-dibromohexane (4.88 g, 20.0 mmol) in dry THF (50 mL) under nitrogen was added potassium carbonate (4.15 g, 30.0 mmol). The mixture was stirred for 20 h under reflux, cooled down to

room temperature and filtered to remove insoluble salts. The filtrate was concentrated by rotary evaporation under reduced pressure. The crude product was purified over silica gel column chromatography with hexane/methylene chloride (3:1) as the eluent to afford a colorless liquid (2.89 g, 56%). ^{1}H NMR (300 MHz, $CDCl_3$): δ 7.24-7.31 (m, 2H), 6.87-6.94 (m, 3H), 3.96 (t, 2H, J = 6.3 Hz), 3.42 (t, 2H, J = 6.6 Hz), 1.47-1.93 (m, 8H). $C_{12}H_{17}BrO$: Calcd C 56.04, H 6.66, Br 31.07; Found C 55.91, H 6.74, Br 31.18. ESI-MS (*m/z*): Calcd. 256.1; Found 256.0.

Diethyl 6-phenoxyhexylphosphonate (1c): A mixture of 1b (1.29 g, 5.0 mmol) and triethyl phosphite (9.55 g, 53.5 mmol, 10.0 mL) was heated under nitrogen at 150 °C for 17 h. The excess of triethyl phosphite was removed by distillation under vacuum. The crude product was purified over silica gel column chromatography with methylene chloride to methylene chloride/ethyl acetate (1:1) as the eluents to afford a colorless liquid (1.28 g, 82%). ^{1}H NMR (300 MHz, $CDCl_3$): δ 7.24-7.31 (m, 2H), 6.86-6.94 (m, 3H), 4.05-4.13 (m, 4H), 3.95 (t, 2H, J = 6.3 Hz), 1.44-1.82 (m, 10H), 1.32 (t, 6H, J = 6.9 Hz). $C_{16}H_{27}O_4P$: Calcd C 61.13, H 8.66, P 9.85; Found C 61.01, H 8.79, P 9.74. ESI-MS (*m/z*): Calcd. 315.2; Found 315.2.

6-Phenoxyhexylphosphonic acid (1, Ph6PA): To a solution of 1c (0.629 g, 2.0 mmol) in dry methylene chloride (15 mL) under nitrogen was dropwise added bromotrimethylsilane (1.84 g, 1.55 mL, 12.0 mmol). The mixture was stirred overnight at room temperature. The reaction mixture was poured into water (200 mL), filtered and washed with large amount of water to collect a white solid (0.453 g, 88%). ^{1}H NMR (300 MHz, $CDCl_3$): δ 7.24-7.32 (m, 2H), 6.85-6.94 (m, 3H), 3.95 (t, 2H, J = 6.3 Hz), 1.45-1.84 (m, 10H). $C_{12}H_{19}O_4P$: Calcd C 55.81, H 7.42, P 11.99; Found C 55.67, H 7.59, P 11.82. ESI-MS (*m/z*): Calcd. 258.3; Found 258.3.

3.2.2 *Device Fabrication*

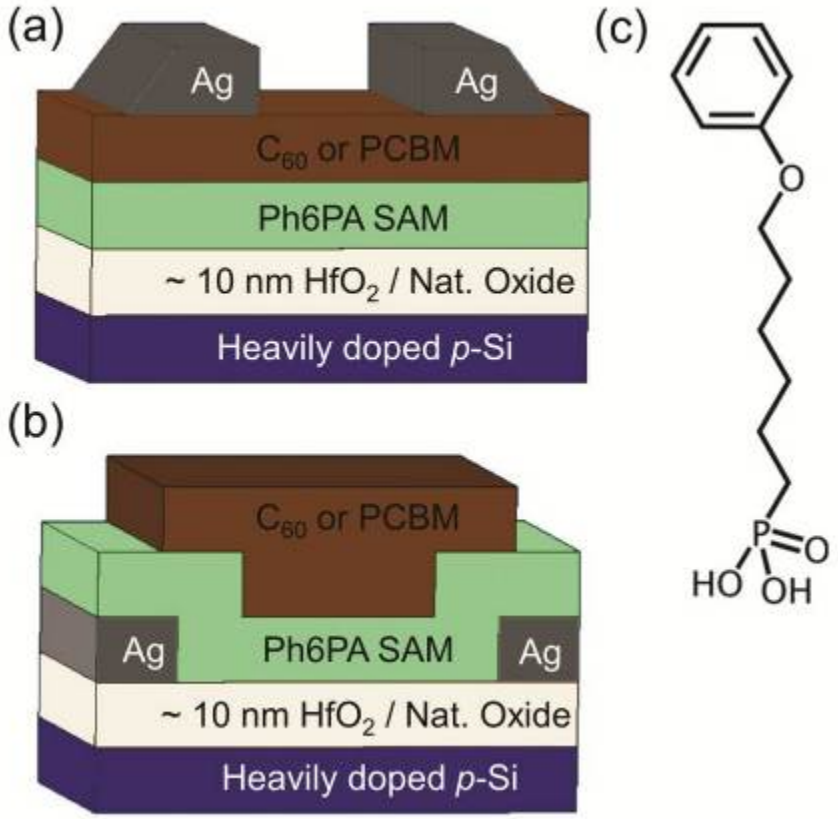

Figure 3.2. Device architecture and molecular structure of Ph6PA SAM (a) Top- and (b) bottom-contact bottom-gate device architectures used in this study and (c) 6-phenoxyhexylphosphonic acid (Ph6PA) self-assembled monolayer molecule. Reprinted with permission from [44]. Copyright 2012, Elsevier Limited.

OFETs were fabricated with device architectures indicated in Fig. 3.2. Hafnium oxide (HfO_2) sol-gel dielectric was prepared on cleaned heavily p-doped silicon with a native oxide layer as described by our group previously [41]. Source and drain electrodes were patterned with shadow masks via thermal deposition of 40 nm thick silver at a rate of 0.4 Å/s under a vacuum of 5E-7 Torr. A spin-coating assembly process for Ph6PA was developed from an adapted procedure by Nie *et* al [71]. A 3 mM Ph6PA solution was prepared in dry and degassed chloroform and tetrahydrofuran (THF) in a 1:4 by volume solvent ratio. The solution was subsequently sonicated for 10 minutes, filtered with a 0.2 µm PTFE filter, dispensed onto prepared substrates in air, left

to sit for 10 seconds, then spun at 3000 rpm for 30 seconds. Substrates were then annealed at 120 °C for 10 minutes in a dry N_2 environment, cooled to room temperature, then rinsed extensively with anhydrous dimethylformamide:triethylamine (95:5 by volume), THF, and hexanes. [6,6]-Phenyl-C_{61}-butyric acid methyl ester > 99% (Sigma-Aldrich) was dissolved in anhydrous dichlorobenzene at 0.1 wt%, filtered with a 0.2 μm PTFE filter, and then spun-cast at 1200 rpm with a 500 rpm/s ramp rate for 60 seconds. 40 nm thick C_{60} 99.9% sublimed (Sigma-Aldrich) was thermally evaporated in a quartz crucible at a rate of 0.2 Å/s at 5E-7 Torr through patterned shadow masks onto prepared substrates maintained at a temperature of 50° C. HfO_2, SAM, and OSC deposition and assembly were completed at the same time using the same solution batches regardless of the device architecture in order to minimize experimental errors due to small variations in individual batches.

3.3 Results and Discussion

In order to reduce the barrier to commercialization of organic electronics it is necessary to find processes that are compatible with current manufacturing standards such as photolithography while still being able to take advantage of the inherent strengths of organic electronics such as roll-to-roll processing. Top-contact organic transistors are generally not compatible with photolithography due to the incompatibility between the organic semiconductor and photoresist used for patterning. Although bottom-contact transistors are compatible with photolithographic processing, their device performance is significantly reduced because of the incompatibility between the metal electrode and organic semiconductor. Control of the metal/organic interface of organic transistors is needed in order to overcome the challenges presented in bottom-contact devices. Equally important is limiting the resistance at the source and drain electrodes in order to achieve high performance while maintaining compatibility with solution-processed organic semiconductors and using minimal processing steps.

3.3.1 *Rationale of SAM Molecular Design*

Ph6PA was designed by carefully selecting each individual component of the SAM in order to achieve desirable properties. The SAM can be divided into three functional parts: binding group,

spacer unit, and terminal group (Fig. 3.2c). Phosphonic acid was chosen as the binding moiety due to its ability to react with a wide range of metal oxides [96]. Further advantages such as higher thermal stability [97], not being limited by surface hydroxyl content [23], and a lack of homocondensation between phosphonic acids [34] make it an ideal binding group over the more traditionally used chlorosilanes. A short alkyl chain was used as a spacer to act as a relatively flexible core and allow the SAM to compensate for variations in surface roughness [98]. Finally, the phenoxy terminal group acts to control the surface energy due to more polarizable phenyl ring and polar ether compared to methyl terminal group, and result in suitable surface energy allowing for compatibility with solution-processed small-organic semiconductors because of better surface energy matching [99]. The combination of van der Waals interactions between alkyl chains and π-π stacking of phenyl rings should allow for the formation of a densely packed monolayer. Additionally, the overall length of the molecule was limited in order to reduce the added resistance that occurs when long-chain SAMs treat the metal electrodes [45, 95]. Theoretical calculations using Jmol 13.0.4 show Ph6PA SAM to be comparable in length at 1.084 nm to octyl-phoshonic acid, a molecule that has previously been shown to not add significant contact resistance when modifying electrodes [45].

3.3.2 *Characterization of SAM Treated Surfaces (AFM and Contact Angle)*

The morphology of Ph6PA SAM modified HfO_2 dielectric surface and Ag source/drain electrodes were characterized via tapping mode atomic force microscopy (AFM). Ph6PA treated HfO_2 surface resulted in a smooth, uniform film with an average RMS roughness of 0.22 nm which is comparable to untreated HfO_2 and the underlying SiO_2 substrate. The smooth Ph6PA-treated surface is indicative of monolayer formation. Untreated bottom-contact Ag source/drain electrodes had an RMS roughness of about 7 nm and did not change with SAM treatment. A contact angle goniometer was used to determine the water contact angles of Ph6PA treated surfaces. Both Ph6PA SAM treated HfO_2 and Ag yielded similar water contact angles of 83° and 85° respectively. Untreated Ag and HfO_2 films had water contact angles of 55° and less than 10° respectively. All contact angle measurements results are averages of at least three different water droplets and are within 3° of each other indicating uniform film coverage.

3.3.3 *Spectral Characterization of SAM Treated Surfaces (NEXAFS)*

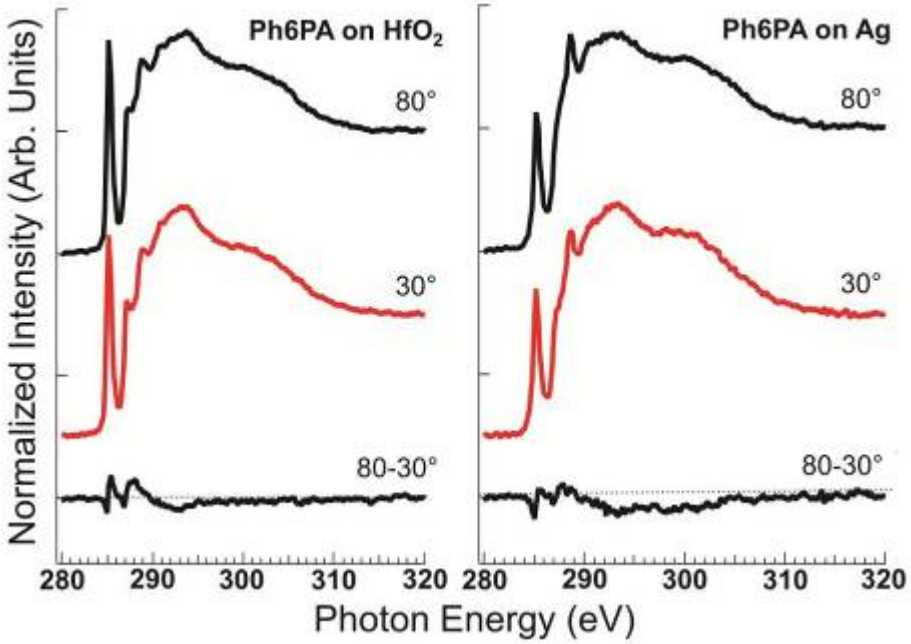

Figure 3.3. NEXAFS carbon K-edge spectra acquired at 30° and 80° from Ph6PA assembled on HfO2 (left panel) and Ag (right panel). The difference spectra between the 80° and 30° data is also shown. Reprinted with permission from [44]. Copyright 2012, Elsevier Limited.

In order to determine information related to Ph6PA SAM order, near edge x-ray absorption fine structure (NEXAFS) spectroscopy was obtained. All NEXAFS spectra, taken from Ph6PA on Ag and HfO2, were collected at the U7A beamline at the National Synchrotron Light Source (NSLS, Brookhaven National Laboratory, Upton, NY). The beamline is equipped with a monochromator and a 600 l/mm grating that provides a full-width at half maximum energy resolution of ~ 0.15 eV at the carbon K-edge (285 eV). A detector with bias voltages set at -150 V for the C K-edge, monitored partial electron yields which were divided by the beam flux during data acquisition [100]. All samples were mounted to allow rotation about the vertical axis, thus, allowing the NEXAFS angle, the angle between the incident X-ray beam and the sample surface, to change.

Pre- and post-edge normalized NEXAFS spectra, collected at x-ray incidence angles of 30° and 80°, can be found in Fig. 3.3. The spectra collected from the monolayer assembled on both Ag and HfO_2 contain identical spectral features. The pre-edge π* resonance at 285.3 eV is representative of aromatic C=C bonds stemming from the monolayer's phenyl rings [101, 102]. Moving to higher photon energies we observe resonances at 288 eV and 293 eV related to R*/C–H * and C–C *, respectively [101-103]. The orientation or ordered molecular bonds are determined by tracking the change in the x-ray absorption as we vary the x-ray incident angle. Then based on the observed polarization dependence can be used to calculate tilt angles of specific bonds within the monolayer [104]. However, for the Ph6PA monolayers on Ag and HfO_2, we observe no polarization dependence (Fig. 3.3, 80-30), demonstrating no ordering or unique tilt angle of either the hydrocarbon chains or the phenyl rings.

3.3.4 *Top- and Bottom-Contact OFET Device Performance*

HfO_2 dielectric properties were determined by fabricating metal/insulator/metal (MIM) junctions using the bottom degenerately doped *p*-type Si as a global contact and patterned Au as a top contact. An Agilent 4284A LCR meter was used to characterize untreated HfO_2 MIM junctions which had an average capacitance of 636 nF cm^{-2} while Ph6PA treated HfO_2 yielded an average value of 590 nF cm^{-2}. Current density versus voltage at ±2 V for SAM treated and untreated MIM junctions were comparable at 4E-9 A cm^{-2}.

Table 3.1. Averaged performance data of C_{60} and PCBM OFETs with top-contact (TC) and bottom-contact (BC) device architecture OFETs using spin-cast HfO_2 dielectric and Ag source/drain electrodes. Ph6PA SAM modification is done on the electrodes and dielectric for BC devices while just the dielectric is modified for TC devices. Data are from an average of 8 measured transistors for each channel length per device architecture over two separate batches.

		μ [$cm^2\ V^{-1}\ s^{-1}$]	V_{th} [V]	S [$mV\ dec^{-1}$]	I_{on}/I_{off}	R_{sd} [kΩ cm]
C_{60}	TC	0.212 ± 0.081	2.06 ± 0.03	135 ± 13	10^5	34.5
	BC	0.320 ± 0.081	1.85 ± 0.06	146 ± 23	10^6	11.6
PCBM	TC	0.040 ± 0.003	2.32 ± 0.02	150 ± 17	10^5	14.9
	BC	0.063 ± 0.007	2.20 ± 0.01	129 ± 13	10^5	45.5

Top and bottom contact transistors with the structures listed in Fig. 3.2 were characterized with an Agilent 4155B semiconductor parameter analyzer in a dry N_2 environment. C_{60} and PCBM transistors yielded comparable performance between their respective top- and bottom-contact device architectures (Fig. 3.4). The field effect mobility was determined from the slope of a linear fit of $(I_{ds})^{1/2}$ vs. V_{gs} while the threshold voltage (V_t) was estimated as the intercept at the x-axis of the same linear fit. All devices exhibited little to no hysteresis, subthreshold swing values between 120-180 mV $decade^{-1}$, and I_{on}/I_{off} ratios between 10^5 and 10^6. Averaged device data is tabulated in Table 3.1. It is important to note that devices were also fabricated without SAM modification which resulted in no measureable device performance. This lack of performance may be attributed to the strong ionization potential of hafnium oxide [41] or the sensitive nature of n-type materials to charge traps present on the dielectric surface [93, 105].

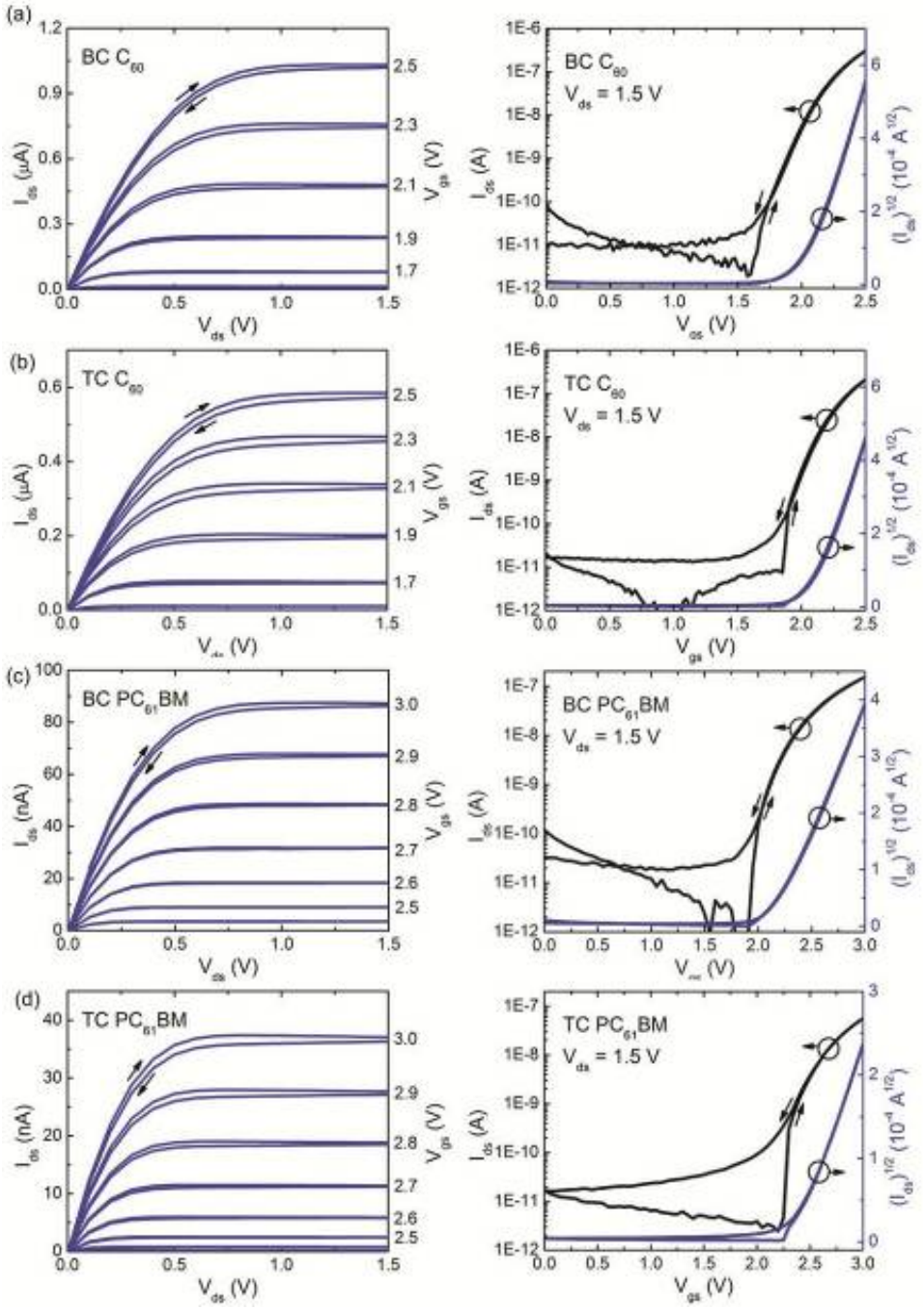

Figure 3.4. Electrical characteristics of OFETs fabricated in this study. Representative output (left) and transfer (right) curves for Ph6PA modified (a) BC C_{60} and (b) TC C_{60} devices (L = 80 μm, W = 1000 μm) and (c) BC PCBM and (d) TC PCBM devices (L = 100 μm, W = 1000 μm). Reprinted with permission from [44]. Copyright 2012, Elsevier Limited.

AFM was used to characterize the semiconductor morphology of tested devices and better understand the underlying effect of Ph6PA on small molecule OSC morphology (Fig. 3.5). C_{60} SAM-treated devices have similar grain size regardless of architecture, while untreated HfO_2 surfaces resulted in significantly smaller grains. RMS roughness of C_{60} for BC SAM-treated, TC SAM-treated, and untreated HfO_2 are comparable at 1.86 nm, 1.97 nm, and 1.96 nm respectively.

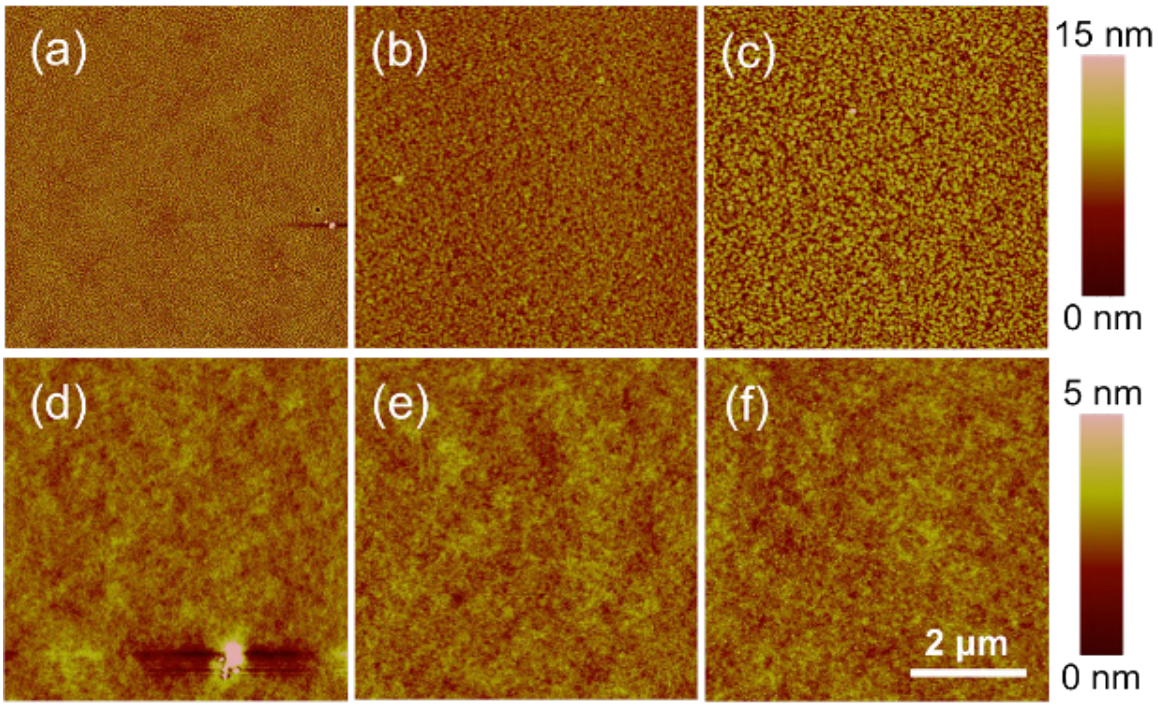

Figure 3.5. AFM Morphology of C_{60} and PCBM based on SAM treatment and device architecture. C_{60} (a) and PCBM (d) semiconductor morphology on untreated HfO_2. Bottom- and top-contact semiconductor morphology of C_{60} devices (b and c) and PCBM devices (e and f) on Ph6PA treated HfO_2. Reprinted with permission from [44]. Copyright 2012, Elsevier Limited.

The significantly larger C_{60} grain size for SAM-treated surfaces suggests an improved compatibility between C_{60} and the underlying SAM-treated dielectric. PCBM morphology is characterized as smooth amorphous films for BC SAM-treated, TC SAM-treated, and untreated HfO_2 surfaces with RMS roughness values of 0.34, 0.37, 0.29 nm respectively. It is important to note that due to the limited interaction between PCBM and HfO_2, PCBM would fail to form a thin-film unless it was first drop-cast onto HfO_2 for 60 seconds followed by the spincoating procedure

described previously. Such an issue does not occur for SAM-treated surfaces which may be indicative of a π-π interaction between PCBM and the phenyl ring of Ph6PA SAM allowing for enhanced adhesion.

3.3.5 *Device Contact Resistance*

In order to better understand the performance differences between top- and bottom-contact devices the transmission line method (TLM) was used to determine contact resistance [105]. The TLM calculates the series resistance of the source and drain electrodes across the channel length of a set of transistors. One is able to determine contact resistance based on the change of slope in the linear region of the output curve as the gate-source voltage is changed while the drain-source voltage is held constant. In order to minimize experimental error and obtain the most accurate measurement of total resistance a MATLAB ® script file was written which utilizes the least mean squares method to determine the fit of the linear region of the output curve with an R^2 value greater than 0.98 and containing at least 10 measured data points.

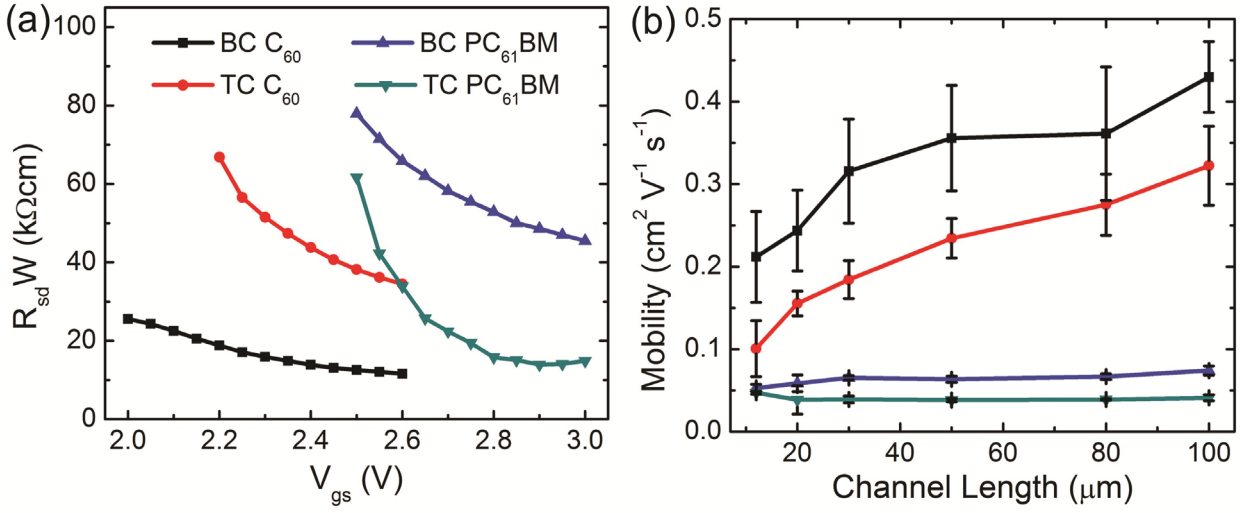

Figure 3.6. Contact resistance and electron mobility of fabricated devices based on device architecture and semiconductor. (a) Contact resistance as a function of gate-source voltage for Ph6PA modified devices with varying geometry and (b) averaged mobility for each tested channel length. Reprinted with permission from [44]. Copyright 2012, Elsevier Limited.

All devices exhibited expected contact resistance trends with an exponential increase towards V_t while saturating when sufficiently far from the threshold voltage as the gate-source voltage increased (Fig. 3.6). Additionally, the contact resistance for all device architectures were similar and of the same order of magnitude ranging from 11 kΩ cm to 45 kΩ cm. Typically it is expected that contact resistance between staggered (TC) and planar (BC) transistor device geometries is significantly different when a charge injection barrier height is present. Theoretical calculations show that contact resistance diverges by orders of magnitude between the two device architectures when the injection barrier height is greater than 0.3 eV [106]. For this reason it is speculated that one of the functions of the Ph6PA SAM is to help reduce the electron injection barrier height present when using electrodes with relatively high work functions such as Ag.

A possible mechanism that caused this reduced electron injection barrier could be due to the dipole effect of the Ph6PA SAM. Top-contact PCBM transistors using TiO_2 as a charge injection layer between PCBM and Al source/drain electrodes have resulted in similar performance in terms of mobility and contact resistance. The strong dipole present at the TiO_2 surface results in a reduction of the electron injection barrier and allows for performance similar to devices utilizing calcium electrodes [107]. Additionally, the constant surface energy across dielectric and source/drain electrodes due to SAM treatment of BC devices helps to minimize defects. Different semiconductor morphologies can result when the source/drain electrodes and dielectric material have different surface energies and can cause significant defects at that interface [108]. This control over the semiconductor morphology based on the underlying SAM present on both the dielectric and electrode allows for enhanced performance.

Overall, a very limited difference is seen between Ph6PA treated devices with top- and bottom-contact geometries. Similar performance, morphology, and contact resistance is indicative that this particular SAM effectively serves to reduce the limitations caused by different device architectures.

3.4 CONCLUSION

In conclusion, through rational molecular design and process optimization a SAM has been developed to simultaneously modify both source/drain electrodes and metal oxide dielectric surfaces and be compatible with solution processable and thermally evaporated organic semiconductors. Our results show comparable performance between top- and bottom-contact device architectures with an average electron mobility of C_{60} TC and BC devices of 0.212 and 0.320 $cm^2\ V^{-1}\ s^{-1}$ respectively. PCBM devices yielded 0.04 and 0.06 $cm^2\ V^{-1}\ s^{-1}$ for TC and BC devices respectively. Low contact resistance between 11 and 45 kΩ cm was found regardless of device architecture or *n*-type semiconductor used. Through this simultaneous SAM modification photolithography compatible and solution processed semiconductor-based OFET devices are achievable without being inhibited by the performance degradation that typically accompanies the bottom-contact device architecture.

Chapter 4. UNDERSTANDING THE ROLE OF SELF-ASSEMBLED MONOLAYERS ON GRAPHENE TRANSISTORS

4.1 Influence of Self-Assembled Monolayer Binding Group on Graphene Transistors

Graphene transistors on self-assembled monolayer (SAM) modified dielectric substrates were fabricated and characterized in order to determine the influence SAM binding group has on device properties. It was found that silane based alkyl SAMs had little to no influence in doping graphene transistors while phosphonic acid based ones caused n-type doping of graphene transistors with a charge neutrality point shift of over ten volts. It was also discovered that alkyl SAM packing density influenced the doping magnitude. Due to substrate surface charge trap quenching, these SAMs independent of binding group enhanced charge mobility of graphene transistors compared to ones on bare oxide substrates. A modified version of this section can be found published as a peer-reviewed article in Applied Physics Letters [109].

4.1.1 *Introduction*

Graphene is a two-dimensional material with promising electrical and optical properties that have been explored extensively [110, 111]. Electron mobility as high as 200,000 $cm^2V^{-1}s^{-1}$ can be achieved once extrinsic factors such as scattering centers form underlying substrates, adsorbates, and defects within graphene itself are controlled [112-115]. However, in order to achieve commercial viability it is necessary to have precise control over the electrical properties of graphene to cater to the specific needs of device applications. Of particular interest is control of graphene doping which directly influences the position of the charge neutrality point. Graphene doping has been accomplished in a variety of ways such as surface chemical doping [116], substitutional doping [117], electrical field modulation [118], and metal contact doping [119]. Recent reports have also shown that self-assembled monolayers (SAMs) are capable of doping graphene as well as enhance graphene transistor charge mobility by limiting the interactions between graphene and substrate surface trap states [49, 50, 120, 121].

While much emphasis has been placed on examining the influence of the SAM functional group on the properties of graphene; the influence of SAM binding group is often overlooked. A recent report [52] has elucidated the fact that the SAM binding group can play a considerable role in influencing the properties of low voltage organic thin-film transistors. In this study we utilize

the two most commonly used SAM binding groups to demonstrate their effect on the properties of graphene-based transistors.

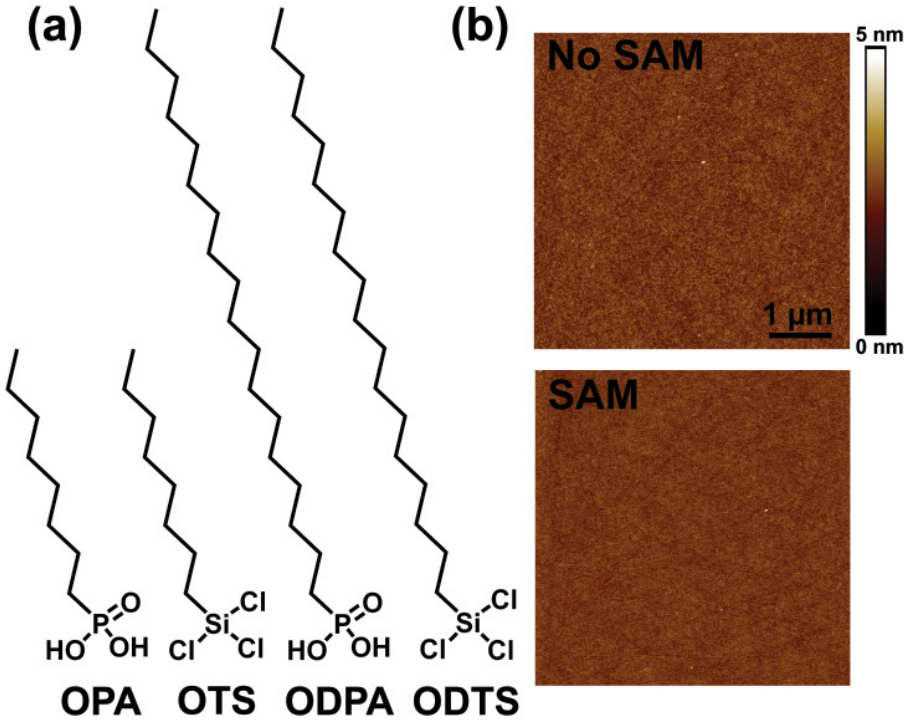

Figure 4.1. SAM structure and representative morphology. (a) Chemical structures of the SAMs used in this study. (b) Representative morphology of AlO_x substrate without SAM (top) and SAM modified AlO_x substrate determined via atomic force microscopy. Image z-scale is 5 nm. Reprinted with permission from [109]. Copyright 2015, AIP Publishing LLC.

In order to understand the influence of the SAM binding group and minimize the effect of the SAM functional group, carefully selected SAMs were used in this study. The SAM molecule design can be separated into two parts: the binding group, which covalently bonds to a metal oxide surface, and the functional group that can be designed to serve a variety of purposes. In this section, we have chosen to use alkyl chains to minimize extrinsic effects caused by the SAM functional group due to their lack of polarity. In addition, we have selected to utilize both 8- and 18-carbon long alkyl chains since it is known that the SAM packing density increases as the number of carbon molecules in an alkyl chain increases due to the additive nature of van der Waals interactions [122]. A schematic of the SAMs used can be seen in Figure 4.1, which are octadecylphosphonic acid

(ODPA), octylphosphonic acid (OPA), octadecyl trichlorosilane (ODTS), and octyl trichlorosilane (OTS).

4.1.2 *Experimental*

4.1.2.1 *Preparation and Assembly of Phosphonic Acid and Silane Molecules*

SAMs were assembled on 2-3 nm AlO_x/300 nm SiO_2/heavily p-doped Si substrates which were cleaned as described previously [44]. The AlO_x layer was used as an adhesion layer in order to promote the covalent bonding between the phosphonic acid based SAMs and the substrate [46]. Assembly of phosphonic acid molecules occurred via immersion assembly in ambient conditions with substrates being placed in a filtered 0.1 mM solution of tetrahydrofuran (THF) and ethanol (EtOH) (1:1 ratio by volume) for 18 hours. Substrates were then annealed for 15 minutes at 110 °C in air, allowed to cool to room temperature, and sonicated in THF and EtOH for 15 minutes. Silane based SAMs were assembled from a modified procedure [50] with substrates being immersed for 3 hours in a filtered 5 mM solution of silane molecules in anhydrous trichloroethylene while under an inert nitrogen environment. Substrates were then annealed for 10 minutes at 110 °C, allowed to cool to room temperature, removed from the nitrogen environment, and cleaned via sonication in acetone and toluene for 15 minutes.

4.1.2.2 *Device Fabrication*

CVD monolayer graphene was grown on copper foil at 990 °C as described elsewhere [123]. Poly(methyl methacrylate) (PMMA) was then spun-cast on top of the graphene layer and the copper film was etched away using an aqueous ammonium persulfate solution leaving only graphene supported by PMMA floating in solution. Graphene/PMMA was then rinsed in several baths of deionized water followed by the films being transferred to the SAM treated dielectrics. PMMA was then removed from the graphene/SAM/dielectric substrates with extensive cleaning in acetone and isopropyl alcohol. Devices were subsequently placed under high vacuum and top-contact gold electrodes were evaporated through a shadow mask followed by annealing for 2 hours under a dry nitrogen environment at 200 °C.

4.1.3 *Results and Discussion*

4.1.3.1 *AFM and Contact Angle Characterization of SAM Treated Surfaces*

Atomic force microscopy (AFM) and contact angle goniometry were used to characterize each SAM assembled on AlO_x/SiO_2 surface. A Digital Instruments Multimode Nanoscope IIIa scanning probe microscope (Veeco Instruments, Plainview, NY) was used in AFM tapping mode to characterize the topography of the SAMs used in this study. All SAMs show a similar smooth morphology with an RMS roughness between 0.2 and 0.3 nm, which is comparable to the untreated dielectric surface. A representative image of SAM topography compared to the unmodified dielectric surface can be seen in Figure 4.1b. In order to ensure that the SAM had modified the dielectric surface, aqueous static contact angle values were determined with a VCA Optima Surface Analysis System (Adv. Surface Technology Products, Billerica, MA) which resulted in contact angles of 109°, 104°, 106°, and 101° for ODPA, OPA, ODTS, and OTS respectively. This is significantly different than the untreated dielectric which has an aqueous static contact angle of less than 10°. These values are comparable to previously published reports [41, 52]. The standard deviation of contact angle measurements for each SAM is less than 3°, indicating uniform and continuous coverage across the entire dielectric surface. The low RMS roughness and preserved contact angle after extensive sonication in organic solvents post-assembly indicates the formation of a dense and homogenous molecular monolayer that is chemically bound to the dielectric surface and free of physisorbed aggregate.

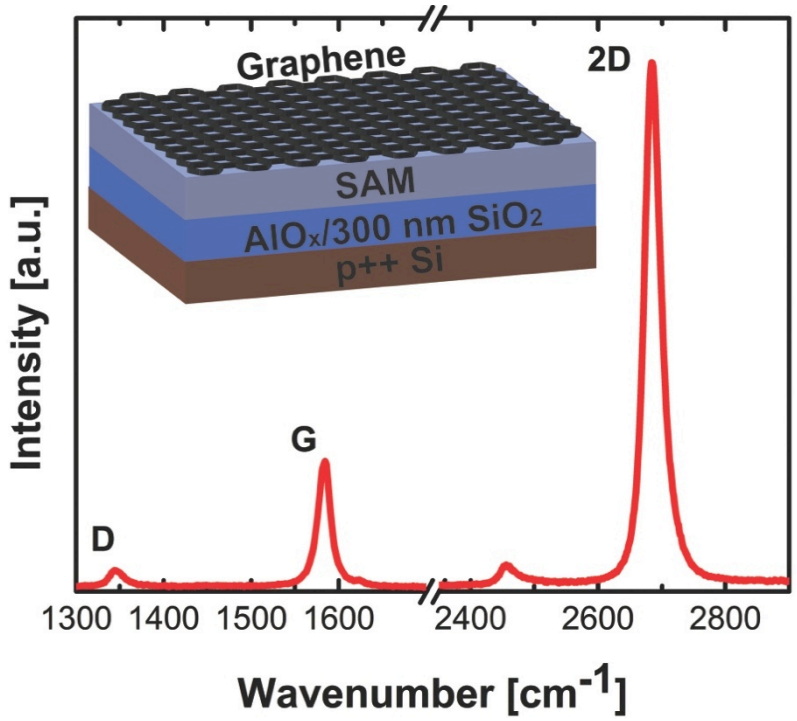

Figure 4.2. Raman spectrum for graphene on SAMs used in this study. (Insert) Schematic of device structure used to characterize graphene. Reprinted with permission from [109]. Copyright 2015, AIP Publishing LLC.

4.1.3.2 *Raman Spectroscopy for Determination of Graphene Quality*

A Renishaw inVia Raman Microscope with 514 nm laser and resolution of 2.5 cm^{-1} was used to determine the quality of graphene on a SAM modified dielectric surface via its characteristic phonon peaks. Figure 4.2 shows a representative Raman spectrum of graphene on the SAM/dielectric. The minimal D peak at (~1350 cm^{-1}) implies high quality graphene with the presence of minimal defects [124]. The 2D peak (~2685 cm^{-1}) is spectrally sharp and its intensity is about four times greater than that of the G peak (~1585 cm^{-1}), which are characteristics of monolayer graphene [125].

4.1.3.3 *SAM-Modified Graphene Transistor Electrical Characterization*

Gold electrode top-contact graphene on SAM-modified AlO_x/300 nm SiO_2 transistors were fabricated. Transistor channel width was 1000 µm while channel length varied between 12 µm and 100 µm. Typical transfer curves of the graphene devices can be seen in Figure 4.3 wherein devices were characterized with a Agilent 4155B semiconductor parameter analyzer under a dry nitrogen environment with a two-point measurement for source and drain electrodes. Graphene devices show little to no hysteresis with the exception of the OTS SAM treated devices and the reference devices without SAM treatment. It is thought that the hysteresis occurs from trapped impurities between the graphene and SAM interface as recently adsorbed water and oxygen molecules have been shown to be the origin of hysteresis in graphene via a redox reaction [126]. It is expected that the reference devices without SAM treatment would have some amount of hysteresis due to the presence of charge traps and impurities at the surface of the untreated dielectric. The hysteresis in OTS may be due to a lower packing density compared to OPA as inferred via the slightly lower water contact angle.

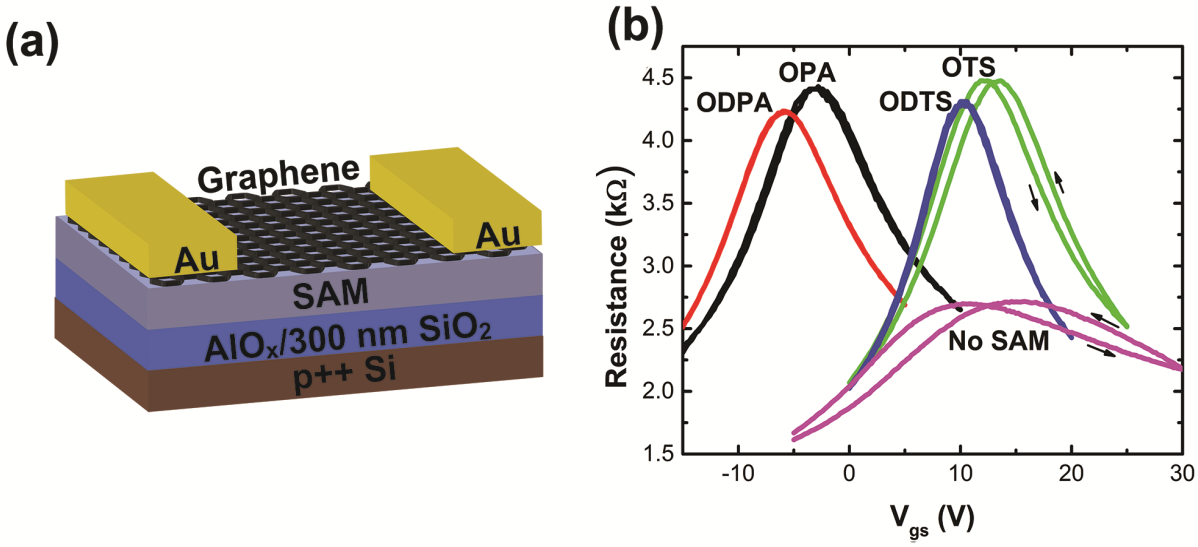

Figure 4.3. Graphene transistor schematic and transfer characteristics. (a) Schematic of graphene transistors fabricated. (b) Representative transfer curves of graphene transistors with SAM on dielectric surface modification compared to an untreated (No SAM)

dielectric graphene transistor. Reprinted with permission from [109]. Copyright 2015, AIP Publishing LLC.

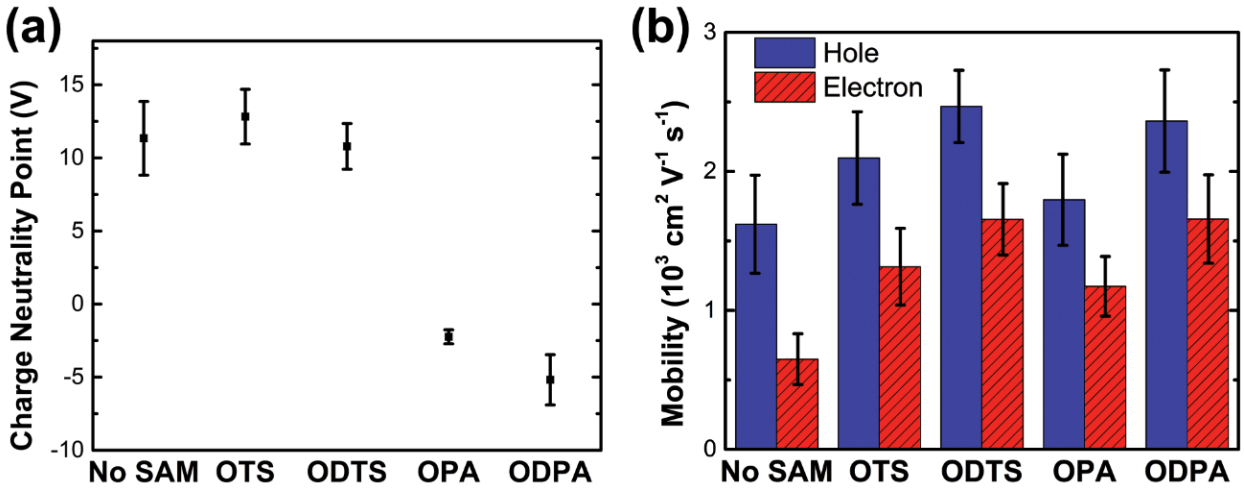

Figure 4.4. Averaged charge neutrality point and mobility of graphene transistors. (a) Averaged charge neutrality point and (b) averaged hole/electron mobility for graphene transistors with (and without) SAM modification characterized in this study. Averaged data are from approximately 30 transistors per device structure. Reprinted with permission from [109]. Copyright 2015, AIP Publishing LLC.

The charge neutrality point (V_D) is defined as the conductivity minimum of the transfer curve. V_D for each tested device was determined and averaged as seen in Figure 4.4a. V_D did not change significantly with respect to tested transistor channel lengths of 12, 20, 30, 50, 80, and 100 μm. A clear trend can be determined from V_D between the different SAMs used and the properties of graphene. In terms of doping, silane based SAMs appear to have little effect on V_D with values comparable to the untreated dielectric. This is a reasonable effect given the chemical similarity of the silane binding group and the underlying hydroxyl moieties present on the untreated device. However, since ODTS has a slightly lower V_D compared to OTS there appears to be some element of n-doping. This slight enhancement may be due to the higher packing density of ODTS, which results in fewer defects within the SAM layer and thus less charge trap states. On the other hand, phosphonic acid based SAMs show a clear n-type doping effect. There is an approximately 10-15 volt negative shift in V_D compared to the OTS, ODTS, and the reference devices. This n-doping effect correlates well with previous reports that show a similar effect for low-voltage organic field-effect transistors [52]. Interestingly, there is also a slight difference in doping effect between the

18-carbon chain alkyl moiety and the shorter 8-carbon chain. Since longer alkyl SAMs have a higher packing density [122] than shorter alkyl SAMs it is speculated that a stronger doping effect will occur since the dopant is at a higher concentration comparatively. Alternatively, this shift could also be due to the slightly higher water contact angle of 18-carbon alkyl SAMs (compared to 8-carbon alkyl SAMs) making devices less susceptible to water or oxygen adsorbents which tend to p-dope graphene. However, since these devices were stored overnight under vacuum followed by annealing and electrical characterization in a dry nitrogen environment it is more likely to be due to an increased dopant density.

The extrinsic mobility of the graphene transistors was determined in order to clarify the extent of which the SAM binding group influences charge transport. The extrinsic field-effect mobility was extracted from the maximum slope near the charge neutrality point with the following equation:

$$\mu_{FET} = \frac{L_{ch}(dI_{ds}/dV_{gs})}{W_{ch}C_{ox}V_{DS}} \qquad (Eq. 4.1)$$

where L_{ch} and W_{ch} is the channel length and width respectively, dI_{ds}/dV_{gs} is determined from the maximum slope near the charge neutrality point of the I_{ds} vs. V_{gs} transfer curve, C_{ox} is the gate-oxide capacitance per area, and V_{DS} is the constant drain-source voltage of the same transfer curve [127]. This methodology is comparable to previously reported methods of determining the mobility of graphene transistors with a similar device architecture and two-point probe [121]. Figure 4.4b shows the averaged results of characterized devices. From the averaged data a clear trend in regards to alkyl chain length is observed with mobility increasing as the SAM alkyl chain length increases and with the reference devices without SAM treatment having the lowest performance. This statement is verified via statistical analysis in which a two-sample two-tailed student's *t*-test comparing the hole/electron mobility to alkyl chain length (binding group held constant) results in a *P* value of less than 0.002 at the 0.05 level. This indicates that the difference in mobility related to SAM alkyl length (8 carbon vs. 18 carbon) is significant. From the similarity in charge mobility of the same SAM alkyl chain length, regardless of binding group used, it becomes apparent that the specific SAM binding group used does not play a significant role in influencing device mobility.

This relationship also verified via statistical analysis in which a two-sample two-tailed student's *t*-test comparing the hole/electron mobility to binding group (alkyl chain length held constant) results in a *P* value greater than 0.05 at the 0.05 level. This indicates that the mobility difference related to SAM binding group is not significant. An exception to this comparison is the hole mobility of OTS and OPA which has a *P* value less than 0.002 at the 0.05 level indicating that the difference in hole mobility for these two SAMs is statistically significant. This may indicate a difference packing density between the two SAMs. In fact, the significant increase in performance between the different alkyl chain lengths indicates that SAM packing density plays a major role in graphene mobility. Since long alkyl chains have been shown to produce near crystalline packing structure [128] compared to their more disordered shorter length counterparts, it can be argued that the performance enhancement comes from the reduction in defects within the SAM itself as well as due to enhanced quenching of hydroxyl groups present at the dielectric surface which results in a reduction of charge trap states. This hypothesis correlates well with the previously discussed difference between long and short chain alkyl groups in regards to V_D.

Additionally, the effect of quenching of hydroxyl groups at the dielectric surface by the SAM is made further apparent by the fact that the electron mobility of untreated devices is significantly lower than those of SAM treated substrates. The hole to electron mobility ratio (H/E) is 2.8 for untreated substrates while the SAM treated devices maintain a consistent ratio of approximately 1.5 across all SAMs tested. This imbalance in H/E ratio for untreated substrates is due to electron susceptibility to hydroxyl groups on the dielectric surface acting as charge trap sites [93]. From these results we can ascertain that the quenching of hydroxyl groups by the SAM binding group enhances graphene charge mobility, but that the specific binding group used does not play a significant role. In order to achieve the highest mobility of CVD graphene transistors it becomes apparent that SAM molecular design should incorporate a functional group that will enhance SAM packing density in order to minimize charge trap states.

4.1.4 *Conclusion*

In conclusion, we have shown that the chosen SAM binding group can make a significant doping contribution to the properties of graphene transistors. In particular, phosphonic acid based SAMs intrinsically n-doped graphene transistors. Additionally, we found that when using alkyl-based molecules a SAM with a greater packing density has a stronger doping effect either due to increased dopant density or a reduction in charge trap states. Conversely, we found that silane based SAM molecules do not significantly dope graphene transistors due to their similarity to the underlying dielectric layer. Furthermore, we have shown no significant difference between specific SAM binding groups used in terms of the extrinsic charge mobility of graphene transistors. Rather, it was found that the packing density and crystallinity of the molecular monolayer plays a key role in enhancing charge mobility once extrinsic factors such as absorbed impurities are removed.

4.2 Systematic Doping Control of CVD Graphene Transistors with Functionalized Aromatic Self-Assembled Monolayers

Recent reports have shown that self-assembled monolayers (SAMs) can induce doping effects in graphene transistors. However, a lack of understanding persists surrounding the quantitative relationship between SAM molecular design and its effects on graphene. In order to facilitate the fabrication of next-generation graphene-based devices it is important to reliably and predictably control the properties of graphene without negatively impacting its intrinsic high performance. In this study, we utilize SAMs with varying dipole magnitudes/directions and directly correlate these values to changes in performance seen in graphene transistors. It is found that by knowing the z-component of the SAM dipole one can reliably predict the shift in graphene charge neutrality point after taking into account the influence of the metal electrodes (which also play a role in doping graphene). We verify this relationship through density functional theory and comprehensive device studies utilizing atomic force microscopy, x-ray photoelectron spectroscopy, Raman spectroscopy, and electrical characterization of graphene transistors. It is shown that properties of graphene transistors can be predictably controlled with SAMs when considering the total doping environment. Additionally, we find that methylthio-terminated SAMs strongly interact with graphene allowing for a cleaner graphene transfer and enhanced charge mobility. A modified version of this section can be found published as a peer-reviewed article in Advanced Functional Materials [50].

4.2.1 *Introduction*

Graphene is a two-dimensional semimetal with promising electrical and optical properties that consists of sp^2-hybridized carbon atoms arranged in a honeycomb lattice. The electronic properties arising from the unique crystal structure of graphene result in a linear dispersion for low energy carriers, which can be described as zero rest-mass relativistic particles with exemplary transport properties [111, 129, 130]. Electron mobility as high as 200,000 $cm^2 V^{-1} s^{-1}$ can be achieved once extrinsic factors such as scattering centers from underlying substrates, adsorbates, and defects within graphene itself are controlled [112, 113, 115, 131-133]. In order to utilize graphene for next generation electronic devices it is necessary to have precise control of carrier concentration and

polarity without disrupting its intrinsic properties. Carrier doping of graphene has so far been achieved via chemical doping [116, 134-136], substitutional doping [117, 137, 138], electric field modulation [139, 140], and metal contact doping [119, 141].

Recent reports have also shown it is possible to modulate the properties of graphene by modifying the underlying dielectric surface with a self-assembled monolayer (SAM) resulting in doping control without compromising the intrinsic graphene performance [49, 120, 121, 142]. However, these studies use exfoliated graphene rather than the more commercially viable CVD-based graphene. In addition, exfoliation severely limits the ability to do a systematic and statistical study based on multiple devices due to the taxing processing steps necessary to fabricate individual devices. In order to circumvent this issue, characterization of these devices is mainly attributed to multiple Raman scans on a few pieces of modified graphene rather than multiple pieces of graphene. While such methodology is useful for obtaining an overall picture of the graphene doping environment it makes it difficult to understand the exact relationship between SAMs and graphene. SAMs are commonly used in organic field-effect transistors to modify the work function of metal electrodes [48, 92], quench charge trap sites at the interface between semiconductor and metal or dielectric [89, 90, 93], and modulate the position of the threshold voltage [51, 143, 144]. SAMs represent an ideal platform for control of graphene electronics as they can be designed and functionalized at the molecular scale to cater to specific device requirements.

However, there is still a need for better understanding of how SAM-treated dielectrics modulate the doping of graphene devices. In particular, an understanding of how the SAM dipole, while taking into account metal electrode effects, influences graphene has yet to be studied. In this section we demonstrate that SAMs can be used to reliably and predictably control the charge carrier concentration of graphene transistors without negatively impacting charge carrier mobility while taking into account the total doping environment.

4.2.2 *Experimental*

4.2.2.1 *Device Fabrication and Testing*

CVD monolayer graphene was grown on copper foil at 990 °C in flowing methane and hydrogen gas at 0.002 and 0.035 slm respectively. Standard poly(methyl methacrylate) (PMMA) was then spin coated on top of graphene as a support layer. The underlying copper foil was then etched away using aqueous ammonium persulfate leaving only graphene supported by PMMA floating in the solution. Graphene/PMMA was then transferred to several different baths of deionized water in order to clean the membrane from etchant and metal impurities.

All SAMs utilized the same assembly process in which heavily p-doped Si/300 nm SiO_2 substrates were cleaned with piranha (30% aqueous hydrogen peroxide and 12 M sulfuric acid in a 1:4 volume ratio) followed by sonication in RCA (ammonium hydroxide, 30% aq. hydrogen peroxide, and deionized water in a 1:1:5 volume ratio), and then extensive rinsing in deionized water. Substrates were then plasma cleaned for 30 minutes resulting in a 2-3 nm layer of AlO_x as described previously [46]. Phosphonic acid compounds for SAMs were dissolved in a mixed solvent of tetrahydrofuron (THF) and ethanol (EtOH) (1:1 vol ratio, 0.1 mM concentration), sonicated until complete dissolution, and then filtered with a 0.2 μm PTFE filter. Cleaned substrates were then immersed in the filtered solution and assembly was allowed to occur at room temperature over the course of 48 hours. Upon the completion of assembly, the formed SAMs on substrates were annealed at 120 °C for 15 minutes followed by cleaning via sonication in dimethylformamide, THF, and EtOH in order to remove any residual aggregates.

PMMA supported graphene was then transferred onto assembled SAM substrates and allowed to dry over the course of 24 hours. Afterwards PMMA on top the graphene/SAM/substrates was removed via rinsing in hot (~60 °C) acetone over several hours followed by an isopropyl alcohol rinse.

Shadow masks were then used to fabricate 40 nm thick Au source and drain electrodes using standard thermal evaporation under high vacuum (10E-7 Torr). Devices were subsequently annealed at 200 °C under nitrogen and characterized immediately using an Agilent 4155B semiconductor parameter analyzer. Reported electrical characteristics are an average of more than 15 devices with channel lengths varying between 12, 20, 30, 50, 80, and 100 μm. No significant

deviation in performance or charge neutrality point was seen with respect to transistor channel length.

4.2.2.2 *AFM, Contact Angle Goniometry, and Raman Spectroscopy*

Digital Instruments Multimode Nanoscope IIIa scanning probe microscope (Veeco Instruments, Plainview, NY) was used in AFM tapping mode. Aqueous static contact angle values were taken with a VCA Optima Surface Analysis System (Adv. Surface Technology Products, Billerica, MA) and are an average of five measurements with a standard deviation of less than ±3°. An inVia Raman Microscope (Renishaw, Cook, IL) with 514 nm laser was used to determine the quality of graphene on dielectric surface via the characteristic phonon peaks of graphene and is averaged data of more than 10 scans sweep from 3000 to 1000 cm^{-1} and a resolution of 2.5 cm^{-1}.

4.2.2.3 *XPS Characterization*

XPS measurements were performed under ultrahigh vacuum (5E-10 Torr) with a PHI VersaProbe X-ray photoelectron spectrometer (ULVAC-PHI, Kanagawa, Japan) using a monochromatic focused Al-K_α X-ray source ($h\nu$ = 1486.70 eV) and hemispherical analyzer. In order to achieve a high resolution spectrum for characterization of the C 1s peak a pass energy of 23.5 eV was used. Work function measurements are an average of approximately 14 positions on a given substrate and characterized with a pass energy of 2.95 eV. The large number of data points were necessary to ensure consistency due to the fact that the samples were exposed to atmosphere before measurement. It is possible that even though exposure was brief (only a few seconds during sample transfer) adsorbed species may partially screen the dipole field resulting in a lower work function shift versus dipole strength while still remaining linear.

4.2.3 *Results and Discussion*

SAMs were grown via immersion assembly on cleaned 300 nm thick SiO_2 with an AlO_x adhesion layer between the SAM and dielectric. Due to the weak interaction between the phosphonic acid SAM binding group and silanol (Si-OH) on the SiO_2 oxide surface, an AlO_x adhesion layer was necessary in order to form a covalent bond between the SAM and dielectric [46]. Functionalized aromatic SAMs of (4-cyanophenyl)phosphonic acid, 4-(trifluoromethyl)phenylphosphonic acid, phenylphosphonic acid, 4-(methylthio)phenyl phosphonic acid, and 4-(methoxy)phenylphosphonic acid were used to systematically study the influence of SAM dipoles on CVD graphene transistors. These SAMs will be referred to throughout this paper as CN, CF_3, Ph, MeS, and MeO respectively and can be seen in Figure 4.5a.

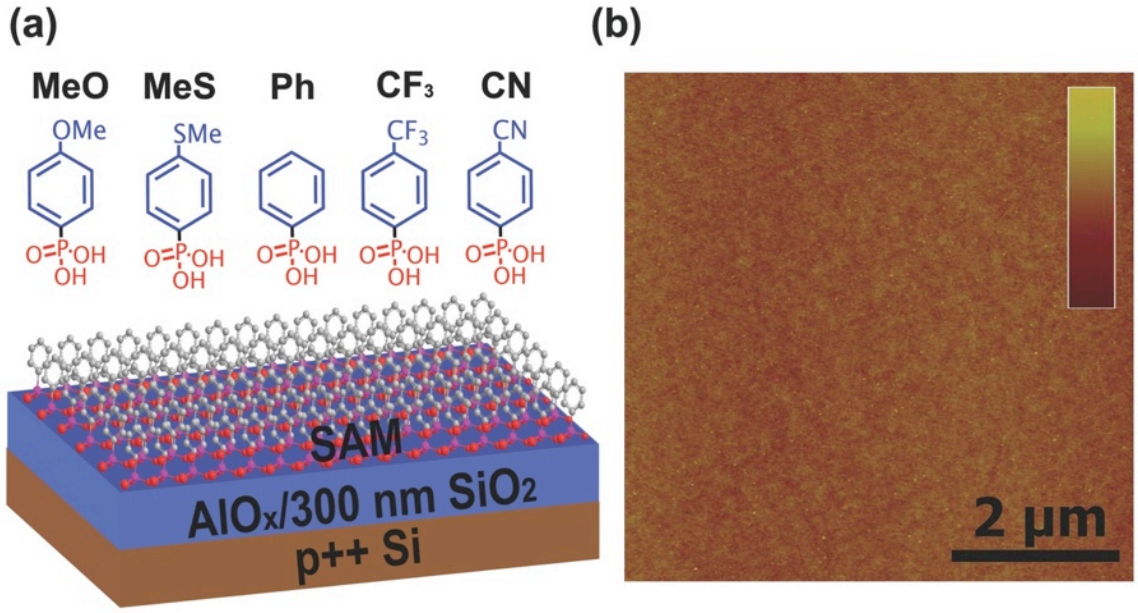

Figure 4.5. Chemical structure of SAMs and representative AFM morphology. (a) Chemical structure of each SAM used in this study with assembled SAM schematic and (b) representative topology measured by AFM of assembled SAM on AlO_x/SiO_2 dielectric. The color z-scale for the AFM image shown in the top right is 0-5 nm. Reprinted with permission from [50]. Copyright 2014, Wiley-VCH Verlag GmbH & Co. KGaA.

4.2.4 *AFM and Contact Angle Goniometry of SAMs*

Phosphonic acid molecules were used to functionalize the AlO_x/SiO_2 dielectric layer due to advantages over traditional silane based SAMs such as: high thermal stability [97], binding not limited by surface hydroxyl content [23], and no homocondensation [34]. These factors, in conjunction with the chosen molecular designs, result in the formation of densely packed SAMs with high thermal stability and similar packing density. Atomic force microscopy (AFM) and water contact angle goniometry were used to characterize each SAM assembled on AlO_x/SiO_2 surface. All SAMs show a similar smooth morphology with an RMS roughness between 0.2 and 0.3 nm, which is comparable to the untreated dielectric surface. A representative image of the SAM topography can be seen in Figure 4.5b.

The static water contact angle for each SAM on the AlO_x dielectric was determined to be 57°, 75°, 61°, 68°, and 64° for CN, CF_3, Ph, MeS, and MeO, respectively. For reference, the water contact angle for the untreated dielectric surface is less than 10°. The standard deviation of contact angle for each SAM is less than 3°, indicating uniform and continuous coverage across the entire dielectric surface. The low RMS roughness and preserved contact angle after extensive sonication in organic solvents post-assembly, indicates the formation of a dense and homogenous molecular monolayer that is chemically bound to the dielectric surface and free of physisorbed aggregate.

4.2.4.1 *SAM Dipole Determination via Density Functional Theory*

Density Functional Theory (DFT) calculations were used to extract the molecular dipole of the SAMs [145] from geometry-optimized structures of single molecules. DFT [146, 147] geometry optimizations were performed using Gaussian 09(A.02) [148] employing the Perdew, Burke, and Ernzhof [149] functional (PBE) with the split valence basis set (SVP) from Schaefer, Horn, and Ahlrichs [150] and the SVPFit auxiliary basis [151]. Molecules were rotated into frame so to define the longest molecular axis as the z direction; that is, the vector from the phosphorous to the para-standing carbon of the phenyl SAMs. Frequency calculations and population analysis were performed on the optimized geometries and minima were verified through normal mode analyses. Finally, conformational analysis was performed on all molecules to determine the lowest

energy conformations. A summarization of calculated dipoles along the z-axis can be found in Table 4.1.

Table 4.1. Summarized data from this study contained dipole moment, contact angle, work function shift, charge neutrality point, and mobility. Data from the z-component of the SAM dipole moment (μ_z), static water contact angle (SCA), the change in graphene/SAM/dielectric stack work function relative to the reference graphene/dielectric device ($\Delta\Phi_{Gr}$/SAM), the mean Dirac voltage (V_{Dirac}), electron mobility (μ_e), and hole mobility (μ_h) for graphene/SAM transistors with Au source and drain electrodes.

SAM	μ_z [D]	SCA [deg]	$\Delta\Phi_{Gr}$/SAM [eV]	V_{Dirac} [V]	μ_e [$cm^2V^{-1}s^{-1}$]	μ_h [$cm^2V^{-1}s^{-1}$]
Ref[a]	n/a[b]	<10	n/a[b]	-7.33 ± 0.78	802 ± 189	1611 ± 376
MeO	-2.02	63.9	-0.12 ± 0.02	-10.88 ± 1.48	856 ± 257	1115 ± 318
MeS	-1.49	68.1	0.03 ± 0.01	-5.76 ± 0.86	1327 ± 294	2053 ± 317
Ph	-0.74	60.5	-0.07 ± 0.01	-8.70 ± 2.73	665 ± 285	1164 ± 485
CF_3	1.92	75.3	0.19 ± 0.03	12.32 ± 3.91	774 ± 140	1441 ± 271
CN	3.88	57.3	0.29 ± 0.02	15.91 ± 3.85	693 ± 181	1225 ± 267

[a] Ref represents device with no SAM treatment on dielectric surface, graphene only; [b] not applicable

4.2.4.2 *Raman Spectroscopy for Determination of Graphene Quality*

A Renishaw inVia Raman Microscope with 514 nm laser was used to determine the quality of graphene on SAM modified dielectric surface via the characteristic phonon peaks of graphene. Figure 4.6 shows a representative Raman spectrum of graphene on the SAM/dielectric. The lack of a D peak (~1350 cm^{-1}) implies high quality, defect free graphene [124]. The 2D peak (~2685 cm^{-1}) is spectrally sharp and its intensity is about four times greater than that of the G peak (~1585 cm^{-1}), which are characteristics of monolayer graphene [125, 152, 153].

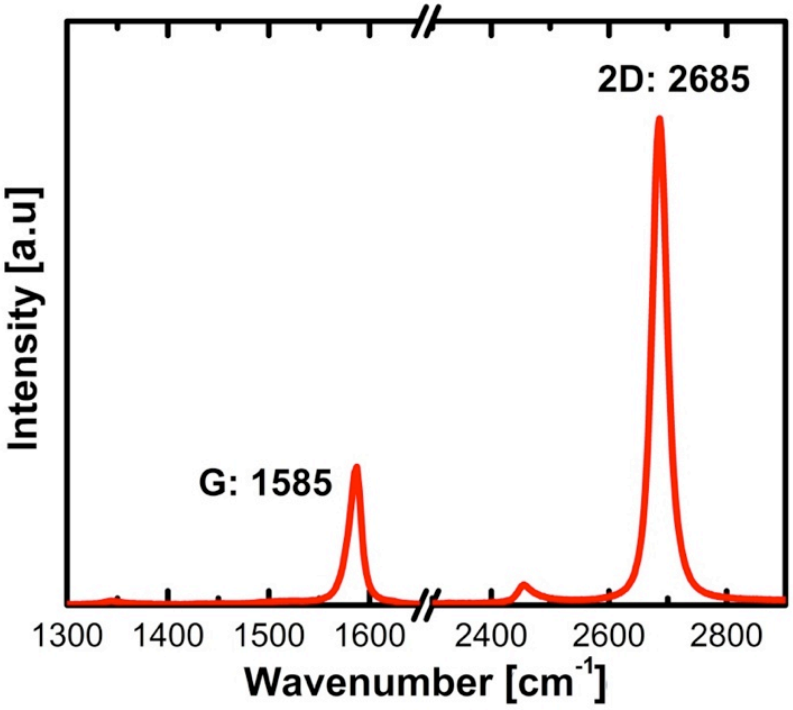

Figure 4.6. Raman spectra of graphene on SAM signifying high quality graphene. Reprinted with permission from [50]. Copyright 2014, Wiley-VCH Verlag GmbH & Co. KGaA.

4.2.4.3 *XPS Characterization*

To obtain a better understanding of the effect a given SAM-dipole has on the electronic properties of graphene, X-ray photoelectron spectroscopy (XPS) was used to determine the work function as well as the characteristic C1s binding energy peak of graphene on the various SAM-treated AlO_x/SiO_2 surfaces. In order to minimize the influence of extrinsic factors such as atmospheric adsorbants, substrates were annealed under an inert atmosphere of N_2 at 200 °C for 2 hours and were only exposed to ambient conditions for a few seconds while transferring into the XPS system. A -5 V bias was applied to the graphene/SAM substrate relative to the spectrometer, and the location of the secondary electron cut-off energy was determined at a take-off angle of 90° via linear extrapolation with respect to the background baseline as described elsewhere [154]. Graphene on an AlO_x/SiO_2 dielectric without SAM treatment was determined to have a work function of 4.31 ± 0.02 eV which is comparable to that in literature for CVD grown graphene [155]. The relative work function shift of graphene on SAM-treated dielectric surfaces was within a range of 0.5 eV dependent on the SAM dipole direction and magnitude. A linear relationship, with the exception of MeS, between the SAM dipole and the average shift in graphene work function is shown in Figure 4.7a.

The surface dipole generated by the SAM is expected to affect the work function of graphene based on the following relationship [156, 157]:

$$\Delta\Phi_{SAM} = \left(\frac{eN\mu_z}{\varepsilon_0 \varepsilon_{SAM}}\right) \qquad (Eq.\ 4.2)$$

Where e is elementary charge, N is the SAM packing density, μ_z is the SAM dipole component perpendicular to the dielectric plane, ε_0 is the permittivity of free space, and ε_{SAM} is the relative permittivity of the SAM. From equation 4.2, a linear relationship between the change in work function of the graphene/SAM stack and the SAM dipole moment is expected provided that the relative dielectric constant and packing density for each SAM is similar. This is a reasonable expectation given the similarity between each SAM molecule. Assuming a relative dielectric constant of 2.5, the packing density of each SAM is calculated to be approximately 5E13 molecules per square centimeter, which is near the expected theoretical value [158].

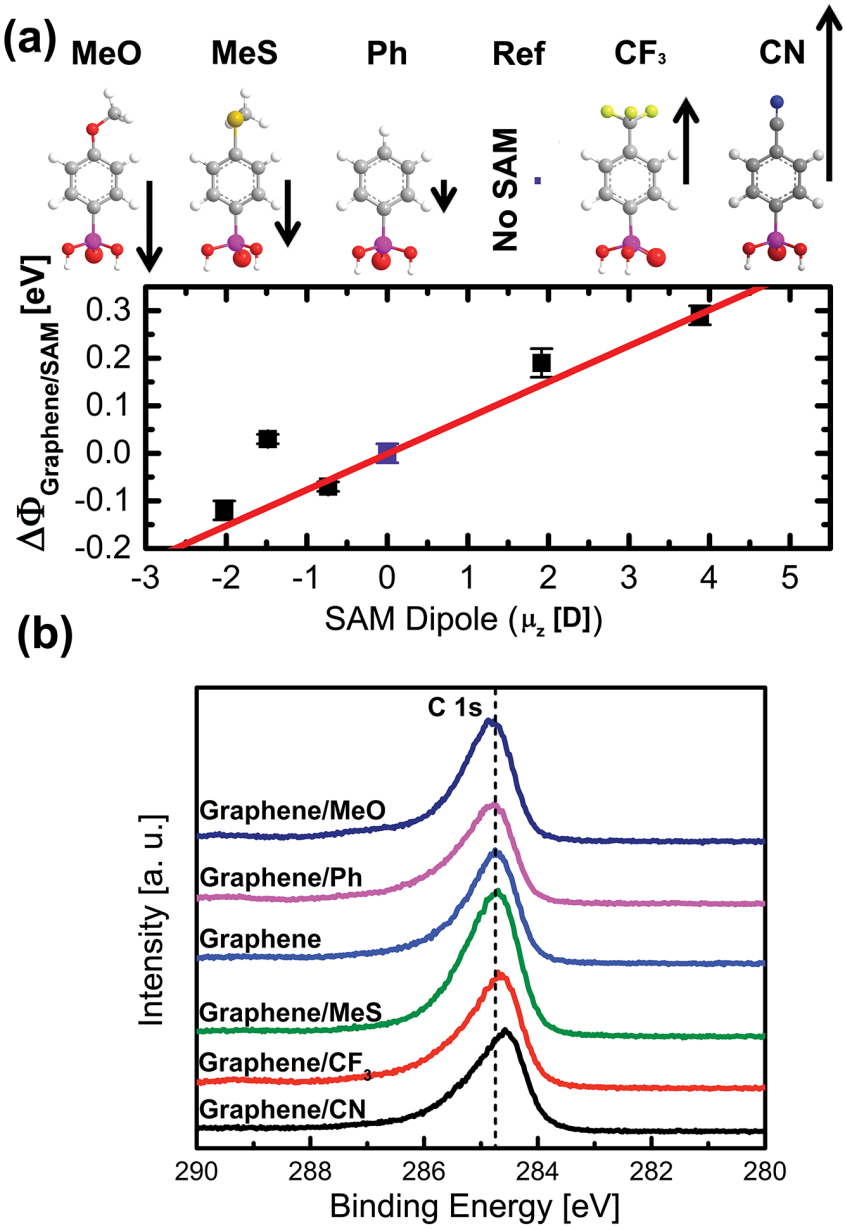

Figure 4.7. Influence of SAM dipole on graphene work function and shift in C 1s binding peak from XPS. (a) Visual representation of predicted z-component of SAM dipole (μ_z). Change in graphene/SAM work function as measured by XPS with respect to μ_z. The outlier of the linear fit is the MeS SAM which displays a strong interaction with graphene. (b) C 1s binding energy peak for various graphene/SAMs used in this study. Direct correlation between peak position and SAM dipole is observed. Reprinted with permission from [50]. Copyright 2014, Wiley-VCH Verlag GmbH & Co. KGaA.

It should be noted that the reference device with no SAM of graphene/dielectric was given a dipole magnitude of 0 D due to the additive nature of dipoles along the same direction [159]. Since the same base dielectric system is used across all characterized systems it is reasonable to assume that effect of the bare dielectric surface is uniform. An exception to the linear relationship between SAM dipole component and change in work function is the MeS SAM. It is hypothesized that the strong interaction between π-conjugated carbon and sulfur [160-162] results in a stronger interaction between the SAM and graphene upon device annealing. In addition, annealing may cause the MeS SAM to locally react with vacancy or edge defects within the graphene film which has been shown to induce hole doping [163]. Representative carbon 1s binding energy peaks can be seen in Figure 4.7b that show a shift towards lower binding energy (blue shift) as the p-type SAM character increases and higher binding energy (red shift) as the n-type SAM character increases which is in agreement with reported results [49]. These results also fall in line with the measured shift in work function, including MeS, which shows slight p-type character.

4.2.4.4 *Electrical Characterization of SAM Modified Graphene Transistors*

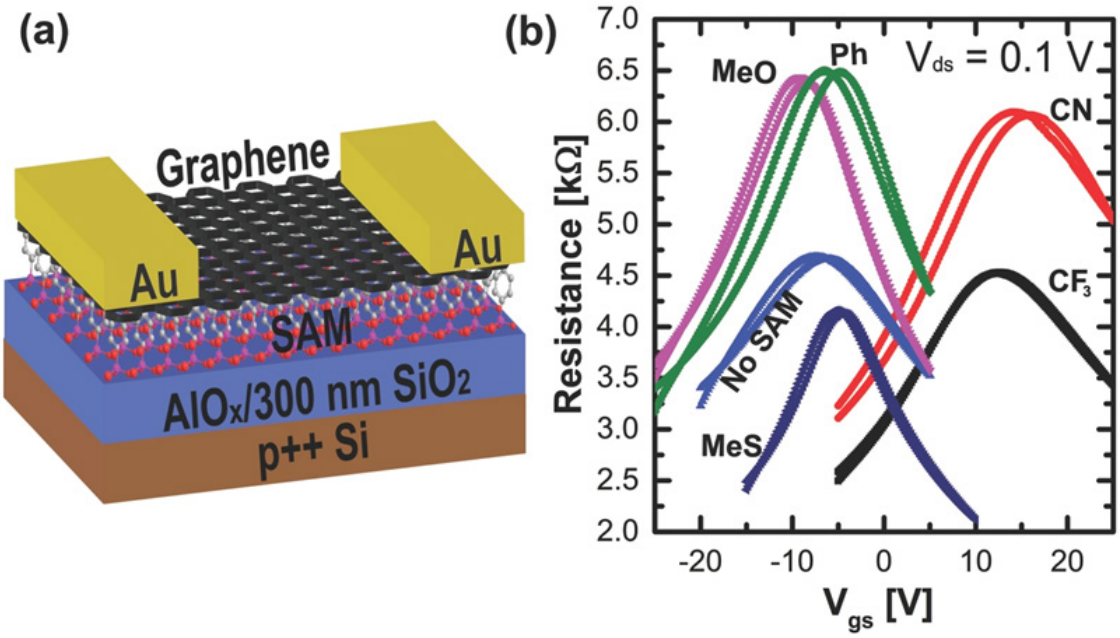

Figure 4.8. Graphene transistor schematic and transfer curve (a) Schematic of graphene transistors fabricated and used in this study. (b) Representative transfer curves (forward and backward sweep) of graphene transistors with various SAM-treated substrates. Reprinted with permission from [50]. Copyright 2014, Wiley-VCH Verlag GmbH & Co. KGaA.

In order to further understand the effect of SAM dipoles on graphene, graphene transistors on SAM-modified AlO_x/300 nm SiO_2 were fabricated. Transistor channel width was 1000 µm while channel length varied between 12 µm and 100 µm. A schematic of the device structure and typical transfer curves of the graphene devices are shown in Figures 4.8a and 4.8b. The low hysteresis in these devices indicates an insignificant amount of adsorbed water and oxygen molecules that have recently been shown to be the origin of hysteresis in graphene via a redox reaction [126]. The average total resistance at the charge neutrality point is 5.5 kΩ, 4.4 kΩ, 6.6 kΩ, 4.3 kΩ, 6.6 kΩ and 4.8 kΩ for CN, CF_3, Ph, MeS, MeO and the Ref device with no SAM treatment respectively. This slight variation in resistance may be due to several factors such as differences in contact or sheet resistance from each individual SAM because of differing doping levels, charge impurities, or scattering sites. Several factors could affect contact resistance such as the thickness of the SAM molecule and its particular dipole. Secondly, the SAMs are shown previously in this section to

influence the work function of graphene which may further influence contact resistance. The extrinsic field-effect mobility of graphene was extracted from the maximum slope near the charge neutrality point with the following equation:

$$\mu_{FET} = \frac{L_{ch}(dI_{ds}/dV_{gs})}{W_{ch}C_{ox}V_{DS}} \qquad \text{(Eq. 4.3)}$$

where L_{ch} and W_{ch} is the channel length and width respectively, C_{ox} is the gate-oxide capacitance per area, and V_{DS} is the constant drain-source voltage [127].

Averaged field-effect mobility can be seen in Table 4.2. Mobility values do not deviate significantly throughout all measured channel lengths. Although most of the graphene devices on SAM-treated dielectrics exhibited slightly lower mobility than the reference device without SAM treatment (hole mobility of 1200 $cm^2V^{-1}s^{-1}$ and 1600 $cm^2V^{-1}s^{-1}$, respectively), the MeS SAM treated devices surprisingly exhibit significantly enhanced hole and electron mobility with values of 2053 $cm^2V^{-1}s^{-1}$ and 1327 $cm^2V^{-1}s^{-1}$, respectively. This enhancement may be due to the strong π-conjugated carbon and sulfur interaction between the SAM and graphene (as seen in XPS results) which results in the transfer of graphene with less wrinkles and tears. Additionally, a general correlation between the total resistance and the extrinsic hole mobility is observed for SAM-treated devices with the lowest resistance having the highest mobility. This same correlation is not seen for electron mobility most likely due to the sensitivity of electrons to charge traps. This enhancement of mobility may indicate a reduction in contact resistance and remains an area to be further studied. Subsequently, thio-functionalized SAMs may prove to be a potential avenue to obtain high performance graphene transistors.

4.2.4.5 *Correlation between Charge Neutrality Point, Metal Electrode, and SAM*

The charge neutrality point (V_D) is defined as the conductivity minimum of the transfer curve [164]. V_D for each tested device was determined and averaged data were interrelated to the calculated SAM dipoles in Figure 4.8b. These data follow a general trend in which the SAM direction and magnitude is a baseline predictor for V_D. Based on the understanding of the electronic structure of graphene, it is possible to correlate the V_D shift to the change in Fermi energy as

measured by XPS and discussed previously. Due to the linear band structure of graphene, the shift in Fermi energy induced by the SAM dipole can be described as follows:

$$\Delta E = \hbar v_F \sqrt{\pi n (V_{D2} - V_{D1})} \qquad \text{(Eq. 4.4)}$$

where n is the intrinsic carrier density per volt [165] with a typical value of approximately 7.2E10 cm^{-2} V^{-1}, v_F is the Fermi velocity [166] previously reported as 1.1E6 m s^{-1}, and V_{D2} (V_{D1}) is the charge neutrality point of devices with (without) SAM treatment. Appropriately, it is expected that ΔE induced by the SAM should follow a linear relationship with the change in work function of the graphene/SAM devices previously measured via XPS. A linear fit is seen in Figure 4.9a with the exception for CN SAM.

In order to explain the similarity of V_D and thus ΔE for CF_3 and CN SAM treated dielectrics, we attribute this difference as the influence of doping from the metal electrodes. Previously, the results from DFT calculations have illustrated the doping of graphene on Cu with various metal contacts [167, 168]. It was found that physisorbed metals such as Pt, Au, Cu, Ag, and Al can dope graphene to generate holes or electrons depending on the difference between the work function of metal and graphene, and the energy offset related to the separation distance between the metal and graphene. For example, if the separation distance between graphene and the metal is large (5 Å) the crossover from n-type to p-type doping occurs when the metal work function is equal to the work function of graphene. However, the equilibrium spacing for gold is expected to be 3.3 Å which results in a crossover from n-type to p-type doping when the metal is approximately 0.9 eV lower than that of graphene. It is thus predicted that CN and CF_3 SAMs cause the work function of graphene to become close enough to gold that the metal electrode changes from being a p-dopant to that of an n-dopant. This explains why V_D for CN is near that of CF_3 since increasing n-doping from the gold electrodes will result in a negative shift of charge neutrality point. The total change in ΔE is then related to the following equation:

$$\Delta E \approx \Delta\Phi_{\frac{graphene}{SAM}} + \Delta\Phi_{\frac{electrode}{SAM}} \qquad \text{(Eq. 4.5)}$$

It should be noted that the induced doping from metal electrode, $\Delta\Phi_{electrode/SAM}$, should take into account the influence of the SAMs under graphene since the device structure employs an

electrode stack of Au/graphene/SAM as seen previously in Figure 4.8. It is then possible to compare the experimentally determined value $\Delta\Phi_{electrode/SAM}$ with the expected theoretical value shown in Figure 4.9b. The Fermi level shift equation from [167] was used to determine the influence of Au metal doping on graphene:

$$\Delta\Phi_{Electrode}(d) = \pm \frac{\sqrt{1 + 2\alpha D_0(d - d_0)|W_M - W_G - \Delta_c(d)|} - 1}{\alpha D_0(d - d_0)} \qquad (Eq. 4.6)$$

$$and\ \Delta_c(d) = e^{-\gamma d}(a_0 + a_1 d + a_2 d^2) \qquad (Eq. 4.7)$$

where the parameter d represents the separation distance between the metal electrode and graphene with an equilibrium value determined to be 3.3 Å. The work function of Au (W_M) was set as 5.25 eV, while W_G represented the measured value of the graphene/SAM work function. Other parameters are standard parameters related to the graphene unit cell and are detailed further in reference [167].

While a slight deviation of measured and theoretical data occurs, a correction factor can be applied to compensate for this discrepancy, which may be related to the interaction of the SAM dipole on the work function of the gold metal. In order to compensate for interaction/shielding effect between the underlying SAMs on graphene and the metal electrode work function, it was assumed that the effective dipole was reduced and a correction factor was applied. For this factor, W_G from the equation above was changed to $W_{G0} + b*\Delta\Phi_{SAM}$. Where $\Delta\Phi_{SAM}$ is the deviation from the untreated work function of graphene caused by the SAM and b is the correction factor equal to 0.679. W_{G0} is the untreated work function of graphene measured to be 4.31 eV.

The original theoretical predictions assume that graphene on Cu has little to no influence on the properties of graphene. However, in this particular work, there is significant influence of the underlying SAM on the properties of graphene and it is reasonable to expect that due to the ultrathin nature of graphene, the dipole of the SAM should have some contribution to the work function of the metal electrode less some screening effect due to graphene. Figure 4.9c shows an overall schematic of the influences of various interfaces on the properties of a graphene transistor with a SAM modified dielectric. It is important to consider all interfacial effects in order to reliably predict and control the properties of graphene transistors.

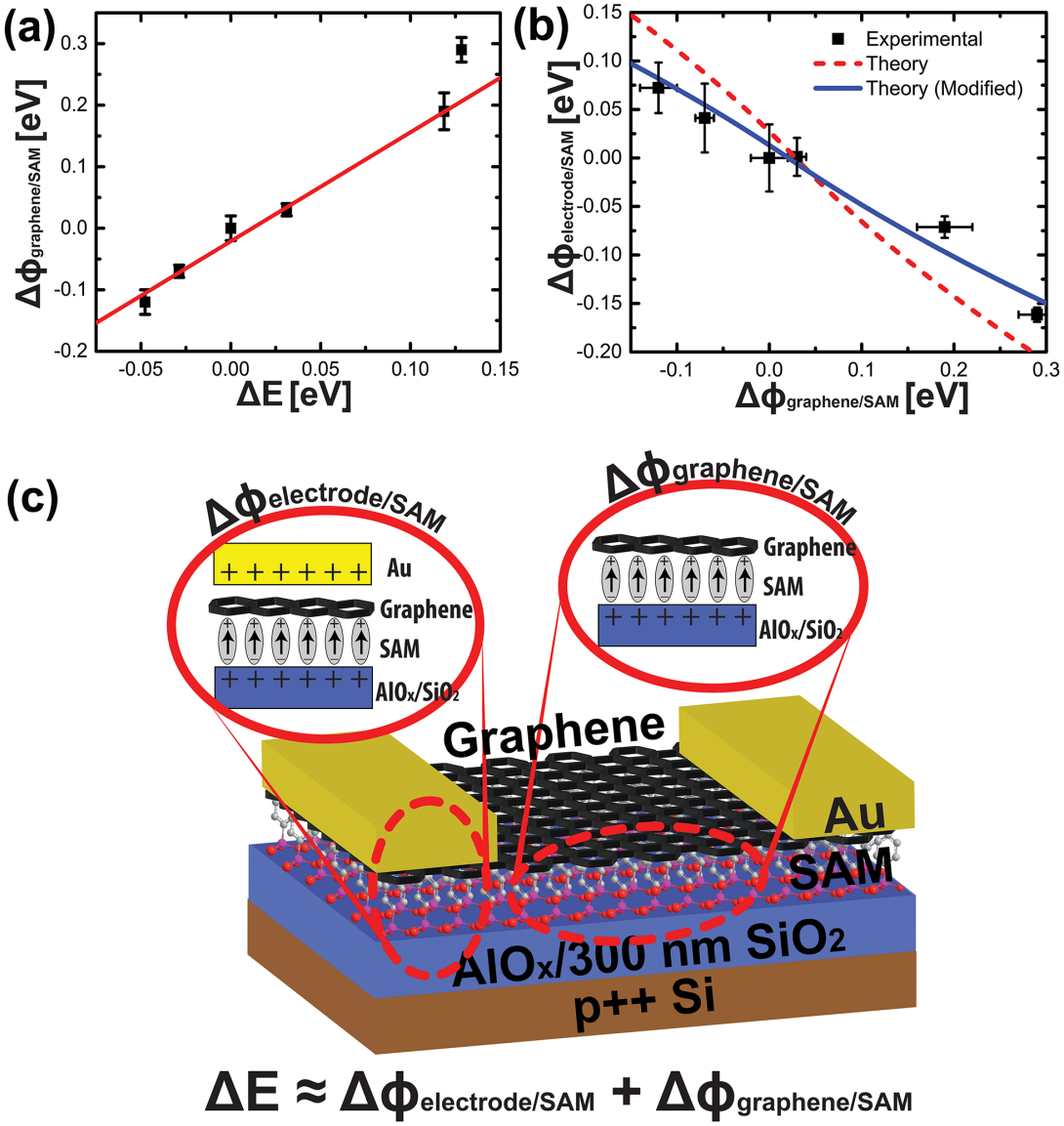

Figure 4.9. Schematic showing the total influence of SAM and metal electrode on graphene transistors. (a) Shift in graphene/SAM work function (measured via XPS) with respect to the total energy shift (determined from FET charge neutrality position) and (b) experimental, theoretical, and modified theoretical results comparing the influence of the contributions of each interface on the total energy shift. (c) Schematic showing that both the electrode/graphene/SAM/dielectric interface and the graphene/SAM/dielectric interface must both be taken into account in order to predict the total shift in energy. Reprinted with permission from [50]. Copyright 2014, Wiley-VCH Verlag GmbH & Co. KGaA.

4.2.5 *Conclusion*

In summary, a clear relationship between SAM molecular dipole and graphene device performance was found to help predict the properties of graphene-based transistors. This is crucial for future applications and may enable predictable and controlled band-gap opening of bilayer graphene without the need for a dual gate architecture via self-assembled monolayers [169, 170]. We have presented direct experimental evidence that shows systematic and precise control of the charge neutrality point of graphene/SAM transistors is possible by carefully tuning the SAM and metal contact without having a negative impact on device performance.

Chapter 5. ENHANCED PERFORMANCE OF SELF-ASSEMBLED MONOLAYER FIELD-EFFECT TRANSISTORS WITH TOP-CONTACT GEOMETRY THROUGH MOLECULAR TAILORING, HEATED ASSEMBLY AND THERMAL ANNEALING

Low voltage self-assembled monolayer field-effect transistors (SAMFETs) that operate under an applied bias of less than -3 V and a high hole-mobility of 10^{-2} cm^2 V^{-1} s^{-1} are reported. A self-assembled monolayer (SAM) with a quaterthiophene semiconducting core and a phosphonic acid binding group is used to fabricate SAMFETs on both high-voltage (AlO_x/300 nm SiO_2) and low-voltage (HfO_2) dielectric platforms. High performance is achieved through the enhanced SAM packing density via a heated assembly process and through the improved electrical contact between SAM semiconductor and metal electrodes. Enhanced electrical contact is obtained by utilizing a functional methyl-thio head group combined with thermal annealing post gold source/drain electrode deposition to facilitate the interaction between SAM and electrode. A modified version of this section can be found published as a peer-reviewed article in Advanced Functional Materials [57].

5.1 INTRODUCTION

Self-assembled monolayers (SAMs) are now an ubiquitous tool for interface modifications [171] to control and modulate a variety of devices such as hybrid and organic photovoltaics [172-176], light-emitting diodes [177-180], and organic transistors [128, 145, 181-183]. Recent progress has also expanded the role of SAMs from a passive interfacial modifier to potentially serve as an active device layer to replace traditional dielectrics and semiconductors in organic field-effect transistors (OFETs). For example, the development of hybrid dielectrics, which are comprised of an ultra thin high-k metal oxide layer in conjunction with a SAM, enables low-voltage high-performance operation of organic transistors [44, 46, 184].

Self-assembled monolayer field-effect transistors (SAMFETs) are a promising concept that uses rationally designed π-conjugated SAMs as the semiconductor of a transistor [56, 61, 63, 64, 185]. This concept works in principle because charge transport in an organic semiconductor based FET occurs in the first few monolayers closest to the dielectric [54, 55]. SAMFETs are believed to have a broad appeal for organic semiconductor device applications due to their low-cost processing, reduced material quantity needed compared to tradition organic thin film transistors and ability to be used toward flexible electronics and sensing applications. Significant progress has been made through molecular design and novel device architecture to achieve a state-of-the-art hole mobility of around 10^{-2} cm2 V^{-1} s^{-1}.

In order to achieve further performance enhancement, it is critical to overcome a fundamental challenge of efficient contact between the metal source/drain electrodes and SAM semiconductor in SAMFET devices. Efficient contacts between SAM semiconductor and electrodes may have been enabled by Smits et al. through under-etching the electrodes allowing the SAM to form underneath or, as shown by Schmaltz et al., through utilizing a secondary SAM to elevate the electrodes to allow edge-on contact with the SAM semiconductor core [56, 63]. However, these reports utilize cumbersome and complicated device architectures that may make SAMFETs less appealing towards commercialization. Furthermore, few work has been done to examine the impact of SAM processing on molecular packing density.

Herein we demonstrate top-contact bottom-gate low voltage p-type SAMFETs with a hybrid HfO_2 dielectric that operates under a bias of -3 V and has a charge carrier mobility of 10^{-2} cm^2 V^{-1} s^{-1}. Charge carrier mobility of the SAMFET is increased by over two orders of magnitude through

the designed functional SAM terminal group that enables efficient charge injection between metal electrode and SAM semiconductor in conjunction with optimized processing conditions to enhance SAM packing density.

5.2 EXPERIMENTAL

5.2.1 *Synthesis of SAM Molecules*

Synthesis of SAM molecules was completed by Professor Hong Ma. All chemicals were purchased from Aldrich or TCI America, and used as received unless otherwise specified. Tetrahydrofuran (THF) was distilled under nitrogen from sodium with benzophenone as the indicator. Methylene chloride was distilled over P_2O_5. ^1H NMR spectra (300 MHz) were taken on a Bruker-300 FT NMR spectrometer with tetramethylsilane (TMS) as internal reference. Elemental analysis was determined at QTI (Whitehouse, NJ). ESI-MS spectra were obtained on a Bruker Daltonics Esquire Ion Trap Mass Spectrometer.

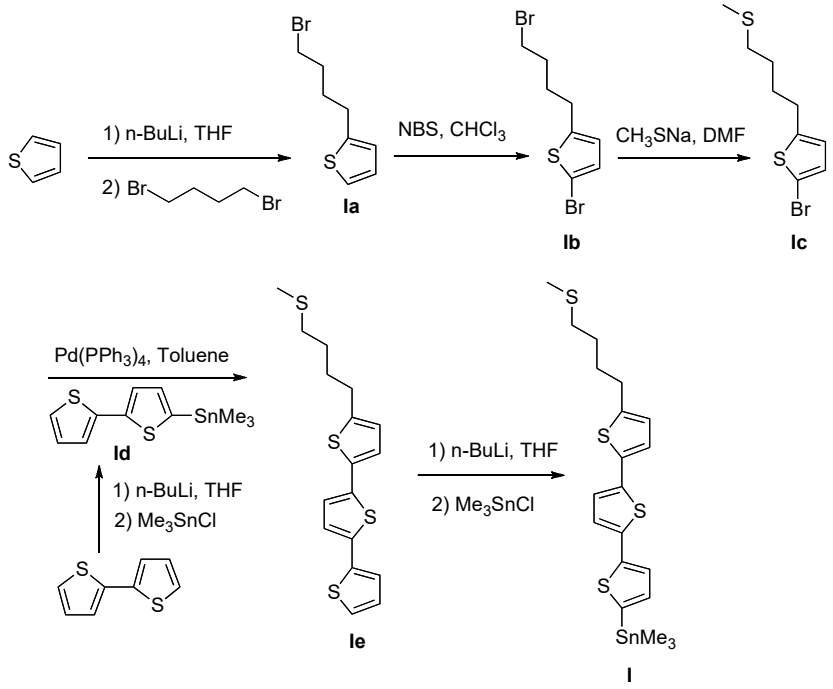

Figure 5.1. Synthesis of 2-(4-methylthiobutyl)terthiophenyltrimethyltin. Reprinted with permission from [57]. Copyright 2015, Wiley-VCH Verlag GmbH & Co. KGaA.

2-(4-Bromobutyl)thiophene (Ia): To a solution of thiophene (5.05 g, 60.0 mmol) in dry THF (40 mL) under nitrogen, a solution of n-butyl lithium in hexanes (2.5 M, 24.0 mL, 60.0 mmol) was dropwise added at –78 °C. The suspension was stirred for one hour at –78 °C. 1,4-Dibromobutane (12.96 g, 7.1 mL, 60.0 mmol) was dropwise added. The reaction mixture was slowly warmed up to room temperature and stirred overnight. The mixture was quenched with water and extracted with ether. The organic layer was washed with water, collected and dried over $MgSO_4$. After removal of the solvent by rotary evaporation under reduced pressure, the crude product was purified over silica gel column chromatography with hexane to hexane/methylene chloride (1:1) as the eluents to afford a colorless liquid (11.02 g, 84%). ^{1}H NMR (300 MHz, $CDCl_3$): δ 7.12 (dd, 1H, J = 5.1, 1.2 Hz), 6.92 (dd, 1H, J = 5.1, 3.3 Hz), 6.79 (dd, 1H, J = 3.3, 1.2 Hz), 3.43 (t, 2H, J = 6.6 Hz), 2.87 (t, 2H, J = 6.6 Hz), 1.76-2.04 (m, 4H). $C_8H_{11}BrS$: Calcd C 43.85, H 5.06, Br 36.46; Found C 43.97, H 4.99, Br 36.53. ESI-MS (*m/z*): Calcd. 218.0; Found 217.9.

2-Bromo-5-(4-bromobutyl)thiophene (Ib): To a solution of Ia (4.38 g, 20.0 mmol) in chloroform (50 mL) in darkness under nitrogen at room temperature was portionwise added N-bromosuccimide (NBS, 3.74 g, 21.0 mmol). The reaction mixture was stirred overnight at room temperature, quenched with water and extracted with methylene chloride. The organic layer was washed with water, collected and dried over $MgSO_4$. After removal of the solvent by rotary evaporation under reduced pressure, the crude product was purified over silica gel column chromatography with hexane as the eluent to afford a colorless liquid (3.02 g, 51%). ^{1}H NMR (300 MHz, $CDCl_3$): δ 6.85 (d, 1H, J = 3.6 Hz), 6.55 (d, 1H, J = 3.6 Hz), 3.44 (t, 2H, J = 6.6 Hz), 2.79 (t, 2H, J = 6.9 Hz), 1.79-2.05 (m, 4H). C8H10Br2S: Calcd C 32.24, H 3.38, Br 53.62; Found C 32.38, H 3.29, Br 53.74. ESI-MS (*m/z*): Calcd. 295.9; Found 295.9.

2-Bromo-5-(4-methylthiobutyl)thiophene (Ic): To a solution of Ib (2.99 g, 10.0 mmol) in anhydrous N,N-dimethylformamide (DMF, 20 mL) under nitrogen at room temperature was added sodium thiomethoxide (1.05 g, 15.0 mmol). The reaction mixture was stirred overnight at 90 °C, cooled down to room temperature and filtered to remove insoluble salts. The filtrate was concentrated by rotary evaporation under reduced pressure. The crude product was purified over silica gel column chromatography with hexane to hexane/methylene chloride (5:1) as the eluents to afford a colorless liquid (1.77 g, 67%). ^{1}H NMR (300 MHz, $CDCl_3$): δ 6.84 (d, 1H, J = 3.6 Hz), 6.54 (d, 1H, J = 3.6 Hz), 2.77 (t, 2H, J = 7.2 Hz), 2.51 (t, 2H, J = 7.2 Hz), 2.09 (s, 3H), 1.57-1.75

(m, 4H). $C_9H_{13}BrS_2$: Calcd C 40.76, H 4.94, Br 30.13; Found C 40.92, H 4.86, Br 30.22. ESI-MS (*m/z*): Calcd. 264.0; Found 264.1.

Bithiophenyltrimethyltin (Id): To a solution of bithiophene (3.33 g, 20.0 mmol) in dry THF (35 mL) under nitrogen, a solution of n-butyl lithium in hexanes (2.5 M, 8.0 mL, 20.0 mmol) was dropwise added at –78 °C. The suspension was stirred for 0.5 hour at –78 °C, warmed up to room temperature and stirred for 0.5 hour, and then cooled down to –78 °C. A solution of trimethyltin chloride (4.38 g, 22.0 mmol) in dry THF (5 mL) was dropwise added. The reaction mixture was slowly warmed up to room temperature, stirred overnight, and quenched with water. The THF solvent was removed from the mixture by rotary evaporation under reduced pressure followed by extracting with methylene chloride. The organic layer was washed with water, collected and dried over $MgSO_4$. After removal of the solvent by rotary evaporation under reduced pressure, the crude product was purified over neutral aluminum oxide column chromatography with hexane as the eluent to afford a colorless liquid (6.39 g, 97%). ^{1}H NMR (300 MHz, $CDCl_3$): δ 7.21-7.29 (m, 1H), 7.15-7.20 (m, 2H), 7.09 (d, 1H, J = 1.8 Hz), 6.99-7.08 (m, 1H), 0.38 (s, 9H). $C_{11}H_{14}S_2Sn$: Calcd C 40.15, H 4.29, S 19.49; Found C 40.27, H 4.14, S 19.58. ESI-MS (*m/z*): Calcd. 330.0; Found 329.9.

2-(4-methylthiobutyl)terthiophene (Ie): To a mixture of Ic (1.02 g, 3.85 mmol) and Id (1.52 g, 4.62 mmol) in anhydrous toluene (20 mL) under nitrogen was added tetrakis[triphenylphosphine]palladium(0) ($Pd(PPh_3)_4$, 89.0 mg, 0.077 mmol) at room temperature. The reaction mixture was stirred overnight at 90 °C, cooled down to room temperature and quenched with water. The toluene solvent was removed from the mixture by rotary evaporation under reduced pressure followed by extracting with methylene chloride. The organic layer was washed with water, collected and dried over $MgSO_4$. After removal of the solvent by rotary evaporation under reduced pressure, the crude product was purified over silica gel column chromatography with hexane/methylene chloride (5:1 to 1:1) as the eluents to afford an orange solid (0.57 g, 42%). ^{1}H NMR (300 MHz, CDCl3): δ 7.20 (dd, 1H, J = 5.1, 1.2 Hz), 7.15 (dd, 1H, J = 3.6, 1.2 Hz), 7.05 (d, 1H, J = 3.9 Hz), 6.97-7.03 (m, 3H), 6.69 (d, 1H, J = 3.6 Hz), 2.83 (t, 2H, J = 6.9 Hz), 2.53 (t, 2H, J = 7.2 Hz), 2.09 (s, 3H), 1.66-1.80 (m, 4H). $C_{17}H_{18}S_4$: Calcd C 58.24, H 5.18; Found C 58.37, H 5.03. ESI-MS (*m/z*): Calcd. 350.0; Found 350.0.

2-(4-methylthiobutyl)terthiophenyltrimethyltin (I): To a solution of Ie (0.526 g, 1.5 mmol) in dry THF (20 mL) under nitrogen, a solution of n-butyl lithium in hexanes (2.5 M, 0.6 mL, 1.5

mmol) was dropwise added at –78 °C. The suspension was warmed up to 0 °C and stirred for one hour, and then cooled down to –78 °C. A solution of trimethyltin chloride (0.329 g, 1.65 mmol) in dry THF (3 mL) was dropwise added. The reaction mixture was slowly warmed up to room temperature, stirred overnight, and quenched with water. The THF solvent was removed from the mixture by rotary evaporation under reduced pressure followed by extracting with methylene chloride. The organic layer was washed with water, collected and dried over $MgSO_4$. After removal of the solvent by rotary evaporation under reduced pressure, the crude product was purified over neutral aluminum oxide column chromatography with hexane/methylene chloride (5:1 to 1:1) as the eluents to afford an orange solid (0.375 g, 49%). ^{1}H NMR (300 MHz, $CDCl_3$): δ 7.08 (d, 1H, J = 3.6 Hz), 7.04 (d, 1H, J = 3.6 Hz), 6.96-6.99 (m, 3H), 6.69 (d, 1H, J = 2.7 Hz), 2.83 (t, 2H, J = 6.9 Hz), 2.53 (t, 2H, J = 6.9 Hz), 2.10 (s, 3H), 1.69-1.83 (m, 4H). $C_{20}H_{26}S_4Sn$: Calcd C 46.79, H 5.10, S 24.98; Found C 46.94, H 4.99, S 24.87. ESI-MS (*m/z*): Calcd. 514.0; Found 514.1.

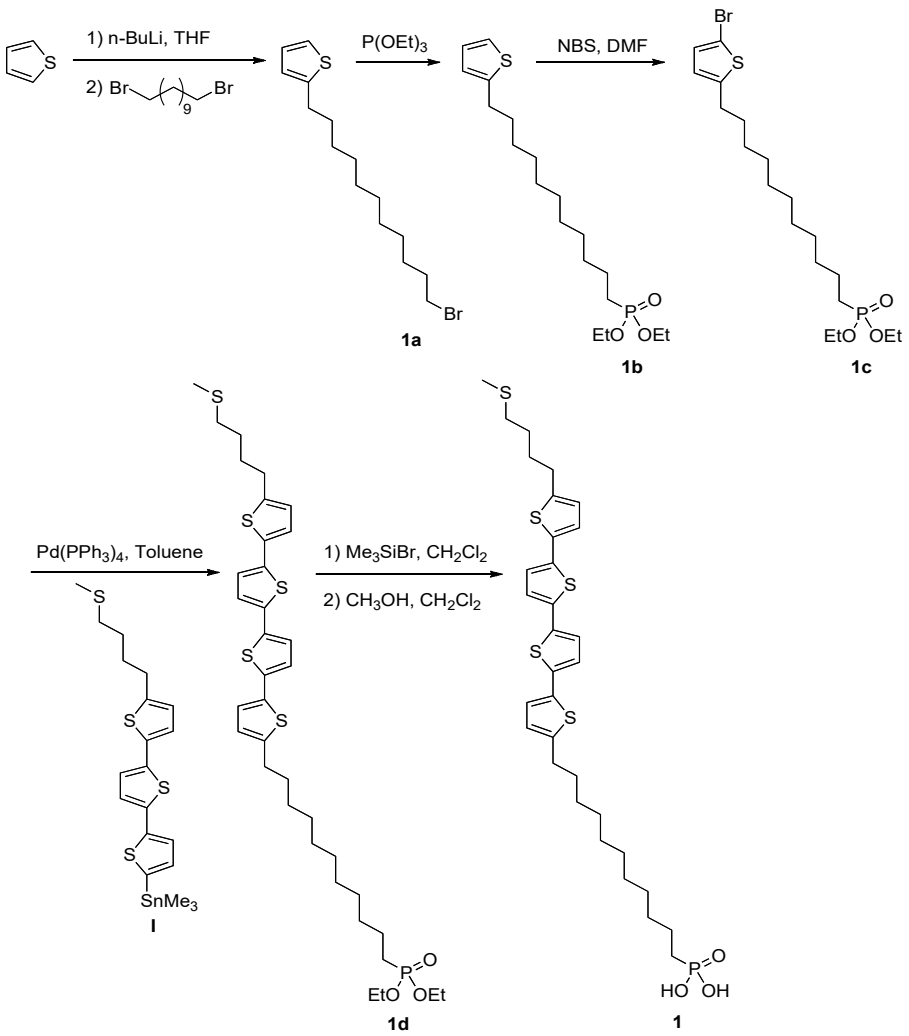

Figure 5.2. Synthesis of 11-(4-methylthiobutylquaterthiophenyl)undecylphosphonic acid. Reprinted with permission from [57]. Copyright 2015, Wiley-VCH Verlag GmbH & Co. KGaA.

2-(11-Bromoundecyl)thiophene (1a): To a solution of thiophene (1.26 g, 15.0 mmol) in dry THF (20 mL) under nitrogen, a solution of n-butyl lithium in hexanes (2.5 M, 6.0 mL, 15.0 mmol) was dropwise added at –78 °C. The suspension was stirred for one hour at –78 °C. 1,11-Dibromoundecane (4.71 g, 3.53 mL, 15.0 mmol) was dropwise added. The reaction mixture was slowly warmed up to room temperature and stirred overnight. The mixture was quenched with water and extracted with ether. The organic layer was washed with water, collected and dried over $MgSO_4$. After removal of the solvent by rotary evaporation under reduced pressure, the crude

product was purified over silica gel column chromatography with hexane as the eluent to afford a colorless liquid (4.07 g, 86%). ^{1}H NMR (300 MHz, $CDCl_3$): δ 7.09 (d, 1H, J = 5.4 Hz), 6.91 (dd, 1H, J = 5.1, 3.3 Hz), 6.77 (d, 1H, J = 3.3 Hz), 3.41 (t, 2H, J = 6.9 Hz), 2.81 (t, 2H, J = 7.5 Hz), 1.20-1.88 (m, 18H). $C_{15}H_{25}BrS$: Calcd C 56.77, H 7.94, Br 25.18; Found C 56.95, H 7.80, Br 25.25. ESI-MS (*m/z*): Calcd. 316.1; Found 316.1.

Diethyl 11-(2-thienyl)undecylphosphonate (1b): A mixture of 1a (3.96 g, 12.5 mmol) and triethyl phosphite (19.1 g, 20.0 mL) was heated under nitrogen at 150 °C for 21 h. The excess of triethyl phosphite was removed by distillation under vacuum. The crude product was purified over silica gel column chromatography with methylene chloride to methylene chloride/ethyl acetate (1:1) as the eluents to afford a colorless liquid (2.42 g, 52%). ^{1}H NMR (300 MHz, $CDCl_3$): δ 7.10 (dd, 1H, J = 5.1, 1.2 Hz), 6.91 (dd, 1H, J = 5.1, 3.6 Hz), 6.77 (dd, 1H, J = 3.6, 1.2 Hz), 4.06-4.13 (m, 4H), 2.81 (t, 2H, J = 7.2 Hz), 1.20-1.80 (m, 24H). $C_{19}H_{35}O_3PS$: Calcd C 60.93, H 9.42, P 8.27, S 8.56; Found C 61.09, H 9.25, P 8.19, S 8.67. ESI-MS (*m/z*): Calcd. 374.2; Found 374.3.

Diethyl 11-(5-bromo-2-thienyl)undecylphosphonate (1c): To a solution of 1b (2.37 g, 6.3 mmol) in anhydrous DMF (15 mL) in darkness under nitrogen at room temperature was portionwise added NBS (1.12 g, 6.3 mmol). The reaction mixture was stirred overnight at room temperature and quenched with water. The DMF solvent was removed from the mixture by rotary evaporation under reduced pressure followed by extracting with methylene chloride. The organic layer was washed with water, collected and dried over $MgSO_4$. After removal of the solvent by rotary evaporation under reduced pressure, the crude product was purified over silica gel column chromatography with methylene chloride to methylene chloride/ethyl acetate (1:1) as the eluents to afford a colorless liquid (2.48 g, 86%). ^{1}H NMR (300 MHz, $CDCl_3$): δ 6.84 (d, 1H, J = 3.6 Hz), 6.52 (d, 1H, J = 3.6 Hz), 4.06-4.12 (m, 4H), 2.73 (t, 2H, J = 7.2 Hz), 1.20-1.80 (m, 24H). $C_{19}H_{34}BrO_3PS$: Calcd C 50.33, H 7.56, Br 17.62, P 6.83, S 7.07; Found C 50.53, H 7.42, Br 17.53, P 6.94, S 7.18. ESI-MS (*m/z*): Calcd. 452.1; Found 452.1.

Diethyl 11-(4-methylthiobutylquaterthiophenyl)undecylphosphonate (1d): To a mixture of 1c (90.7 mg, 0.20 mmol) and I (103.0 mg, 0.20 mmol) in anhydrous toluene (20 mL) under nitrogen was added $Pd(PPh_3)_4$ (4.6 mg, 0.004 mmol) at room temperature. The reaction mixture was stirred overnight at 90 °C, cooled down to room temperature and quenched with water. The toluene solvent was removed from the mixture by rotary evaporation under reduced pressure followed by extracting with methylene chloride. The organic layer was washed with water, collected and dried

over $MgSO_4$. After removal of the solvent by rotary evaporation under reduced pressure, the crude product was purified over silica gel column chromatography with methylene chloride to methylene chloride/ethyl acetate (1:1 to 1:2) as the eluents to afford an orange solid (107.0 mg, 74%). ^{1}H NMR (300 MHz, $CDCl_3$): δ 6.97-7.04 (m, 6H), 6.67-6.71 (m, 2H), 4.06-4.12 (m, 4H), 2.73-2.86 (m, 4H), 2.54 (t, 2H, J = 7.2 Hz), 2.10 (s, 3H), 1.20-1.86 (m, 30H). $C_{36}H_{51}O_3PS_5$: Calcd C 59.80, H 7.11, P 4.28, S 22.17; Found C 59.96, H 7.01, P 4.37, S 22.04. ESI-MS (*m/z*): Calcd. 722.2; Found 722.2.

11-(4-methylthiobutylquaterthiophenyl)undecylphosphonic acid (1): To a solution of 1d (102.0 mg, 0.14 mmol) in dry methylene chloride (15 mL) under nitrogen was dropwise added bromotrimethylsilane (Me_3SiBr, 129.0 mg, 0.11 mL, 0.84 mmol). The mixture was stirred overnight at room temperature followed by the removal of solvent and excess of Me_3SiBr via rotary evaporation under reduced pressure. The residue was dissolved in a mixture of methylene chloride (15 mL) and methanol (20 mL), and stirred overnight at room temperature followed by the removal of solvent via rotary evaporation under reduced pressure to collect an orange-red solid (79.0 mg, 85%). ^{1}H NMR (300 MHz, $CDCl_3$): δ 6.97-7.05 (m, 6H), 6.67-6.72 (m, 2H), 2.73-2.86 (m, 4H), 2.54 (t, 2H, J = 7.2 Hz), 2.10 (s, 3H), 1.20-1.86 (m, 24H). $C_{32}H_{43}O_3PS_5$: Calcd C 57.62, H 6.50, P 4.64, S 24.04; Found C 57.79, H 6.38, P 4.78, S 23.96. ESI-MS (*m/z*): Calcd. 666.2; Found 666.2.

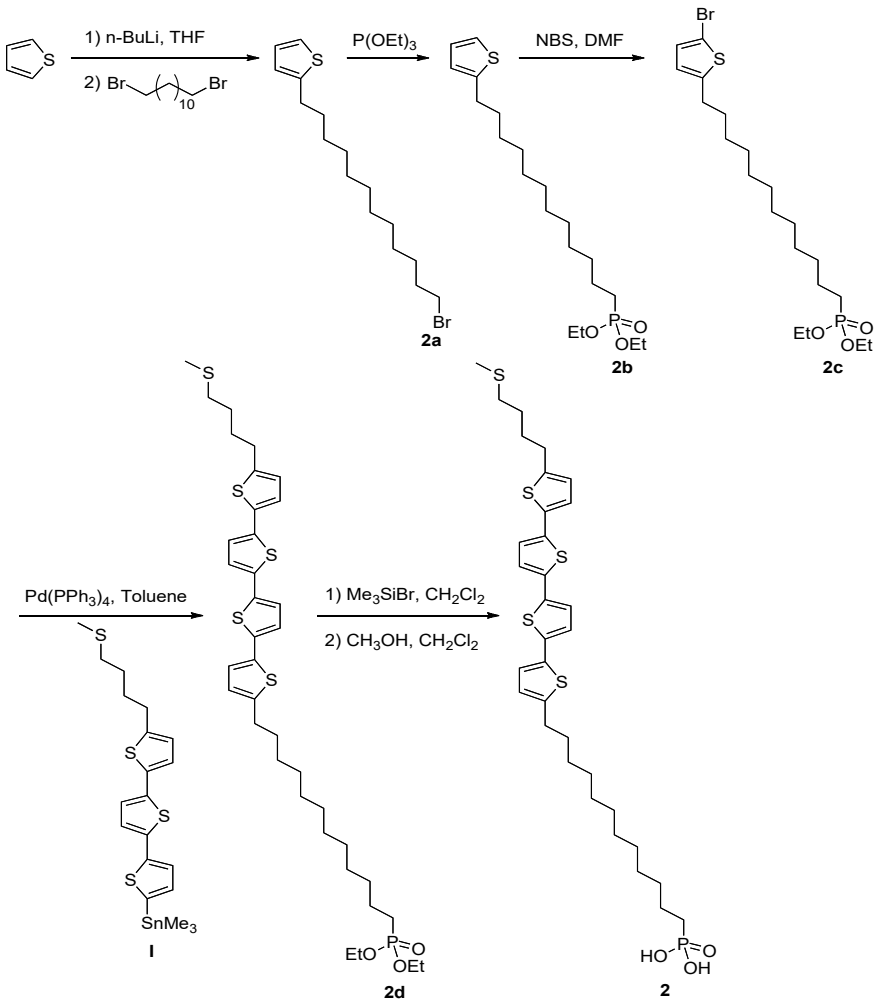

Figure 5.3. Synthesis of 12-(4-methylthiobutylquaterthiophenyl)dodecylphosphonic acid. Reprinted with permission from [57]. Copyright 2015, Wiley-VCH Verlag GmbH & Co. KGaA.

2-(12-Bromododecyl)thiophene (2a): To a solution of thiophene (2.52 g, 30.0 mmol) in dry THF (40 mL) under nitrogen, a solution of n-butyl lithium in hexanes (2.5 M, 12.0 mL, 30.0 mmol) was dropwise added at –78 °C. The suspension was stirred for one hour at –78 °C. A solution of 1,12-dibromododecane (9.84 g, 15.0 mmol) in dry THF (5 mL) was dropwise added. The reaction mixture was slowly warmed up to room temperature and stirred overnight. The mixture was quenched with water and extracted with ether. The organic layer was washed with water, collected and dried over $MgSO_4$. After removal of the solvent by rotary evaporation under reduced pressure, the crude product was purified over silica gel column chromatography with hexane as the eluent to afford a colorless liquid (6.16 g, 62%). ^{1}H NMR (300 MHz, $CDCl_3$): δ 7.08 (d, 1H, J = 5.4 Hz),

6.92 (dd, 1H, J = 5.1, 3.3 Hz), 6.78 (d, 1H, J = 3.3 Hz), 3.40 (t, 2H, J = 6.9 Hz), 2.81 (t, 2H, J = 7.5 Hz), 1.20-1.89 (m, 20H). $C_{16}H_{27}BrS$: Calcd C 58.00, H 8.21, Br 24.11; Found C 58.19, H 8.06, Br 24.27. ESI-MS (*m/z*): Calcd. 330.1; Found 330.1.

Diethyl 12-(2-thienyl)dodecylphosphonate (2b): A mixture of 2a (3.31 g, 10.0 mmol) and triethyl phosphite (57.3 g, 60.0 mL) was heated under nitrogen at 150 °C for 48 h. The excess of triethyl phosphite was removed by distillation under vacuum. The crude product was purified over silica gel column chromatography with methylene chloride to methylene chloride/ethyl acetate (1:1) as the eluents to afford a colorless liquid (1.90 g, 49%). ^{1}H NMR (300 MHz, $CDCl_3$): δ 7.10 (dd, 1H, J = 5.1, 1.2 Hz), 6.92 (dd, 1H, J = 5.1, 3.6 Hz), 6.78 (dd, 1H, J = 3.6, 1.2 Hz), 4.06-4.13 (m, 4H), 2.82 (t, 2H, J = 7.2 Hz), 1.20-1.82 (m, 26H). $C_{20}H_{37}O_3PS$: Calcd C 61.82, H 9.60, P 7.97, S 8.25; Found C 61.97, H 9.49, P 8.06, S 8.14. ESI-MS (*m/z*): Calcd. 388.2; Found 388.1.

Diethyl 12-(5-bromo-2-thienyl)dodecylphosphonate (2c): To a solution of 2b (1.83 g, 4.7 mmol) in anhydrous DMF (15 mL) in darkness under nitrogen at room temperature was portionwise added NBS (0.84 g, 4.7 mmol). The reaction mixture was stirred overnight at room temperature and quenched with water. The DMF solvent was removed from the mixture by rotary evaporation under reduced pressure followed by extracting with methylene chloride. The organic layer was washed with water, collected and dried over $MgSO_4$. After removal of the solvent by rotary evaporation under reduced pressure, the crude product was purified over silica gel column chromatography with methylene chloride to methylene chloride/ethyl acetate (1:1) as the eluents to afford a colorless liquid (2.03 g, 92%). ^{1}H NMR (300 MHz, $CDCl_3$): δ 6.84 (d, 1H, J = 3.6 Hz), 6.52 (d, 1H, J = 3.6 Hz), 4.06-4.12 (m, 4H), 2.73 (t, 2H, J = 7.8 Hz), 1.20-1.80 (m, 26H). $C_{20}H_{36}BrO_3PS$: Calcd C 51.39, H 7.76, Br 17.09, P 6.63, S 6.86; Found C 51.57, H 7.61, Br 17.24, P 6.77, S 6.69. ESI-MS (*m/z*): Calcd. 466.1; Found 466.1.

Diethyl 12-(4-methylthiobutylquaterthiophenyl)dodecylphosphonate (2d): To a mixture of 2c (93.5 mg, 0.20 mmol) and I (103.0 mg, 0.20 mmol) in anhydrous toluene (20 mL) under nitrogen was added $Pd(PPh_3)_4$ (4.6 mg, 0.004 mmol) at room temperature. The reaction mixture was stirred overnight at 90 °C, cooled down to room temperature and quenched with water. The toluene solvent was removed from the mixture by rotary evaporation under reduced pressure followed by extracting with methylene chloride. The organic layer was washed with water, collected and dried over $MgSO_4$. After removal of the solvent by rotary evaporation under reduced pressure, the crude product was purified over silica gel column chromatography with methylene chloride to methylene

chloride/ethyl acetate (1:1) as the eluents to afford an orange solid (94.0 mg, 64%). ^{1}H NMR (300 MHz, $CDCl_3$): δ 6.97-7.04 (m, 6H), 6.67-6.71 (m, 2H), 4.06-4.12 (m, 4H), 2.76-2.86 (m, 4H), 2.54 (t, 2H, J = 7.2 Hz), 2.10 (s, 3H), 1.20-1.84 (m, 32H). $C_{37}H_{53}O_3PS_5$: Calcd C 60.29, H 7.25, P 4.20, S 21.75; Found C 60.45, H 7.12, P 4.33, S 21.69. ESI-MS (*m/z*): Calcd. 736.2; Found 736.2.

12-(4-methylthiobutylquaterthiophenyl)dodecylphosphonic acid (2): To a solution of 2d (89.0 mg, 0.12 mmol) in dry methylene chloride (15 mL) under nitrogen was dropwise added Me_3SiBr (110.0 mg, 0.093 mL, 0.72 mmol). The mixture was stirred overnight at room temperature followed by the removal of solvent and excess of Me_3SiBr via rotary evaporation under reduced pressure. The residue was dissolved in a mixture of methylene chloride (15 mL) and methanol (20 mL), and stirred overnight at room temperature followed by the removal of solvent via rotary evaporation under reduced pressure to collect an orange solid (70.2 mg, 86%). ^{1}H NMR (300 MHz, $CDCl_3$): δ 6.97-7.05 (m, 6H), 6.67-6.72 (m, 2H), 2.76-2.86 (m, 4H), 2.54 (t, 2H, J = 7.2 Hz), 2.10 (s, 3H), 1.20-1.82 (m, 26H). $C_{33}H_{45}O_3PS_5$: Calcd C 58.20, H 6.66, P 4.55, S 23.54; Found C 58.39, H 6.50, P 4.64, S 23.46. ESI-MS (*m/z*): Calcd. 680.2; Found 680.2.

5.2.2 *SAM Assembly and Device Fabrication*

5.2.2.1 *Substrate preparation*

For high-voltage SAMFETs, heavily p-doped Si/300 nm SiO_2 substrates were cleaned by immersion into a piranha solution (30% aqueous hydrogen peroxide and 12 M sulfuric acid in a 1:3 volume ratio), extensively rinsed with deionized water and then dried with nitrogen gas. Substrates were then plasma cleaned in a Diener Fempto Plasma Cleaner for 30 min resulting in a 2-3 nm layer of AlOx as described previously [46]. Substrates were then immediately used for SAM assembly.

For low-voltage SAMFETs, heavily p-doped Si substrates were cleaned by immersion into a piranha solution (30% aqueous hydrogen peroxide and 12 M sulfuric acid in a 1:3 volume ratio), extensively rinsed with deionized water and then dried with nitrogen gas and then used immediately for the formation of hafnium oxide (HfO_2) dielectric. HfO_2 dielectric was prepared in a similar manner as described previously [45]. HfO_2 was prepared by dissolving hafnium (IV) chloride ($HfCl_4$) (Aldrich, 99.9%) in ethanol (EtOH) under a dry nitrogen environment, followed

by the addition of nitric acid (HNO_3) and DI water in air (molar ratio of $HfCl_4$:EtOH:HNO_3:H_2O is 1:205:5:5). The solution is then filtered with a 0.2 μm PTFE filter and heated at 50 ºC for 3 hours. The cooled solution is then spun-cast on the previously cleaned substrates at 5000 rpm for 30 seconds, left to sit for 1 hour and then annealed at 550 ºC for 30 minutes. Once substrates are cooled, they are used immediately for SAM assembly.

5.2.2.2 *SAM preparation, assembly, and cleaning*

SAMs of MTB4TC11 or MTB4TC12 were prepared by dissolving the molecules under a dry nitrogen environment in anhydrous dimethylsulfoxide (DMSO) (0.1 mM concentration) at 60 ºC for 48 hours. The SAM solution was then allowed to cool and filtered with a 0.45 μm PTFE filter. Prepared substrates as described in 5.2.2.1 were then immersed in SAM solutions, sealed, and allowed to assemble over the course of 72 hours. During SAM assembly, the solutions were held at either 25, 60, 90, or 120 ºC. The solutions were then allowed to cool to room temperature and the substrates removed. The substrates with assembled SAMs were then cleaned via spin-rinsing at 3000 rpm with anhydrous DMSO, tetrahydrofuran, and hexanes. At no point during assembly and cleaning were the substrates with assembled SAMs removed from their initial dry nitrogen environment.

5.2.2.3 *Au source and drain electrode evaporation*

Shadow masks were then used to fabricate 40 nm thick Au source and drain electrodes on cleaned SAMs using standard thermal evaporation under high vacuum (10E-7 Torr).

5.2.2.4 *Explanation of anneal before and anneal after*

Devices that are defined as “Anneal Before” are annealed at 120 °C before the evaporation of Au source and drain electrodes under a dry nitrogen environment for 10 hours. Devices that are defined as “Anneal After” are annealed at 120 °C under a dry nitrogen environment for 10 hours after Au source and drain electrodes have been evaporated on top of the SAM semiconductor.

After device fabrication and annealing transistor electrical characterization was completed in an inert environment with an Agilent 4155B semiconductor parameter analyzer.

5.2.3 *AFM and Contact Angle Goniometry*

Digital Instruments Multimode Nanoscope IIIa scanning probe microscope (Veeco Instruments, Plainview, NY) was used in AFM tapping mode. Aqueous static contact angle values were taken with a VCA Optima Surface Analysis System (Adv. Surface Technology Products, Billerica, MA) and are an average of five measurements with a standard deviation of less than ±3°.

5.2.4 *X-ray Photoelectron Spectroscopy*

MTB4TC12 SAM semiconductor was assembled on AlO_x/300 nm SiO_2/Si substrates at 25 °C and 120 °C, cleaned via sonication in DMSO, THF, and hexanes then subsequently characterized via X-ray photoelectron spectroscopy. Measurements were performed on a Kratos AXIS Ultra DLD instrument using a monochromatic Al Kα X-ray source and a 0° takeoff angle in hybrid mode. The compositional scans were acquired using an analyzer pass energy of 80 eV. Error bars in the reported data represent the standard deviation of the average of the three spots on two samples. Data analysis was performed with the CASA XPS software package. The results are summarized in Table 5.1.

5.2.5 *Near-Edge X-ray Absorption Fine Structure Spectroscopy (NEXAFS)*

NEXAFS spectra were collected at the National Synchrotron Light Source (NSLS) U7A beamline at Brookhaven National Laboratory, using an elliptically polarized beam with 85% p-polarization. This beamline is equipped with a monochromator (600 lines/mm grating) which provides a full width at half-maximum (fwhm) resolution of 0.15 eV at the carbon K-edge. At the carbon K-edge, the monochromator energy scale was calibrated using the intense C 1s−π* transition at 285.35 eV of a graphite transmission grid placed in the path of the X-rays and partial electron yield was monitored by a detector with the bias voltage maintained at −150 V. Samples were mounted to allow rotation and changing the angle between the sample surface and the

synchrotron X-rays. The NEXAFS angle is defined as the angle between the incident light and the sample surface. A molecular rotation (twist angle) of 0° was assumed for the tilt angle calculations [186].

5.3 Results and Discussion

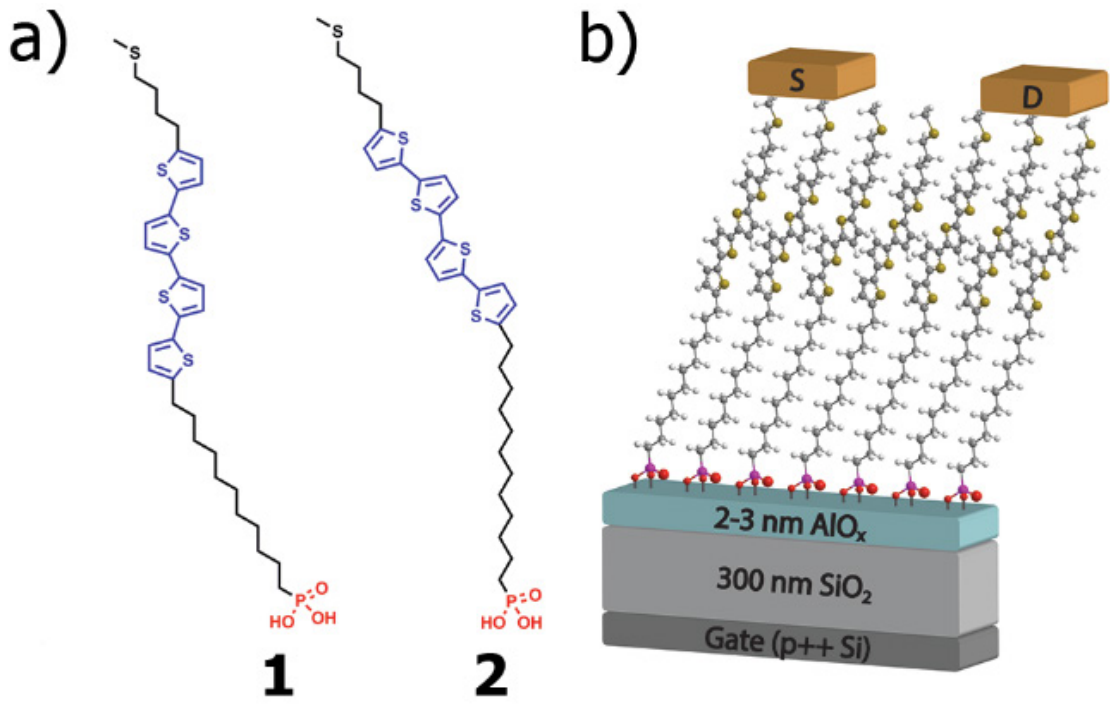

Figure 5.4. SAM semiconductor structure and high-voltage SAMFET device schematic. a) Molecular structures of SAM semiconductors used in this study, 1 MTB4TC11 and 2 MTB4TC12; b) schematic of high-voltage SAMFETs fabricated. Reprinted with permission from [57]. Copyright 2015, Wiley-VCH Verlag GmbH & Co. KGaA.

The SAM molecules, (11-(5'''-(4-(methylthio)butyl)-[2,2':5',2'':5'',2'''-quaterthiophen]-5-yl)undecyl)phosphonic acid (MTB4TC11) and (12-(5'''-(4-(methylthio)butyl)-[2,2':5',2'':5'',2'''-quaterthiophen]-5-yl)dodecyl)phosphonic acid (MTB4TC12), used in this study are designed in such a manner to promote efficient charge injection between the semiconducting core and chosen electrode. As shown in Figure 5.4a the molecule is comprised of a phosphonic acid binding group which allows for the covalent attachment to a variety of metal oxides [96]. A flexible undecyl or

dodecyl spacer unit is chosen to promote self-assembly and optimal π-π overlap due to its conformational freedom [187]. A quaterthiophene unit is chosen as the semiconducting core due to its proven ability to work as a semiconductor in both thin film [187] and monolayer [188] transistors. Finally, to achieve efficient charge injection into the SAM a functional terminal group composed of methylthiobutyl is chosen. In order to enhance charge injection and minimize contact resistance, the terminal group is designed to take advantage of the well-known gold-sulfide coordinate bond that occurs between the two species [189]. In particular, methylsulfide has been used in the past as an anchoring group for molecular junctions due to its ability to electronically couple with gold [190]. To take advantage of this intimate contact, a simple top-contact bottom-gate transistor architecture is used (Figure 5.4b). This will simplify the device architecture compared to those reported for previous high performance SAMFETs [56, 63].

5.3.1 *Impact of Thermal Annealing on SAMFETs*

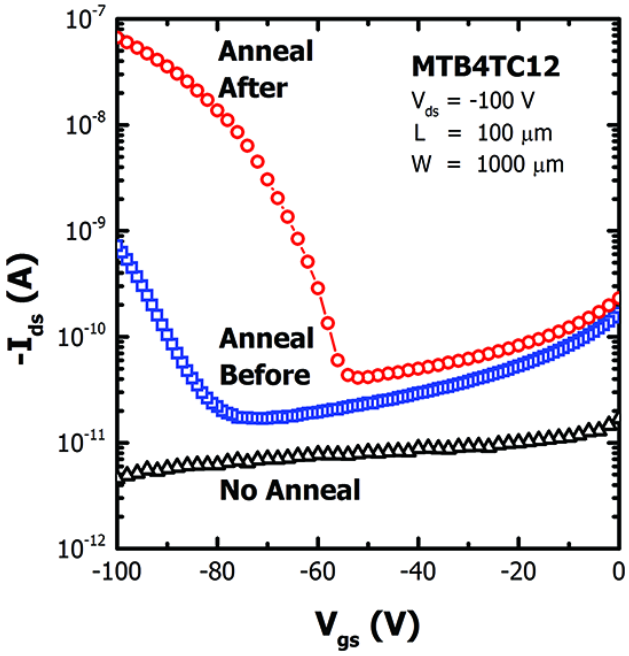

Figure 5.5. Transfer characteristics of high-voltage MTB4TC12 SAMFETs with various annealing conditions. Anneal before indicates SAM annealing at 120 °C for 10 hours before electrode deposition and anneal after, indicates SAM annealing at 120 °C for 10 hours after electrode deposition. Reprinted with permission from [57]. Copyright 2015, Wiley-VCH Verlag GmbH & Co. KGaA.

In order to better understand the dynamics of the coordinate bond between the SAM molecules and gold electrodes high-voltage SAMFETs are first fabricated and the impact of thermal annealing on device performance is also examined. SAMs are assembled via immersion at room temperature on a traditional dielectric platform (Figure 5.4b) previously used by our group for both thin film transistors [66] and SAMFETs [191]. After SAM assembly and cleaning to remove aggregates, substrates are annealed either before or after gold electrode deposition at 120 °C for 10 h. Remarkably, Figure 5.5 shows a considerable difference in representative transfer electrical characteristics when comparing devices that are not annealed, annealed before electrode deposition, and annealed after electrode deposition. Devices not annealed show no performance with the inability to act as a switch. Figure 5.6a shows that devices annealed before electrode deposition have some limited charge mobility of around 10^{-5} cm^2 V^{-1} s^{-1} while devices annealed

after electrode deposition show two orders of magnitude increase in charge mobility to 10^{-3} cm2 V^{-1} s^{-1}.

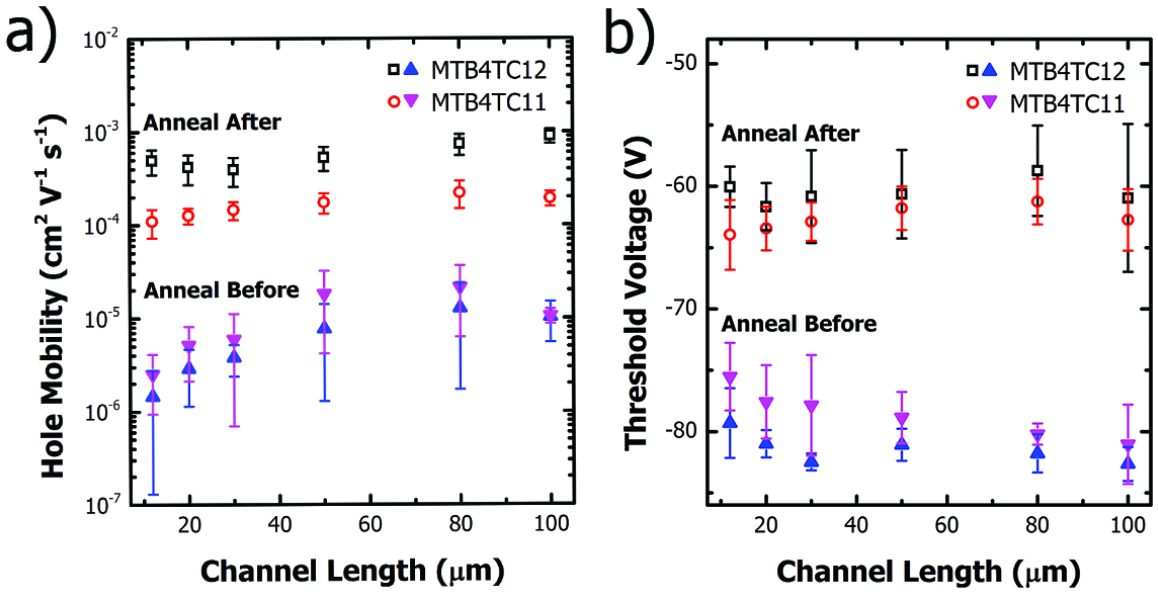

Figure 5.6. High-voltage transistor performance parameters for a) hole mobility and b) threshold voltage based on SAM semiconductor and annealing route. Data are averaged of approximately 7 devices per channel length and are for transistors with a channel width of 1000 μm. Reprinted with permission from [57]. Copyright 2015, Wiley-VCH Verlag GmbH & Co. KGaA.

In terms of yield, roughly half of all devices annealed before electrode deposition function properly, while the yield for devices annealed after electrode deposition is near unity. Interestingly, this enhancement is accompanied by a shift in apparent threshold voltage (*Vt*) as can be seen in Figure 5.6b. Devices annealed before or after electrode deposition exhibited an apparent threshold voltage of around -80 V and -65 V respectively. While *Vt* remains constant across tested channel lengths regardless of odd or even alkyl chain of SAMFET molecules, the impact of annealing before or after electrode deposition plays a clear role and elucidates a potential mechanism for the shown performance enhancement.

Vt is generally thought to be related to the surface density of deeply trapped charges in the channel and contact region of a transistor [192]. Deep traps, which are considered to be a few kT above the highest occupied molecular orbital, may occur due to structural defects and impurities [105]. It is likely that the deposition of gold on top of the SAM semiconductor resulted in the formation of such trap states through the creation of local structural disorder. The morphology of unannealed gold on top of the SAM (Figure 5.7a) shows morphology consistent with having a high density of trap sites due to the numerous small grains and subsequent grain boundaries. However, upon annealing at 120 °C (Figure 5.7b), these grains coarsen to form large interconnected grains. Evidence of this morphology change indicates that the gold atoms are able to reorganize to a more energetically favorable morphology to allow for better contact between electrode and SAM semiconductor resulting in reduced trap sites. This reduction in trap site density due to grain coarsening may also be a contributing factor for the mobility enhancement that occurs upon annealing post electrode deposition.

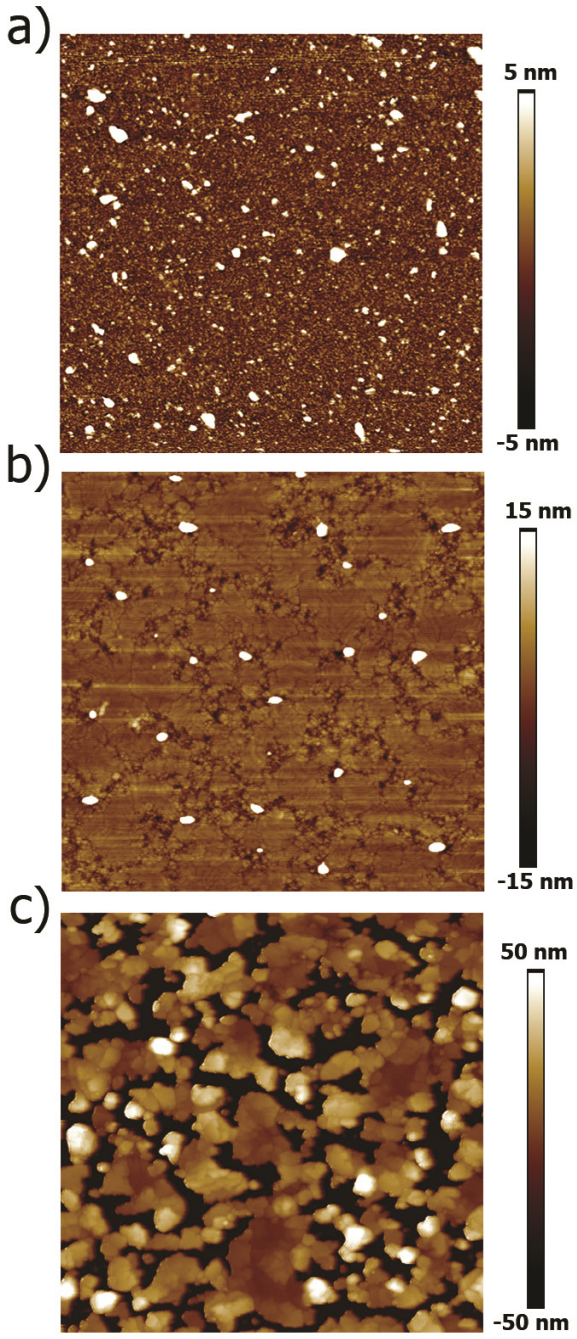

Figure 5.7. Representative morphology of Au on top of MTB4TC11 SAM assembled on AlO_x measured by AFM with different annealing conditions of a) no anneal, b) anneal after, and c) over annealed substrates. Reprinted with permission from [57]. Copyright 2015, Wiley-VCH Verlag GmbH & Co. KGaA.

Another mechanism for enhanced mobility is most likely related to a reduced charge injection barrier at the Au-SAM interface. A threshold voltage shift accompanied by improved mobility due to changes between metal electrodes and semiconductor has been found earlier for both thin film organic transistors with SAM modified gold electrodes and monolayer MoS_2 transistors with different metal electrodes [193, 194]. The reduced charge injection barrier for devices fabricated in this section is thought to be enabled by the intimate contact formed between the sulfur of the SAM semiconductor and the gold atoms. Thermal annealing after gold electrode deposition is needed to further strengthen the coordinate bond between SAM and electrode which requires a separation distance of less than 0.5 nm [195]. It is hypothesized that annealing post-electrode deposition provides enough thermal energy for reorganizing SAM molecules, gold atoms, or both to improve contact.

However, it is known that if temperatures are elevated to around 300 °C, the mobile gold atoms will cause the sulfide to desorb from the surface [196]. It was found that over annealing to above 150 °C will result in gold dewetting from the SAM surface and forming isolated islands of gold (Figure 5.7c). Such a phenomenon is accompanied by a significant reduction in device performance.

5.3.2 *Impact of SAM Immersion Assembly Temperature*

In order to further enhance SAMFET performance, SAM immersion assembly temperature is optimized. Traditionally, for the assembly of SAMs, solvents with a dielectric constant (ε_r) between 3 and 5 are found to be optimal. It is believed that if the solvent ε_r is below 3, SAMs tend to form micelles. If greater than 5, solvent will interact too strongly with the SAM to disrupt assembly at the substrate-solution interface [43, 71]. In our study, dimethyl sulfoxide (DMSO) was found to provide the greatest solubility allowing for higher SAM solution concentration without forming aggregate. However, DMSO has a relatively high dielectric constant (~46), which may limit the dense assembly of SAM.

High-voltage SAMFET devices using the same device architecture shown in Figure 5.4b with varying SAM immersion assembly temperatures were fabricated and characterized. Morphology of SAMs assembled at room temperature and 120 °C were found to be similar for both MTB4TC11 and MTB4TC12. SAMs assembled at room temperature had rms roughness values of 0.26 nm and

0.46 nm for MTB4TC11 and MTB4TC12, respectively while SAMs assembled at 120 °C had rms roughness values of 0.33 nm and 0.43 nm, respectively. Representative morphologies characterized by tapping mode atomic force microscopy are shown in Figure 5.8.

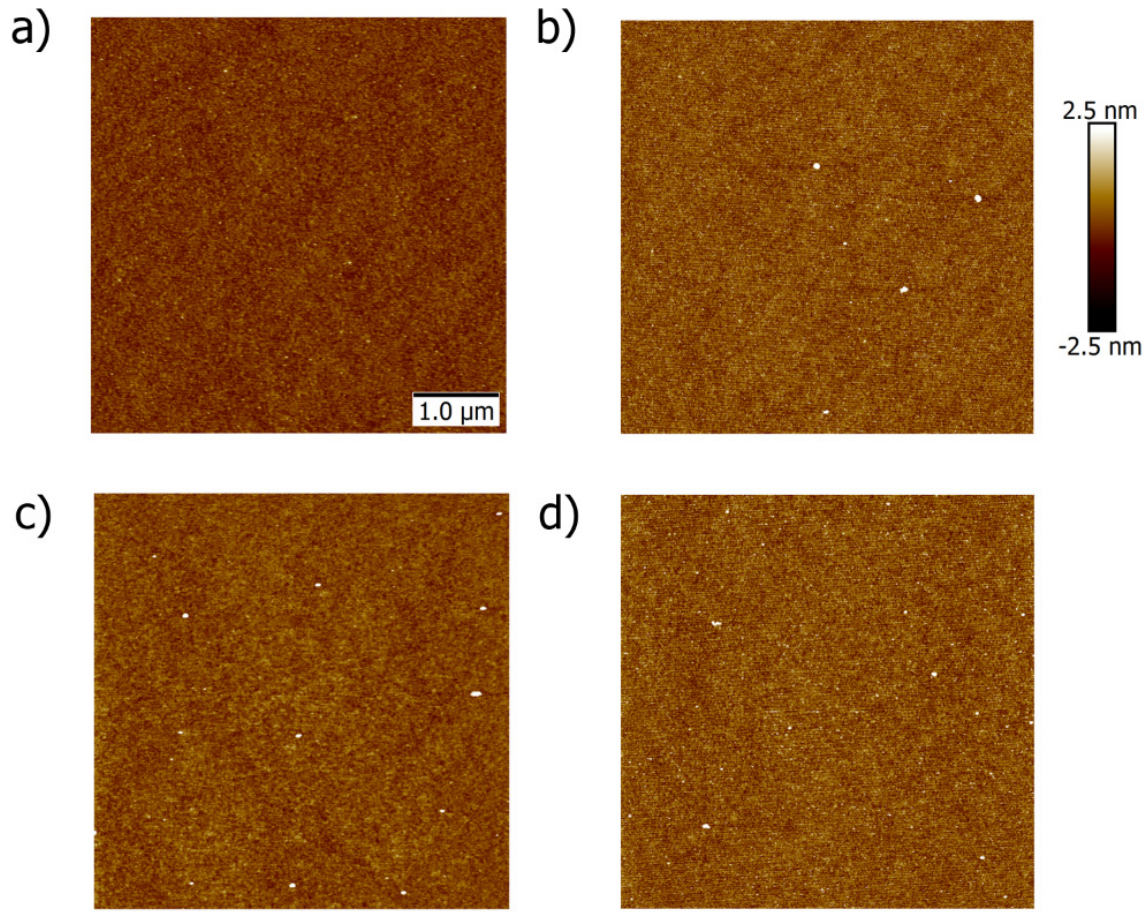

Figure 5.8. Representative morphology of semiconductor SAMs assembled on AlO_x/300 nm SiO_2/Si substrates at 25 °C and 120 °C. 5 µm x 5 µm AFM images of SAMs MTB4TC11 (a, c) and MTB4TC12 (b, d) assembled at 25 °C (a, b) and at 120 °C (c, d) on AlOx/300 nm SiO2/Si substrates. RMS roughness values of 0.262 nm (a), 0.463 nm (b), 0.332 nm (c), and 0.439 nm (d) were found. Reprinted with permission from [57]. Copyright 2015, Wiley-VCH Verlag GmbH & Co. KGaA.

The static water contact angle for MTB4TC12 SAMFETs was found to increase slightly from 71.4° ± 0.8° to 76.2° ± 0.9°, respectively, when comparing assembled at room temperature versus 120 °C. This slightly increased contact angle may be indicative of increased SAM density. The relationship between SAM assembly temperature and density is further corroborated from X-ray photoelectron spectroscopy data which suggests an approximately 30% increase in SAM density between room temperature and 120 °C assembly conditions (Table 5.4). The I_{S2p}/I_{Al2p} ratio determined from the elemental composition data is a direct measure of packing density. The data show an increased packing of the SAM at a 120 °C assembly temperature.

Table 5.1. Atomic composition (in atomic %) and intensity ratio derived from XPS spectra of MTB4TC12 SAM semiconductor assembled at different temperatures.

Assembly Temp (°C)	C	S	P	Al	$\boldsymbol{I_{S2p}/I_{Al2p}}^{a}$
25	77.6 (1.7)[b]	6.7 (0.3)	1.8 (0.2)	13.9 (1.8)	**1.5 (0.3)**
120	77.9 (0.7)	8.2 (0.3)	1.8 (0.1)	12.3 (0.9)	**2.1 (0.2)**

This improved SAM density results in an order of magnitude higher hole-mobility as shown in Figure 5.9. This follows an expected trend of increasing mobility with respect to assembly temperature from room temperature to 120 °C while other parameters such as on/off current ratio, threshold voltage, and subthreshold swing remain relatively constant regardless of assembly temperature (Figure 5.10). Representative transfer and output curves of high voltage SAMFETs with MTB4TC11 assembled are shown in Figure 5.11.

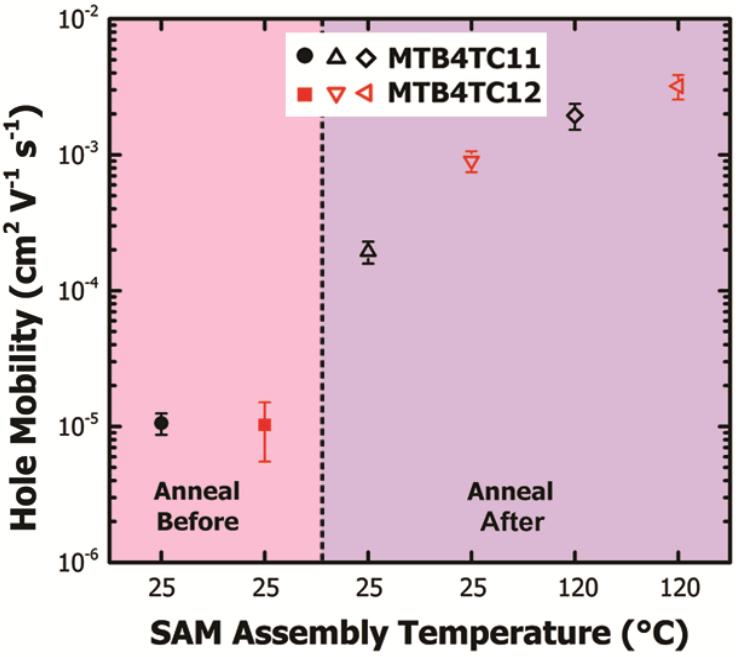

Figure 5.9. Hole mobility of high voltage SAMFETs with either MTB4TC11 or MTB4TC12 SAM semiconductor assembled at 25 °C or 120 °C. The first two left most data points indicate performance for devices annealed before electrode deposition while last four data points indicate performance for devices annealed after electrode deposition. Data is for transistors with channel width and length of 1000 µm and 100 µm respectively and is an average of at least 5 devices. Reprinted with permission from [57]. Copyright 2015, Wiley-VCH Verlag GmbH & Co. KGaA.

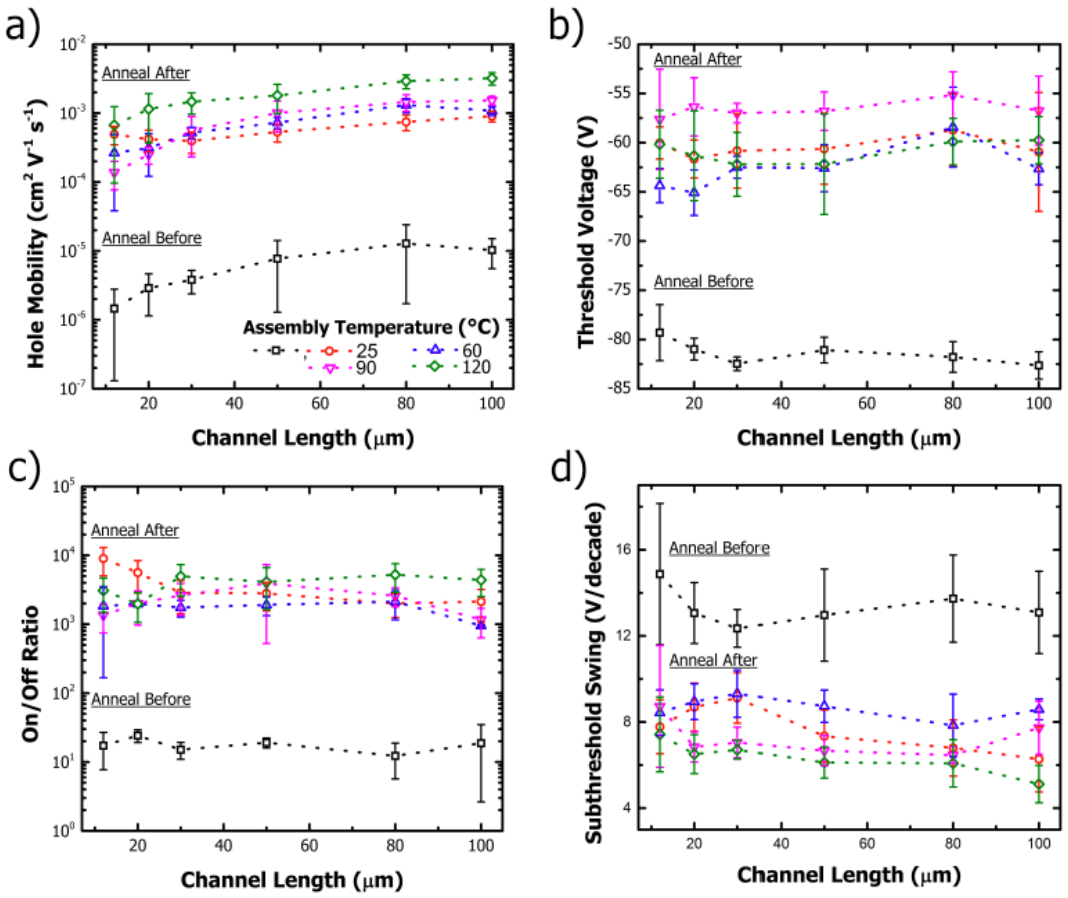

Figure 5.10. Average transistor performance characteristics of high voltage SAMFETs with MTB4TC12 SAM semiconductor prepared via immersion assembly at 25 °C, 60 °C, 90 °C, and 120 °C. Data also compares performance metric between devices annealed before and after Au electrode deposition. Performance metrics of hole mobility (a), threshold voltage (b), on/off ratio (c), and subthreshold swing (d) are average values of approximately 7 transistors per channel length. Reprinted with permission from [57]. Copyright 2015, Wiley-VCH Verlag GmbH & Co. KGaA.

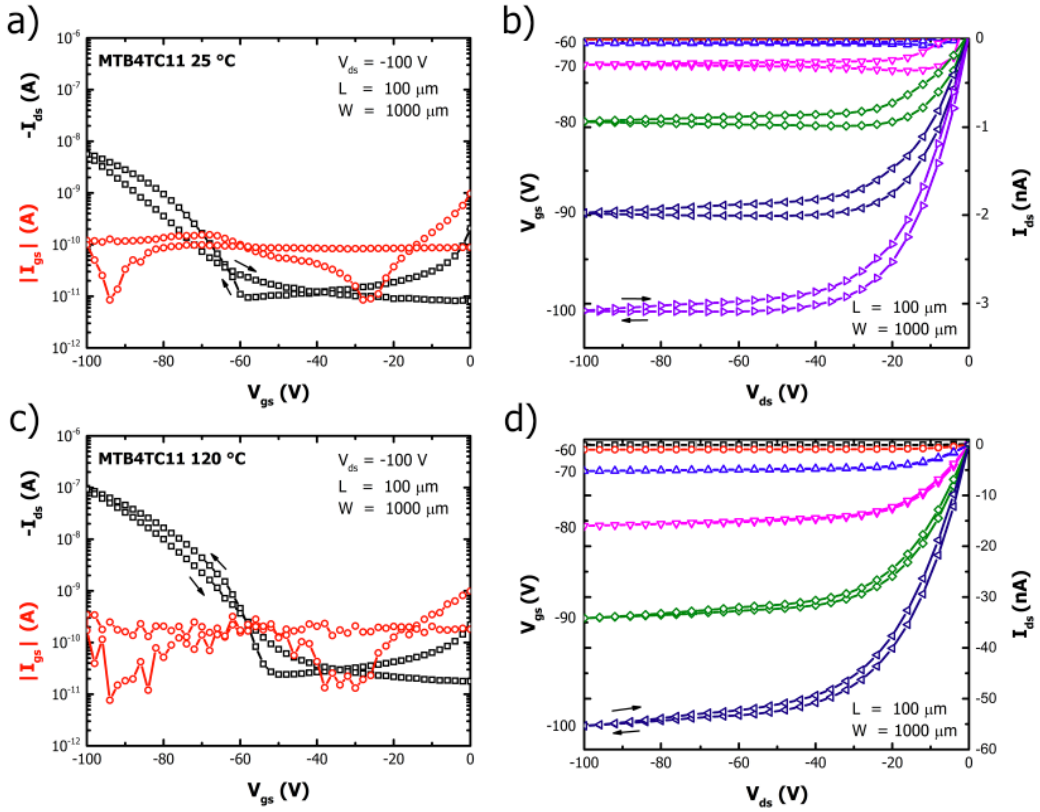

Figure 5.11. Electrical characteristics of high voltage SAMFETs that have been annealed after electrode deposition with MTB4TC11 semiconductor SAM assembled at 25 °C (a, b) and 120 °C (c, d). Representative transfer (a, c) and output (b, d) characteristics for transistors with channel width and length of 1000 µm and 100 µm and Vds held at -100 V. Reprinted with permission from [57]. Copyright 2015, Wiley-VCH Verlag GmbH & Co. KGaA.

5.3.3 *NEXAFS Characterization of SAMs and Impact of Annealing*

To obtain a better insight of the overall quality of SAMs assembled at 120 °C, the SAM/electrode interface, and the impact of annealing, SAMs of MTB4TC11 were characterized with near edge X-ray absorption fine structure (NEXAFS) spectroscopy. NEXAFS can provide chemical identification of specific bonds within SAMs and detailed information about molecular alignment [100]. Substrates with MTB4TC11 SAM were half covered with a 3 nm thick gold layer to allow for the characterization via NEXAFS of MTB4TC11 SAM with or without gold. After gold deposition, a subset of substrates were then annealed at 120 °C for 2 h to allow the determination of the influence of both gold and annealing post gold deposition.

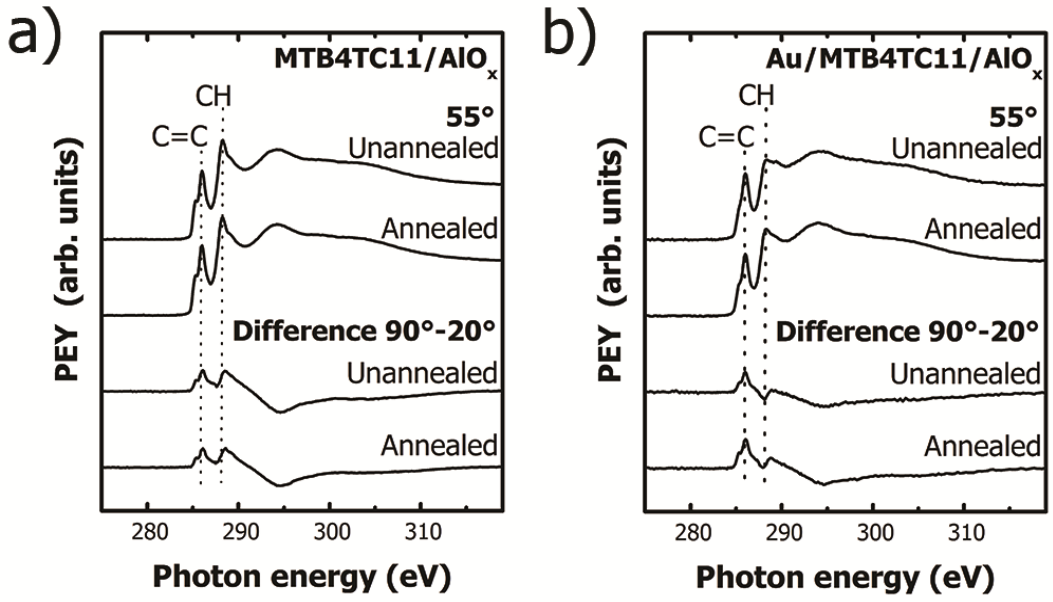

Figure 5.12. NEXAFS C K-edge spectra from unannealed and annealed samples of MTB4TC11 a) on AlO_x and b) covered by 3nm of Au. Each figure contains spectra collected at X-ray incidence angles of 55° (top traces) along with differences of spectra recorded at 90° and 20° (bottom traces). Reprinted with permission from [57]. Copyright 2015, Wiley-VCH Verlag GmbH & Co. KGaA.

Carbon K-edge spectra, collected at an x-ray incident angle of 55°, from annealed/unannealed versions of MTB4TC11 and Au coated MTB4TC11 are presented in Figure 5.12a and 5.12b. The absorption near 285 eV, related to π* C=C orbitals within the quaterthiophene groups, is present in all spectra taken from all variants of the MTB4TC11 SAM [197]. Moving to higher x-ray energies we observe a peak at 287 eV related to R*/C-H σ* molecular orbitals [198]. The orientation and ordering of molecular bonds can be assessed by changes in the x-ray absorption as the sample is rotated relative to the incident x-ray beam by θ. Difference spectra (90°-20°), from annealed/unannealed versions of MTB4TC11 and Au coated MTB4TC11 are also shown in Figures 5.12a and 5.12b.

Table 5.2. NEXAFS tilt angle calculations based on SAM semiconductor, annealing condition, and presence of Au

SAM	No Anneal	Anneal
MTB4TC11	29.5 (0.2)[a]	30.5 (0.1)
MTB4TC11/Au	26.3 (0.6)	24.4 (0.9)
B4TC11	30.0 (0.1)	30.7 (0.2)
B4TC11/Au	26.0 (0.4)	25.3 (0.7)

In all cases, the NEXAFS spectra show a high degree of ordering (positive dichroism) of π* C=C molecular orbitals. We have modeled the angle dependence of the π* resonance to calculate the orientation of the thiophene units before and after gold deposition using standard procedures [100]. Relative to the surface normal, the thiophene tilt angles for unannealed and annealed MTB4TC11 are 29.5° and 30.5° respectively. This apparent lack in change of tilt angle seems to indicate that annealing by itself may not result in significant molecular reorientation. However, upon depositing gold on top of the MTB4TC11 SAM the thiophene units became more upright. For the unannealed sample set, the thiophene tilt angle is determined to be 26.3°. For the sample set where gold was annealed after deposition on MTB4TC11 SAM, the thiophene tilt angle is determined to be 24.4°. The SAMs may become more upright when covered with gold due to the proposed coordinate bond between sulfur and gold. Additionally, the greater change in thiophene tilt angle between pristine SAM and SAM covered with gold (6° and 3° for annealed and

unannealed respectively) indicates annealing with gold facilitates an interaction between SAM and gold. A similar trend with the comparison molecule B4TC11 is also found (Table 5.2) which may indicate that the gold is not limited to interact with just the methyl sulfide functional group but may also interact with the sulfur present in the quaterthiophene semiconducting core. The molecular architecture can introduce some uncertainty in the angle determination (twist, torsion angles etc). These errors do not apply for systems which use the same molecules: MTB4TC11 or B4TC11 (before and after anneal, or before and after gold deposition). The error margin comparing within a given molecule set is less than 1 degree. Comparing between datasets we can assume a margin of 2.5 degree. We have some statistics because we use three different ratios within the dataset to calculate and we get standard deviations of about 0.2 degrees. The rest of the error includes experimental inaccuracies. Errors introduced by data analysis are largely eliminated because we use intensity ratios and not absolute values. So small inaccuracies induced by normalization cancel out. Overall, this NEXAFS dataset provides enough information to show that depositing gold on top of these SAMs results in the thiophenes orienting more upright which is then slightly increased with the addition of an annealing step.

5.3.4 *SAMFET Comparison With or Without Methylthio Functional Group*

In order to understand the influence of the methylthio functional group a comparison molecule ((11-(5'''-(4-butyl)-[2,2':5',2'':5'',2'''-quaterthiophen]-5-yl)undecyl)phosphonic acid, B4TC11) was fabricated. Comparing performance data of B4TC11 to MTB4TC11 allows us to further understand the advantages and disadvantages of the two functional groups. SAMs of B4TC11, MTB4TC11, and MTB4TC12 were fabricated on HfO_2 via the heated assembly procedure at 120 °C as described earlier for AlO_x. In order to verify the quality of SAM, static water contact angle for MTB4TC12 was determined at 77.1° ± 0.3° which is comparable to the data previously reported on AlO_x. Additionally, the contact angle of B4TC11 was found to be at 87.3° ± 0.4° which is comparable to literature data [58]. Furthermore, the rms roughness determined by AFM of MTB4TC12 was found to be 0.32 nm further indicating the presence of a quality monolayer on the HfO_2 dielectric platform (Figure 5.13) that is comparable to that of our AlO_x platform.

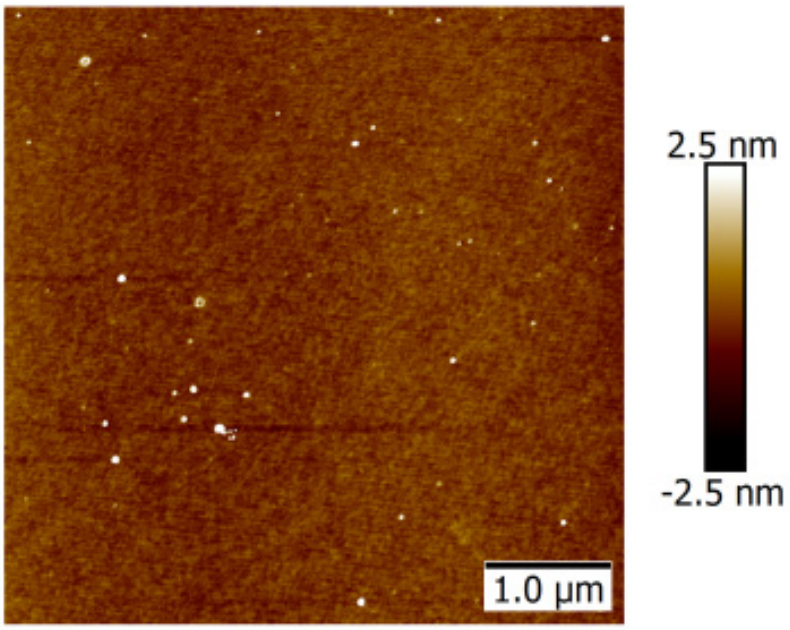

Figure 5.13. AFM image of MTB4TC12 on a HfO_2/300 nm SiO_2/Si dielectric stack assembled at 120 °C with an rms roughness of 0.329 nm. Reprinted with permission from [57]. Copyright 2015, Wiley-VCH Verlag GmbH & Co. KGaA.

Performance data for the series of fabricated devices can be seen in Figure 5.14a. Surprisingly, it was found that our control molecule B4TC11 yielded a hole mobility of 0.00213 $cm^2\ V^{-1}\ s^{-1}$ for pristine unannealed devices. However, upon annealing the devices at 120 °C for 10 h after electrode deposition the hole mobility was reduced by nearly an order of magnitude. A similar trend was also seen for an even lower temperature anneal of 80 °C. This reduction in hole mobility seems to indicate that devices with only a butyl functional head group have limited thermal stability and that annealing results in damage at the SAM/electrode interface. This damage may be caused by diffusion of gold molecules into the SAM semiconductor core at said interface resulting in interface of local SAM molecular order that is integral for charge carrier transport. Comparatively, our MTB4TC11 and MTB4TC12 devices initially exhibit little to no performance without annealing. However, upon annealing after electrode deposition the hole mobility for MTB4TC11 and MTB4TC12 increases to 0.00356 $cm^2\ V^{-1}\ s^{-1}$ and 0.00737 $cm^2\ V^{-1}\ s^{-1}$ respectively. Additionally, since MTB4TC11 has slightly better mobility compared to unannealed B4TC11 and about an order of magnitude better hole mobility for annealed B4TC11 devices, the influence of the methylthio functional group seems to help slightly enhance device mobility as well as increase

thermal stability by protecting the semiconducting core from being damaged by the gold electrodes.

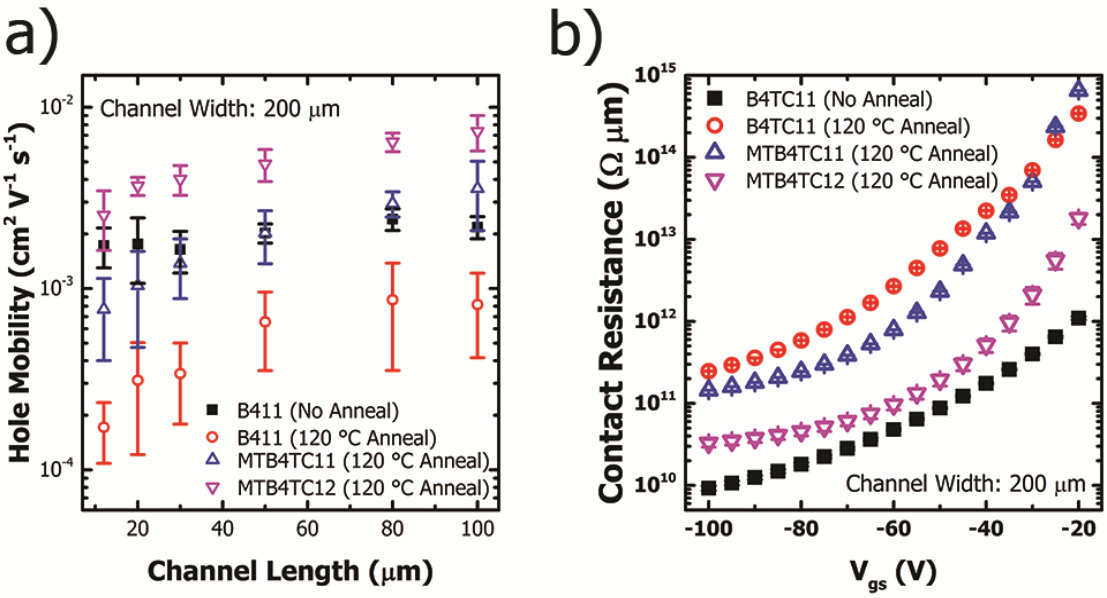

Figure 5.14. Comparison of hole mobility and contact resistance of high voltage SAMFETs consisting of MTB4TC11, MTB4TC12, and B4TC11 assembled on HfO_2. a) Hole mobility with respect to channel length for high voltage SAMFETs with a HfO_2/300nm SiO_2/Si dielectric/gate stack and SAM semiconductors B4TC11, MTB4TC11, and MTB4TC12. Performance is indicated if devices are not annealed or are annealed at 120 °C for 10 h after 50 nm Au electrode deposition. b) Contact resistance with respect to gate-source voltage of high-voltage SAMFETs with HfO_2 dielectric stack. Reprinted with permission from [57]. Copyright 2015, Wiley-VCH Verlag GmbH & Co. KGaA.

5.3.5 *SAMFET Contact Resistance*

In order to further understand the influence of the SAM functional head group, contact resistance was determined using a modified transmission line method [199]. Contact resistance with respect to gate-source voltage is shown in Figure 5.14b. It was found that even though MTB4TC12 exhibited the best device performance, the unannealed B4TC11 devices had the lowest contact resistance. This is reasonable given that it has the shortest functional head group of the systems tested. However, as expected, upon annealing after electrode deposition the contact

resistance of B4TC11 becomes the highest among tested architectures. MTB4TC12 exhibits contact resistance similar to unannealed B4TC11 indicating that not only does the functional head group play a role in contact resistance, but that even tilt angle differences between an odd and even number alkyl chain can result in a fairly significant difference in both contact resistance and performance.

5.3.6 *Low Voltage SAMFETs*

While high-voltage devices in this paper serve to elucidate the importance of device processing and design for SAMFETs, real-world applications rely on having low operating voltage devices. Optimized processing conditions have been used to fabricate low-voltage MTB4TC12 SAMFETs on a thin HfO_2 dielectric as seen in the insert of Figure 5.15a. HfO_2 is a proven high-k dielectric that has previously been used for low-voltage thin film organic transistors [45]. Approximately 8 nm thick HfO2 dielectric films were characterized by the fabrication of p++ Si/HfO2/Au metal-insulator-metal devices. Electrical characterization was done under a dry nitrogen environment utilizing an Agilent 4155B semiconductor parameter analyzer for current density vs. voltage and an HP 4284A precision LCR meter for capacitance vs. frequency measurements. Average capacitance of 565 nF cm-2 at 1 kHz frequency and current density of 2.1*10-8 A cm-2 at -3 V was found.

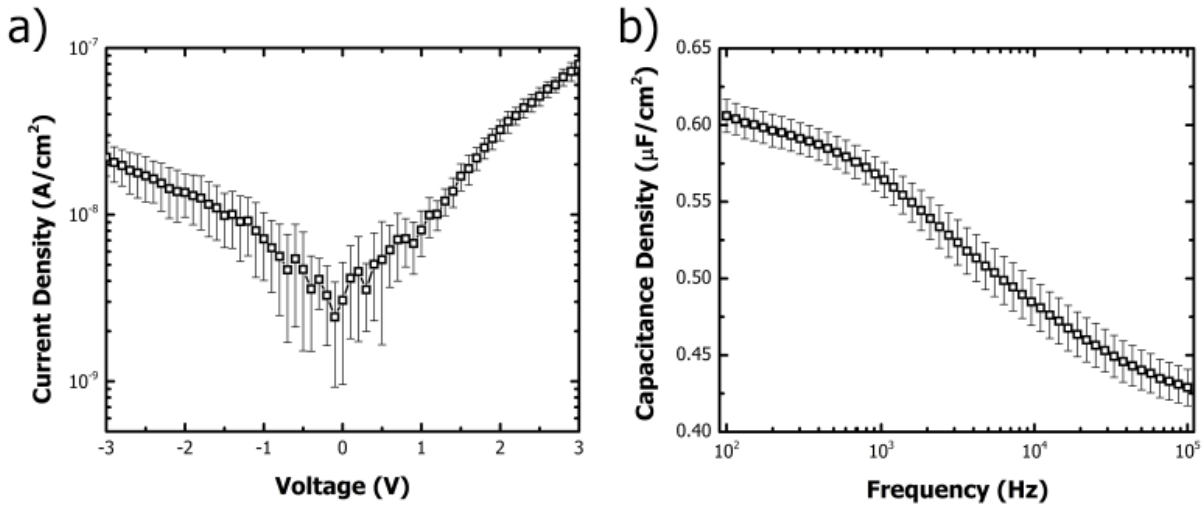

Figure 5.15. Characterization of metal-insulator-metal junctions for determination of HfO_2 current density and capacitance. Characteristic current density vs. voltage (a) and capacitance density vs frequency (b) for p++ Si/HfO_2/Au metal-insulator-metal junctions. Shown data is an average of approximately 15 devices. Reprinted with permission from [57]. Copyright 2015, Wiley-VCH Verlag GmbH & Co. KGaA.

However, it is important to take into account the additional capacitance provided by the dodecyl alkyl chain of the MTB4TC12 SAM used which is estimated to lower the total capacitance to 408 nF cm^{-2} (SI, Figure S8). From Figure S8, we are able to determine the capacitance of HfO_2 dielectric to be approximately 565 nF cm^{-2} at 1 kHz. For low-voltage SAMFET devices, the contribution from the dodecyl alkyl chain also contributes to the overall dielectric stack. Since this alkyl chain is attached to the SAM semiconducting core it is difficult to measure its contribution to total capacitance directly. Instead, we estimate the total capacitance by using the standard capacitance equations as seen below. Using data generated by our group previously [41] we can estimate the contribution of a dodecyl phosphonic acid SAM (DDPA) as follows:

$$\frac{1}{C_{total}} = \frac{1}{C_{HfO_2}} + \frac{1}{C_{DDPA}} \quad \therefore \quad \frac{1}{515\ nF\ cm^{-2}} = \frac{1}{792\ nF\ cm^{-2}} + \frac{1}{C_{DDPA}} \qquad (Eq.5.1)$$

This gives us an estimated capacitance contribution for DDPA of 1473 nF cm^{-2}. This value is comparable to that estimated by other groups at 1480 nF cm^{-2} [63]. Using this information we can then estimate the total capacitance for our HfO_2/SAM dielectric stack as follows:

$$\frac{1}{C_{total}} = \frac{1}{565\ nF\ cm^{-2}} + \frac{1}{1473\ nF\ cm^{-2}} \therefore \boldsymbol{C_{total}} = 408\ nF\ cm^{-2} \quad (Eq.5.2)$$

Low voltage SAMFETs exhibited excellent charge carrier mobility with the best hole-mobility reaching 0.015 $cm^2\ V^{-1}\ s^{-1}$ for devices with a channel width and length of 200 µm and 100 µm respectively. Figure 5.16a shows that mobility increases with decreasing channel width/length ratio indicating that total contact area is critical to device performance. A similar trend is also seen for high-voltage devices and is indicative of performance being limited by resistance within the transistor circuit [200]. As shown in Figure 5.16b and comparable to high voltage SAMFETs, on/off current ratios of 10^3 are found which stems from the reduced off current present in low voltage devices. Additionally, devices are found to have an excellent differential between drain-source current and gate-source leakage current at around 10^2. This exemplifies the high quality nature of our sol-gel HfO_2 hybrid dielectric as it is currently the highest reported value for low voltage SAMFET devices. Representative transfer and output characteristics for a device with channel width and length of 200 um and 100 um respectively is shown in Figure 5.16c and 5.16d.

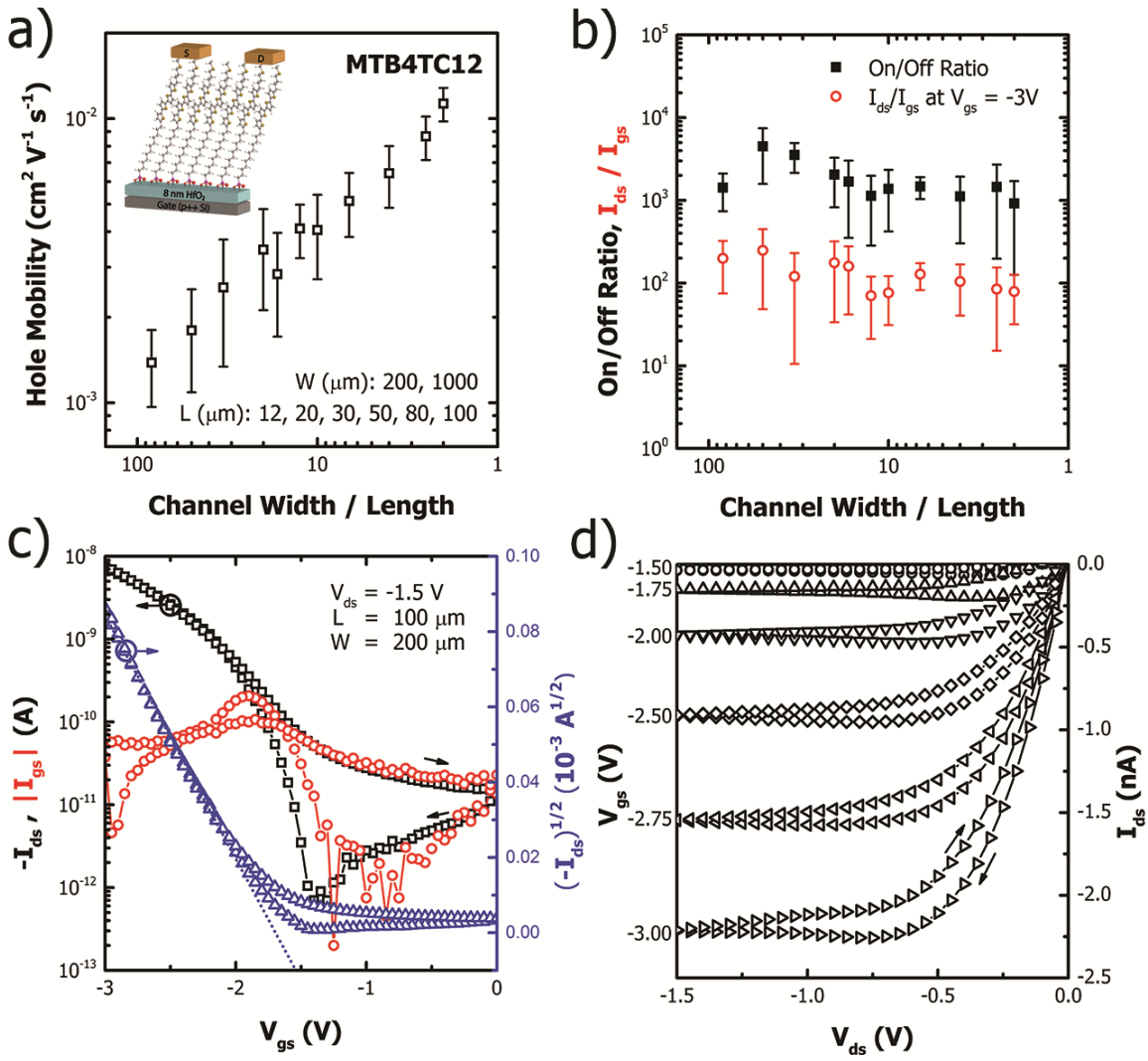

Figure 5.16. Electrical characterization of low voltage MTB4TC12 based SAMFETs. a) Hole mobility with respect to ratio of channel width/length for low voltage SAMFET with MTB4TC12 SAM semiconductor with insert showing device architecture; Device assembled under best conditions with SAM assembly at 120 °C and device annealed at 120 °C for 10 hours after gold electrode deposition; b) Transistor performance parameters indicating on/off current ratio, and difference between drain-source current and gate-source leakage current at -3 V; Representative transfer (c) and output (d) characteristic transistor curves for a device with a channel width and length of 200 μm and 100 μm operated at V_{ds} of -1.5 V. Reprinted with permission from [57]. Copyright 2015, Wiley-VCH Verlag GmbH & Co. KGaA

5.4 CONCLUSION

In summary, high performance low operating voltage SAMFETs have been fabricated through the rational design of a functional SAM head group and processing optimization. The methylthiobutyl terminal group of the quaterthiophene based SAM semiconductors has enabled efficient electrical contact to Au electrodes while maintaining SAMFET thermal stability. Annealing has been shown to further enhance the coordinate bond between SAM and electrode to enable over two orders of magnitude increase in charge carrier mobility. Additionally, through the use of heated immersion assembly, SAM density has been increased by approximately 30% resulting in another order of magnitude higher charge carrier mobility. Low voltage SAMFETs utilizing hybrid HfO_2 sol-gel dielectric were then assembled under optimized processing conditions to achieve a peak hole-mobility of 0.015 $cm^2 V^{-1} s^{-1}$. These results show the importance of terminal group and processing for SAMFETs and should be generally applicable to other SAM semiconductor systems.

BIBLIOGRAPHY

[1] C. Wang, H. Dong, W. Hu, Y. Liu, D. Zhu, Semiconducting π-Conjugated Systems in Field-Effect Transistors: A Material Odyssey of Organic Electronics, *Chemical Reviews*, 112, 2208, **2012**.

[2] A. R. Murphy, J. M. J. Fréchet, Organic Semiconducting Oligomers for Use in Thin Film Transistors, *Chemical Reviews*, 107, 1066, **2007**.

[3] J. Zaumseil, H. Sirringhaus, Electron and Ambipolar Transport in Organic Field-Effect Transistors, *Chemical Reviews*, 107, 1296, **2007**.

[4] J. E. Anthony, A. Facchetti, M. Heeney, S. R. Marder, X. Zhan, n-Type Organic Semiconductors in Organic Electronics, *Advanced Materials*, 22, 3876, **2010**.

[5] D. K. Hwang, C. Fuentes-Hernandez, J. Kim, W. J. Potscavage, S.-J. Kim, B. Kippelen, Top-Gate Organic Field-Effect Transistors with High Environmental and Operational Stability, *Advanced Materials*, 23, 1293, **2011**.

[6] D. Gupta, M. Katiyar, D. Gupta, An analysis of the difference in behavior of top and bottom contact organic thin film transistors using device simulation, *Organic Electronics*, 10, 775, **2009**.

[7] I. G. Hill, Numerical simulations of contact resistance in organic thin-film transistors, *Applied Physics Letters*, 87, 163505, **2005**.

[8] P. V. Necliudov, M. S. Shur, D. J. Gundlach, T. N. Jackson, Modeling of organic thin film transistors of different designs, *Journal of Applied Physics*, 88, 6594, **2000**.

[9] C. R. Newman, C. D. Frisbie, D. A. da Silva Filho, J.-L. Brédas, P. C. Ewbank, K. R. Mann, Introduction to Organic Thin Film Transistors and Design of n-Channel Organic Semiconductors, *Chemistry of Materials*, 16, 4436, **2004**.

[10] A. Tsumura, H. Koezuka, T. Ando, Macromolecular electronic device: Field-effect transistor with a polythiophene thin film, *Applied Physics Letters*, 49, 1210, **1986**.

[11] M. Yamagishi, J. Takeya, Y. Tominari, Y. Nakazawa, T. Kuroda, S. Ikehata, M. Uno, T. Nishikawa, T. Kawase, High-mobility double-gate organic single-crystal transistors with organic crystal gate insulators, *Applied Physics Letters*, 90, 182117, **2007**.

[12] H. Minemawari, T. Yamada, H. Matsui, J. y. Tsutsumi, S. Haas, R. Chiba, R. Kumai, T. Hasegawa, Inkjet printing of single-crystal films, *Nature*, 475, 364, **2011**.

[13] H. Dong, X. Fu, J. Liu, Z. Wang, W. Hu, 25th Anniversary Article: Key Points for High-Mobility Organic Field-Effect Transistors, *Advanced Materials*, 25, 6158, **2013**.

[14] Y. Zhao, Y. Guo, Y. Liu, 25th Anniversary Article: Recent Advances in n-Type and Ambipolar Organic Field-Effect Transistors, *Advanced Materials*, 25, 5372, **2013**.

[15] H. Sirringhaus, 25th Anniversary Article: Organic Field-Effect Transistors: The Path Beyond Amorphous Silicon, *Advanced Materials*, 26, 1319, **2014**.

[16] J. Mei, Y. Diao, A. L. Appleton, L. Fang, Z. Bao, Integrated Materials Design of Organic Semiconductors for Field-Effect Transistors, *Journal of the American Chemical Society*, 135, 6724, **2013**.

[17] G. Malliaras, R. Friend, An organic electronics primer, *Physics Today*, 58, 53, **2005**.

[18] V. Coropceanu, J. Cornil, D. A. da Silva Filho, Y. Olivier, R. Silbey, J.-L. Brédas, Charge Transport in Organic Semiconductors, *Chemical Reviews*, 107, 926, **2007**.

[19] J. L. Bredas, G. B. Street, Polarons, bipolarons, and solitons in conducting polymers, *Accounts of Chemical Research*, 18, 309, **1985**.

[20] A. J. Heeger, S. Kivelson, J. R. Schrieffer, W. P. Su, Solitons in conducting polymers, *Reviews of Modern Physics*, 60, 781, **1988**.

[21] S. M. Sze, K. K. Ng, *Physics of semiconductor devices*, John wiley & sons, 2006.

[22] I. Levine, S. M. Weber, Y. Feldman, T. Bendikov, H. Cohen, D. Cahen, A. Vilan, Molecular Length, Monolayer Density, and Charge Transport: Lessons from Al–AlOx/Alkyl–Phosphonate/Hg Junctions, *Langmuir*, 28, 404, **2012**.

[23] E. L. Hanson, J. Schwartz, B. Nickel, N. Koch, M. F. Danisman, Bonding Self-Assembled, Compact Organophosphonate Monolayers to the Native Oxide Surface of Silicon, *Journal of the American Chemical Society*, 125, 16074, **2003**.

[24] G. G. Ting, O. Acton, H. Ma, J. W. Ka, A. K. Y. Jen, Study on the Formation of Self-Assembled Monolayers on Sol−Gel Processed Hafnium Oxide as Dielectric Layers, *Langmuir*, 25, 2140, **2009**.

[25] H. Sellers, A. Ulman, Y. Shnidman, J. E. Eilers, Structure and binding of alkanethiolates on gold and silver surfaces: implications for self-assembled monolayers, *Journal of the American Chemical Society*, 115, 9389, **1993**.

[26] A. Ulman, Formation and structure of self-assembled monolayers, *Chemical reviews*, 96, 1533, **1996**.

[27] L. H. Dubois, R. G. Nuzzo, Synthesis, structure, and properties of model organic surfaces, *Annual review of physical chemistry*, 43, 437, **1992**.

[28] P. E. Laibinis, G. M. Whitesides, D. L. Allara, Y. T. Tao, A. N. Parikh, R. G. Nuzzo, Comparison of the structures and wetting properties of self-assembled monolayers of n-

alkanethiols on the coinage metal surfaces, copper, silver, and gold*, Journal of the American Chemical Society*, 113, 7152, **1991**.

[29] P. E. Laibinis, G. M. Whitesides, Self-assembled monolayers of n-alkanethiolates on copper are barrier films that protect the metal against oxidation by air*, Journal of the American Chemical Society*, 114, 9022, **1992**.

[30] K. Shimazu, Y. Sato, I. Yagi, K. Uosaki, Packing State and Stability of Self-Assembled Monolayers of 11-Ferrocenyl-1-undecanethiol on Platinum Electrodes*, Bulletin of the Chemical Society of Japan*, 67, 863, **1994**.

[31] A. Demoz, D. J. Harrison, Characterization and extremely low defect density hexadecanethiol monolayers on mercury surfaces*, Langmuir*, 9, 1046, **1993**.

[32] M. Volmer, M. Stratmann, H. Viefhaus, Electrochemical and electron spectroscopic investigations of iron surfaces modified with thiols*, Surface and Interface Analysis*, 16, 278, **1990**.

[33] S. P. Pujari, L. Scheres, A. T. M. Marcelis, H. Zuilhof, Covalent Surface Modification of Oxide Surfaces*, Angewandte Chemie International Edition*, 53, 6322, **2014**.

[34] P. H. Mutin, G. Guerrero, A. Vioux, Hybrid materials from organophosphorus coupling molecules*, Journal of Materials Chemistry*, 15, 3761, **2005**.

[35] R. R. Rye, G. C. Nelson, M. T. Dugger, Mechanistic Aspects of Alkylchlorosilane Coupling Reactions*, Langmuir*, 13, 2965, **1997**.

[36] M. Giza, P. Thissen, G. Grundmeier, Adsorption Kinetics of Organophosphonic Acids on Plasma-Modified Oxide-Covered Aluminum Surfaces*, Langmuir*, 24, 8688, **2008**.

[37] S. Ong, X. Zhao, K. B. Eisenthal, Polarization of water molecules at a charged interface: second harmonic studies of the silica/water interface*, Chemical Physics Letters*, 191, 327, **1992**.

[38] F. J. M. Hoeben, P. Jonkheijm, E. W. Meijer, A. P. H. J. Schenning, About Supramolecular Assemblies of π-Conjugated Systems*, Chemical Reviews*, 105, 1491, **2005**.

[39] F. Schreiber, Structure and growth of self-assembling monolayers*, Progress in Surface Science*, 65, 151, **2000**.

[40] P. J. Hotchkiss, S. C. Jones, S. A. Paniagua, A. Sharma, B. Kippelen, N. R. Armstrong, S. R. Marder, The Modification of Indium Tin Oxide with Phosphonic Acids: Mechanism of Binding, Tuning of Surface Properties, and Potential for Use in Organic Electronic Applications*, Accounts of Chemical Research*, 45, 337, **2012**.

[41] B. O. Acton, G. G. Ting, P. J. Shamberger, F. S. Ohuchi, H. Ma, A. K. Y. Jen, Dielectric Surface-Controlled Low-Voltage Organic Transistors via n-Alkyl Phosphonic Acid Self-

Assembled Monolayers on High-k Metal Oxide*, ACS Applied Materials & Interfaces*, 2, 511, **2010**.

[42] A. Jedaa, M. Burkhardt, U. Zschieschang, H. Klauk, D. Habich, G. Schmid, M. Halik, The impact of self-assembled monolayer thickness in hybrid gate dielectrics for organic thin-film transistors*, Organic Electronics*, 10, 1442, **2009**.

[43] Y. Ito, A. A. Virkar, S. Mannsfeld, J. H. Oh, M. Toney, J. Locklin, Z. Bao, Crystalline Ultrasmooth Self-Assembled Monolayers of Alkylsilanes for Organic Field-Effect Transistors*, Journal of the American Chemical Society*, 131, 9396, **2009**.

[44] N. Cernetic, O. Acton, T. Weidner, D. O. Hutchins, J. E. Baio, H. Ma, A. K. Y. Jen, Bottom-contact small-molecule n-type organic field effect transistors achieved via simultaneous modification of electrode and dielectric surfaces*, Organic Electronics*, 13, 3226, **2012**.

[45] O. Acton, M. Dubey, T. Weidner, K. M. O'Malley, T.-W. Kim, G. G. Ting, D. Hutchins, J. E. Baio, T. C. Lovejoy, A. H. Gage, D. G. Castner, H. Ma, A. K. Y. Jen, Simultaneous Modification of Bottom-Contact Electrode and Dielectric Surfaces for Organic Thin-Film Transistors Through Single-Component Spin-Cast Monolayers*, Advanced Functional Materials*, 21, 1476, **2011**.

[46] O. Acton, D. Hutchins, L. Árnadóttir, T. Weidner, N. Cernetic, G. G. Ting, T.-W. Kim, D. G. Castner, H. Ma, A. K. Y. Jen, Spin-Cast and Patterned Organophosphonate Self-Assembled Monolayer Dielectrics on Metal-Oxide-Activated Si*, Advanced Materials*, 23, 1899, **2011**.

[47] M. Novak, T. Schmaltz, H. Faber, M. Halik, Influence of self-assembled monolayer dielectrics on the morphology and performance of α,ω-dihexylquaterthiophene in thin film transistors*, Applied Physics Letters*, 98, 093302, **2011**.

[48] B. de Boer, A. Hadipour, M. M. Mandoc, T. van Woudenbergh, P. W. M. Blom, Tuning of Metal Work Functions with Self-Assembled Monolayers*, Advanced Materials*, 17, 621, **2005**.

[49] J. Park, W. H. Lee, S. Huh, S. H. Sim, S. B. Kim, K. Cho, B. H. Hong, K. S. Kim, Work-Function Engineering of Graphene Electrodes by Self-Assembled Monolayers for High-Performance Organic Field-Effect Transistors*, The Journal of Physical Chemistry Letters*, 2, 841, **2011**.

[50] N. Cernetic, S. Wu, J. A. Davies, B. W. Krueger, D. O. Hutchins, X. Xu, H. Ma, A. K. Y. Jen, Systematic Doping Control of CVD Graphene Transistors with Functionalized Aromatic Self-Assembled Monolayers*, Advanced Functional Materials*, 24, 3464, **2014**.

[51] U. Zschieschang, F. Ante, M. Schlörholz, M. Schmidt, K. Kern, H. Klauk, Mixed Self-Assembled Monolayer Gate Dielectrics for Continuous Threshold Voltage Control in Organic Transistors and Circuits*, Advanced Materials*, 22, 4489, **2010**.

[52] Y. Chung, E. Verploegen, A. Vailionis, Y. Sun, Y. Nishi, B. Murmann, Z. Bao, Controlling Electric Dipoles in Nanodielectrics and Its Applications for Enabling Air-Stable n-Channel Organic Transistors, *Nano Letters*, 11, 1161, **2011**.

[53] F. Gholamrezaie, A.-M. Andringa, W. S. C. Roelofs, A. Neuhold, M. Kemerink, P. W. M. Blom, D. M. de Leeuw, Charge Trapping by Self-Assembled Monolayers as the Origin of the Threshold Voltage Shift in Organic Field-Effect Transistors, *Small*, 8, 241, **2012**.

[54] F. Dinelli, M. Murgia, P. Levy, M. Cavallini, F. Biscarini, D. M. de Leeuw, Spatially Correlated Charge Transport in Organic Thin Film Transistors, *Physical Review Letters*, 92, 116802, **2004**.

[55] A. Shehu, S. D. Quiroga, P. D'Angelo, C. Albonetti, F. Borgatti, M. Murgia, A. Scorzoni, P. Stoliar, F. Biscarini, Layered Distribution of Charge Carriers in Organic Thin Film Transistors, *Physical Review Letters*, 104, 246602, **2010**.

[56] E. C. P. Smits, S. G. J. Mathijssen, P. A. van Hal, S. Setayesh, T. C. T. Geuns, K. A. H. A. Mutsaers, E. Cantatore, H. J. Wondergem, O. Werzer, R. Resel, M. Kemerink, S. Kirchmeyer, A. M. Muzafarov, S. A. Ponomarenko, B. de Boer, P. W. M. Blom, D. M. de Leeuw, Bottom-up organic integrated circuits, *Nature*, 455, 956, **2008**.

[57] N. Cernetic, T. Weidner, J. E. Baio, H. Lu, H. Ma, A. K. Y. Jen, Enhanced Performance of Self-Assembled Monolayer Field-Effect Transistors with Top-Contact Geometry through Molecular Tailoring, Heated Assembly, and Thermal Annealing, *Advanced Functional Materials*, 25, 5376, **2015**.

[58] M. Novak, A. Ebel, T. Meyer-Friedrichsen, A. Jedaa, B. F. Vieweg, G. Yang, K. Voitchovsky, F. Stellacci, E. Spiecker, A. Hirsch, M. Halik, Low-Voltage p- and n-Type Organic Self-Assembled Monolayer Field Effect Transistors, *Nano Letters*, 11, 156, **2011**.

[59] C. M. Jäger, T. Schmaltz, M. Novak, A. Khassanov, A. Vorobiev, M. Hennemann, A. Krause, H. Dietrich, D. Zahn, A. Hirsch, M. Halik, T. Clark, Improving the Charge Transport in Self-Assembled Monolayer Field-Effect Transistors: From Theory to Devices, *Journal of the American Chemical Society*, 135, 4893, **2013**.

[60] T. Schmaltz, A. Khassanov, H.-G. Steinruck, A. Magerl, A. Hirsch, M. Halik, Tuning the molecular order of C60-based self-assembled monolayers in field-effect transistors, *Nanoscale*, 6, 13022, **2014**.

[61] A. Ringk, X. Li, F. Gholamrezaie, E. C. P. Smits, A. Neuhold, A. Moser, C. Van der Marel, G. H. Gelinck, R. Resel, D. M. de Leeuw, P. Strohriegl, N-Type Self-Assembled Monolayer Field-Effect Transistors and Complementary Inverters, *Advanced Functional Materials*, 23, 2016, **2013**.

[62] A. Ringk, W. S. Christian Roelofs, E. C. P. Smits, C. van der Marel, I. Salzmann, A. Neuhold, G. H. Gelinck, R. Resel, D. M. de Leeuw, P. Strohriegl, n-Type self-assembled

monolayer field-effect transistors for flexible organic electronics, *Organic Electronics*, 14, 1297, **2013**.

[63] T. Schmaltz, A. Y. Amin, A. Khassanov, T. Meyer-Friedrichsen, H.-G. Steinrück, A. Magerl, J. J. Segura, K. Voitchovsky, F. Stellacci, M. Halik, Low-Voltage Self-Assembled Monolayer Field-Effect Transistors on Flexible Substrates, *Advanced Materials*, 25, 4511, **2013**.

[64] A. V. S. Parry, K. Lu, D. J. Tate, B. Urasinska-Wojcik, D. Caras-Quintero, L. A. Majewski, M. L. Turner, Trichlorosilanes as Anchoring Groups for Phenylene-Thiophene Molecular Monolayer Field Effect Transistors, *Advanced Functional Materials*, 24, 6677, **2014**.

[65] C. Messerschmidt, D. K. Schwartz, Growth Mechanisms of Octadecylphosphonic Acid Self-Assembled Monolayers on Sapphire (Corundum): Evidence for a Quasi-equilibrium Triple Point, *Langmuir*, 17, 462, **2001**.

[66] D. O. Hutchins, O. Acton, T. Weidner, N. Cernetic, J. E. Baio, D. G. Castner, H. Ma, A. K. Y. Jen, Solid-state densification of spun-cast self-assembled monolayers for use in ultra-thin hybrid dielectrics, *Applied Surface Science*, 261, 908, **2012**.

[67] M. Pfeiffer-Laplaud, D. Costa, F. Tielens, M.-P. Gaigeot, M. Sulpizi, Bimodal Acidity at the Amorphous Silica/Water Interface, *The Journal of Physical Chemistry C*, 119, 27354, **2015**.

[68] K. Leung, I. M. B. Nielsen, L. J. Criscenti, Elucidating the Bimodal Acid−Base Behavior of the Water−Silica Interface from First Principles, *Journal of the American Chemical Society*, 131, 18358, **2009**.

[69] M. Sulpizi, M.-P. Gaigeot, M. Sprik, The Silica–Water Interface: How the Silanols Determine the Surface Acidity and Modulate the Water Properties, *Journal of Chemical Theory and Computation*, 8, 1037, **2012**.

[70] A. Vega, P. Thissen, Y. J. Chabal, Environment-Controlled Tethering by Aggregation and Growth of Phosphonic Acid Monolayers on Silicon Oxide, *Langmuir*, 28, 8046, **2012**.

[71] H.-Y. Nie, M. J. Walzak, N. S. McIntyre, Delivering Octadecylphosphonic Acid Self-Assembled Monolayers on a Si Wafer and Other Oxide Surfaces, *The Journal of Physical Chemistry B*, 110, 21101, **2006**.

[72] X. Chen, E. Luais, N. Darwish, S. Ciampi, P. Thordarson, J. J. Gooding, Studies on the Effect of Solvents on Self-Assembled Monolayers Formed from Organophosphonic Acids on Indium Tin Oxide, *Langmuir*, 28, 9487, **2012**.

[73] G. Gelinck, P. Heremans, K. Nomoto, T. D. Anthopoulos, Organic Transistors in Optical Displays and Microelectronic Applications, *Advanced Materials*, 22, 3778, **2010**.

[74] G. H. Gelinck, H. E. A. Huitema, E. van Veenendaal, E. Cantatore, L. Schrijnemakers, J. B. P. H. van der Putten, T. C. T. Geuns, M. Beenhakkers, J. B. Giesbers, B.-H. Huisman, E. J. Meijer, E. M. Benito, F. J. Touwslager, A. W. Marsman, B. J. E. van Rens, D. M. de Leeuw, Flexible active-matrix displays and shift registers based on solution-processed organic transistors, *Nat Mater*, 3, 106, **2004**.

[75] M. A. McCarthy, B. Liu, E. P. Donoghue, I. Kravchenko, D. Y. Kim, F. So, A. G. Rinzler, Low-Voltage, Low-Power, Organic Light-Emitting Transistors for Active Matrix Displays, *Science*, 332, 570, **2011**.

[76] P. Lin, F. Yan, Organic Thin-Film Transistors for Chemical and Biological Sensing, *Advanced Materials*, 24, 34, **2012**.

[77] M. D. Angione, R. Pilolli, S. Cotrone, M. Magliulo, A. Mallardi, G. Palazzo, L. Sabbatini, D. Fine, A. Dodabalapur, N. Cioffi, L. Torsi, Carbon based materials for electronic bio-sensing, *Materials Today*, 14, 424, **2011**.

[78] K. Myny, S. Steudel, S. Smout, P. Vicca, F. Furthner, B. van der Putten, A. K. Tripathi, G. H. Gelinck, J. Genoe, W. Dehaene, P. Heremans, Organic RFID transponder chip with data rate compatible with electronic product coding, *Organic Electronics*, 11, 1176, **2010**.

[79] T. Sekitani, T. Someya, Stretchable, Large-area Organic Electronics, *Advanced Materials*, 22, 2228, **2010**.

[80] J. E. Anthony, Functionalized Acenes and Heteroacenes for Organic Electronics, *Chemical Reviews*, 106, 5028, **2006**.

[81] H. Usta, A. Facchetti, T. J. Marks, n-Channel Semiconductor Materials Design for Organic Complementary Circuits, *Accounts of Chemical Research*, 44, 501, **2011**.

[82] J. Veres, S. Ogier, G. Lloyd, D. de Leeuw, Gate Insulators in Organic Field-Effect Transistors, *Chemistry of Materials*, 16, 4543, **2004**.

[83] A. Facchetti, M. H. Yoon, T. J. Marks, Gate Dielectrics for Organic Field-Effect Transistors: New Opportunities for Organic Electronics, *Advanced Materials*, 17, 1705, **2005**.

[84] R. P. Ortiz, A. Facchetti, T. J. Marks, High-k Organic, Inorganic, and Hybrid Dielectrics for Low-Voltage Organic Field-Effect Transistors, *Chemical Reviews*, 110, 205, **2010**.

[85] D. Natali, M. Caironi, Charge Injection in Solution-Processed Organic Field-Effect Transistors: Physics, Models and Characterization Methods, *Advanced Materials*, 24, 1357, **2012**.

[86] M.-H. Yoon, C. Kim, A. Facchetti, T. J. Marks, Gate Dielectric Chemical Structure−Organic Field-Effect Transistor Performance Correlations for Electron, Hole, and Ambipolar Organic Semiconductors, *Journal of the American Chemical Society*, 128, 12851, **2006**.

[87] I. Kymissis, C. D. Dimitrakopoulos, S. Purushothaman, High-performance bottom electrode organic thin-film transistors, *Electron Devices, IEEE Transactions on*, 48, 1060, **2001**.

[88] K. Asadi, Y. Wu, F. Gholamrezaie, P. Rudolf, P. W. M. Blom, Single-Layer Pentacene Field-Effect Transistors Using Electrodes Modified With Self-assembled Monolayers, *Advanced Materials*, 21, 4109, **2009**.

[89] J. Youn, G. R. Dholakia, H. Huang, J. W. Hennek, A. Facchetti, T. J. Marks, Influence of Thiol Self-Assembled Monolayer Processing on Bottom-Contact Thin-Film Transistors Based on n-Type Organic Semiconductors, *Advanced Functional Materials*, 22, 1856, **2012**.

[90] X. Cheng, Y.-Y. Noh, J. Wang, M. Tello, J. Frisch, R.-P. Blum, A. Vollmer, J. P. Rabe, N. Koch, H. Sirringhaus, Controlling Electron and Hole Charge Injection in Ambipolar Organic Field-Effect Transistors by Self-Assembled Monolayers, *Advanced Functional Materials*, 19, 2407, **2009**.

[91] K. Fukuda, T. Hamamoto, T. Yokota, T. Sekitani, U. Zschieschang, H. Klauk, T. Someya, Effects of the alkyl chain length in phosphonic acid self-assembled monolayer gate dielectrics on the performance and stability of low-voltage organic thin-film transistors, *Applied Physics Letters*, 95, 203301, **2009**.

[92] J.-P. Hong, A.-Y. Park, S. Lee, J. Kang, N. Shin, D. Y. Yoon, Tuning of Ag work functions by self-assembled monolayers of aromatic thiols for an efficient hole injection for solution processed triisopropylsilylethynyl pentacene organic thin film transistors, *Applied Physics Letters*, 92, 143311, **2008**.

[93] L.-L. Chua, J. Zaumseil, J.-F. Chang, E. C.-W. Ou, P. K.-H. Ho, H. Sirringhaus, R. H. Friend, General observation of n-type field-effect behaviour in organic semiconductors, *Nature*, 434, 194, **2005**.

[94] I. Hulea, S. Fratini, H. Xie, C. Mulder, N. Iossad, G. Rastelli, S. Ciuchi, A. Morpurgo, Tunable Fröhlich polarons in organic single-crystal transistors, *Nature Materials*, 5, 982, **2006**.

[95] Q. J. Cai, M. B. Chan-Park, Z. S. Lu, C. M. Li, B. S. Ong, Bottom-Contact Poly(3,3‴-didodecylquaterthiophene) Thin-Film Transistors with Gold Source-Drain Electrodes Modified by Alkanethiol Monolayers, *Langmuir*, 24, 11889, **2008**.

[96] J. P. Folkers, C. B. Gorman, P. E. Laibinis, S. Buchholz, G. M. Whitesides, R. G. Nuzzo, Self-Assembled Monolayers of Long-Chain Hydroxamic Acids on the Native Oxide of Metals, *Langmuir*, 11, 813, **1995**.

[97] J. McElwee, R. Helmy, A. Y. Fadeev, Thermal stability of organic monolayers chemically grafted to minerals, *Journal of Colloid and Interface Science*, 285, 551, **2005**.

[98] V. M. Kaganer, H. Möhwald, P. Dutta, Structure and phase transitions in Langmuir monolayers, *Reviews of Modern Physics*, 71, 779, **1999**.

[99] M. Halik, H. Klauk, U. Zschieschang, G. Schmid, C. Dehm, M. Schütz, S. Maisch, F. Effenberger, M. Brunnbauer, F. Stellacci, Low-voltage organic transistors with an amorphous molecular gate dielectric, *Nature*, 431, 963, **2004**.

[100] J. Stöhr, *NEXAFS spectroscopy*, Vol. 25, Springer Science & Business Media, 2013.

[101] A. C. Liu, J. Stöhr, C. M. Friend, R. J. Madix, A critical interpretation of the near-edge X-ray absorption fine structure of chemisorbed benzene, *Surface Science*, 235, 107, **1990**.

[102] J. A. Horsley, J. Stöhr, A. P. Hitchcock, D. C. Newbury, A. L. Johnson, F. Sette, Resonances in the K shell excitation spectra of benzene and pyridine: Gas phase, solid, and chemisorbed states, *The Journal of Chemical Physics*, 83, 6099, **1985**.

[103] D. A. Outka, J. Stöhr, R. J. Madix, H. H. Rotermund, B. Hermsmeier, J. Solomon, NEXAFS studies of complex alcohols and carboxylic acids on the Si(111)(7×7) surface, *Surface Science*, 185, 53, **1987**.

[104] J. Stöhr, D. A. Outka, Determination of molecular orientations on surfaces from the angular dependence of near-edge x-ray-absorption fine-structure spectra, *Physical Review B*, 36, 7891, **1987**.

[105] S. D. Wang, T. Minari, T. Miyadera, Y. Aoyagi, K. Tsukagoshi, Bias stress instability in pentacene thin film transistors: Contact resistance change and channel threshold voltage shift, *Applied Physics Letters*, 92, 063305, **2008**.

[106] S. Chang-Hoon, F. Maruoka, R. Hattori, Structural Analysis on Organic Thin-Film Transistor With Device Simulation, *Electron Devices, IEEE Transactions on*, 57, 195, **2010**.

[107] S. Cho, J. H. Seo, K. Lee, A. J. Heeger, Enhanced Performance of Fullerene n-Channel Field-Effect Transistors with Titanium Sub-Oxide Injection Layer, *Advanced Functional Materials*, 19, 1459, **2009**.

[108] C. Bock, D. V. Pham, U. Kunze, D. Käfer, G. Witte, C. Wöll, Improved morphology and charge carrier injection in pentacene field-effect transistors with thiol-treated electrodes, *Journal of Applied Physics*, 100, 114517, **2006**.

[109] N. Cernetic, D. O. Hutchins, H. Ma, A. K.-Y. Jen, Influence of self-assembled monolayer binding group on graphene transistors, *Applied Physics Letters*, 106, 021603, **2015**.

[110] K. S. Novoselov, A. K. Geim, S. V. Morozov, D. Jiang, M. I. Katsnelson, I. V. Grigorieva, S. V. Dubonos, A. A. Firsov, Two-dimensional gas of massless Dirac fermions in graphene, *Nature*, 438, 197, **2005**.

[111] A. H. Castro Neto, F. Guinea, N. M. R. Peres, K. S. Novoselov, A. K. Geim, The electronic properties of graphene, *Reviews of Modern Physics*, 81, 109, **2009**.

[112] S. V. Morozov, K. S. Novoselov, M. I. Katsnelson, F. Schedin, D. C. Elias, J. A. Jaszczak, A. K. Geim, Giant Intrinsic Carrier Mobilities in Graphene and Its Bilayer, *Physical Review Letters*, 100, 016602, **2008**.

[113] K. I. Bolotin, K. J. Sikes, Z. Jiang, M. Klima, G. Fudenberg, J. Hone, P. Kim, H. L. Stormer, Ultrahigh electron mobility in suspended graphene, *Solid State Communications*, 146, 351, **2008**.

[114] R. A. Nistor, M. A. Kuroda, A. A. Maarouf, G. J. Martyna, Doping of adsorbed graphene from defects and impurities in SiO_2 substrates, *Physical Review B*, 86, 041409, **2012**.

[115] T. O. Wehling, M. I. Katsnelson, A. I. Lichtenstein, Adsorbates on graphene: Impurity states and electron scattering, *Chemical Physics Letters*, 476, 125, **2009**.

[116] H. Liu, Y. Liu, D. Zhu, Chemical doping of graphene, *Journal of Materials Chemistry*, 21, 3335, **2011**.

[117] Y. Xue, B. Wu, L. Jiang, Y. Guo, L. Huang, J. Chen, J. Tan, D. Geng, B. Luo, W. Hu, G. Yu, Y. Liu, Low Temperature Growth of Highly Nitrogen-Doped Single Crystal Graphene Arrays by Chemical Vapor Deposition, *Journal of the American Chemical Society*, 134, 11060, **2012**.

[118] Y. Shi, X. Dong, P. Chen, J. Wang, L.-J. Li, Effective doping of single-layer graphene from underlying SiO_2 substrates, *Physical Review B*, 79, 115402, **2009**.

[119] G. Giovannetti, P. A. Khomyakov, G. Brocks, V. M. Karpan, J. van den Brink, P. J. Kelly, Doping Graphene with Metal Contacts, *Physical Review Letters*, 101, 026803, **2008**.

[120] K. Yokota, K. Takai, T. Enoki, Carrier Control of Graphene Driven by the Proximity Effect of Functionalized Self-assembled Monolayers, *Nano Letters*, 11, 3669, **2011**.

[121] Z. Yan, Z. Sun, W. Lu, J. Yao, Y. Zhu, J. M. Tour, Controlled Modulation of Electronic Properties of Graphene by Self-Assembled Monolayers on SiO2 Substrates, *ACS Nano*, 5, 1535, **2011**.

[122] W. H. Lee, J. Park, Y. Kim, K. S. Kim, B. H. Hong, K. Cho, Control of Graphene Field-Effect Transistors by Interfacial Hydrophobic Self-Assembled Monolayers, *Advanced Materials*, 23, 3460, **2011**.

[123] D. Sun, G. Aivazian, A. M. Jones, J. S. Ross, W. Yao, D. Cobden, X. Xu, Ultrafast hot-carrier-dominated photocurrent in graphene, *Nature nanotechnology*, 7, 114, **2012**.

[124] R. J. Nemanich, S. A. Solin, First- and second-order Raman scattering from finite-size crystals of graphite, *Physical Review B*, 20, 392, **1979**.

[125] L. G. Cançado, A. Reina, J. Kong, M. S. Dresselhaus, Geometrical approach for the study of **G'** band in the Raman spectrum of monolayer graphene, bilayer graphene, and bulk graphite*, Physical Review B*, 77, 245408, **2008**.

[126] H. Xu, Y. Chen, J. Zhang, H. Zhang, Investigating the Mechanism of Hysteresis Effect in Graphene Electrical Field Device Fabricated on SiO2 Substrates using Raman Spectroscopy*, Small*, 8, 2833, **2012**.

[127] F. Schwierz, Graphene transistors*, Nat Nano*, 5, 487, **2010**.

[128] D. O. Hutchins, T. Weidner, J. Baio, B. Polishak, O. Acton, N. Cernetic, H. Ma, A. K. Y. Jen, Effects of self-assembled monolayer structural order, surface homogeneity and surface energy on pentacene morphology and thin film transistor device performance*, Journal of Materials Chemistry C*, 1, 101, **2013**.

[129] K. Novoselov, A. K. Geim, S. Morozov, D. Jiang, M. Katsnelson, I. Grigorieva, S. Dubonos, A. Firsov, Two-dimensional gas of massless Dirac fermions in graphene*, nature*, 438, 197, **2005**.

[130] P. R. Wallace, The Band Theory of Graphite*, Physical Review*, 71, 622, **1947**.

[131] X. Liang, B. A. Sperling, I. Calizo, G. Cheng, C. A. Hacker, Q. Zhang, Y. Obeng, K. Yan, H. Peng, Q. Li, X. Zhu, H. Yuan, A. R. Hight Walker, Z. Liu, L.-m. Peng, C. A. Richter, Toward Clean and Crackless Transfer of Graphene*, ACS Nano*, 5, 9144, **2011**.

[132] A. S. Mayorov, R. V. Gorbachev, S. V. Morozov, L. Britnell, R. Jalil, L. A. Ponomarenko, P. Blake, K. S. Novoselov, K. Watanabe, T. Taniguchi, A. K. Geim, Micrometer-Scale Ballistic Transport in Encapsulated Graphene at Room Temperature*, Nano Letters*, 11, 2396, **2011**.

[133] R. A. Nistor, M. A. Kuroda, A. A. Maarouf, G. J. Martyna, Doping of adsorbed graphene from defects and impurities in SiO${}_{2}$ substrates*, Physical Review B*, 86, 041409, **2012**.

[134] K. C. Kwon, K. S. Choi, S. Y. Kim, Increased Work Function in Few-Layer Graphene Sheets via Metal Chloride Doping*, Advanced Functional Materials*, 22, 4724, **2012**.

[135] P. Wei, N. Liu, H. R. Lee, E. Adijanto, L. Ci, B. D. Naab, J. Q. Zhong, J. Park, W. Chen, Y. Cui, Z. Bao, Tuning the Dirac Point in CVD-Grown Graphene through Solution Processed n-Type Doping with 2-(2-Methoxyphenyl)-1,3-dimethyl-2,3-dihydro-1H-benzoimidazole*, Nano Letters*, 13, 1890, **2013**.

[136] H. H. Kim, J. W. Yang, S. B. Jo, B. Kang, S. K. Lee, H. Bong, G. Lee, K. S. Kim, K. Cho, Substrate-Induced Solvent Intercalation for Stable Graphene Doping*, ACS Nano*, 7, 1155, **2013**.

[137] D. Wei, Y. Liu, Y. Wang, H. Zhang, L. Huang, G. Yu, Synthesis of N-Doped Graphene by Chemical Vapor Deposition and Its Electrical Properties*, Nano Letters*, 9, 1752, **2009**.

[138] Y.-B. Tang, L.-C. Yin, Y. Yang, X.-H. Bo, Y.-L. Cao, H.-E. Wang, W.-J. Zhang, I. Bello, S.-T. Lee, H.-M. Cheng, C.-S. Lee, Tunable Band Gaps and p-Type Transport Properties of Boron-Doped Graphenes by Controllable Ion Doping Using Reactive Microwave Plasma*, ACS Nano*, 6, 1970, **2012**.

[139] Y.-J. Yu, Y. Zhao, S. Ryu, L. E. Brus, K. S. Kim, P. Kim, Tuning the Graphene Work Function by Electric Field Effect*, Nano Letters*, 9, 3430, **2009**.

[140] Y. Shi, X. Dong, P. Chen, J. Wang, L.-J. Li, Effective doping of single-layer graphene from underlying ${\text{SiO}}_{2}$ substrates*, Physical Review B*, 79, 115402, **2009**.

[141] A. Varykhalov, M. R. Scholz, T. K. Kim, O. Rader, Effect of noble-metal contacts on doping and band gap of graphene*, Physical Review B*, 82, 121101, **2010**.

[142] R. Wang, S. Wang, D. Zhang, Z. Li, Y. Fang, X. Qiu, Control of Carrier Type and Density in Exfoliated Graphene by Interface Engineering*, ACS Nano*, 5, 408, **2011**.

[143] U. Kraft, U. Zschieschang, F. Ante, D. Kalblein, C. Kamella, K. Amsharov, M. Jansen, K. Kern, E. Weber, H. Klauk, Fluoroalkylphosphonic acid self-assembled monolayer gate dielectrics for threshold-voltage control in low-voltage organic thin-film transistors*, Journal of Materials Chemistry*, 20, 6416, **2010**.

[144] A. Jedaa, M. Salinas, C. M. Jäger, T. Clark, A. Ebel, A. Hirsch, M. Halik, Mixed self-assembled monolayer of molecules with dipolar and acceptor character—Influence on hysteresis and threshold voltage in organic thin-film transistors*, Applied Physics Letters*, 100, 063302, **2012**.

[145] M. Salinas, C. M. Jäger, A. Y. Amin, P. O. Dral, T. Meyer-Friedrichsen, A. Hirsch, T. Clark, M. Halik, The Relationship between Threshold Voltage and Dipolar Character of Self-Assembled Monolayers in Organic Thin-Film Transistors*, Journal of the American Chemical Society*, 134, 12648, **2012**.

[146] P. Hohenberg, W. Kohn, Inhomogeneous Electron Gas*, Physical Review*, 136, B864, **1964**.

[147] W. Kohn, L. J. Sham, Self-Consistent Equations Including Exchange and Correlation Effects*, Physical Review*, 140, A1133, **1965**.

[148] M. J. Frisch, G. W. Trucks, H. B. Schlegel, G. E. Scuseria, M. A. Robb, J. R. Cheeseman, G. Scalmani, V. Barone, B. Mennucci, G. A. Petersson, H. Nakatsuji, M. Caricato, X. Li, H. P. Hratchian, A. F. Izmaylov, J. Bloino, G. Zheng, J. L. Sonnenberg, M. Hada, M. Ehara, K. Toyota, R. Fukuda, J. Hasegawa, M. Ishida, T. Nakajima, Y. Honda, O. Kitao, H. Nakai, T. Vreven, J. A. Montgomery Jr., J. E. Peralta, F. Ogliaro, M. J. Bearpark, J. Heyd, E. N. Brothers, K. N. Kudin, V. N. Staroverov, R. Kobayashi, J. Normand, K. Raghavachari, A. P. Rendell, J. C. Burant, S. S. Iyengar, J. Tomasi, M. Cossi, N. Rega, N. J. Millam, M. Klene, J. E. Knox, J. B. Cross, V. Bakken, C. Adamo, J. Jaramillo, R. Gomperts, R. E. Stratmann, O. Yazyev, A. J. Austin, R. Cammi, C. Pomelli, J. W. Ochterski, R. L. Martin, K. Morokuma, V. G. Zakrzewski, G. A. Voth, P. Salvador, J. J.

Dannenberg, S. Dapprich, A. D. Daniels, Ö. Farkas, J. B. Foresman, J. V. Ortiz, J. Cioslowski, D. J. Fox, Gaussian, Inc., Wallingford, CT, USA **2009**.

[149] J. P. Perdew, K. Burke, M. Ernzerhof, Generalized Gradient Approximation Made Simple*, Physical Review Letters*, 77, 3865, **1996**.

[150] A. Schäfer, H. Horn, R. Ahlrichs, Fully optimized contracted Gaussian basis sets for atoms Li to Kr*, The Journal of Chemical Physics*, 97, 2571, **1992**.

[151] K. Eichkorn, O. Treutler, H. Öhm, M. Häser, R. Ahlrichs, Auxiliary basis sets to approximate Coulomb potentials (Chem. Phys. Letters 240 (1995) 283-290)*, Chemical Physics Letters*, 242, 652, **1995**.

[152] F. Tuinstra, J. L. Koenig, Raman Spectrum of Graphite*, The Journal of Chemical Physics*, 53, 1126, **1970**.

[153] A. C. Ferrari, J. C. Meyer, V. Scardaci, C. Casiraghi, M. Lazzeri, F. Mauri, S. Piscanec, D. Jiang, K. S. Novoselov, S. Roth, A. K. Geim, Raman Spectrum of Graphene and Graphene Layers*, Physical Review Letters*, 97, 187401, **2006**.

[154] R. Schlaf, H. Murata, Z. H. Kafafi, Work function measurements on indium tin oxide films*, Journal of Electron Spectroscopy and Related Phenomena*, 120, 149, **2001**.

[155] S. Bae, H. Kim, Y. Lee, X. Xu, J.-S. Park, Y. Zheng, J. Balakrishnan, T. Lei, H. R. Kim, Y. I. Song, Roll-to-roll production of 30-inch graphene films for transparent electrodes*, Nature nanotechnology*, 5, 574, **2010**.

[156] S. E. Koh, K. D. McDonald, D. H. Holt, C. S. Dulcey, J. A. Chaney, P. E. Pehrsson, Phenylphosphonic Acid Functionalization of Indium Tin Oxide: Surface Chemistry and Work Functions*, Langmuir*, 22, 6249, **2006**.

[157] L. Kronik, Y. Shapira, Surface photovoltage phenomena: theory, experiment, and applications*, Surface Science Reports*, 37, 1, **1999**.

[158] M. Gliboff, L. Sang, K. M. Knesting, M. C. Schalnat, A. Mudalige, E. L. Ratcliff, H. Li, A. K. Sigdel, A. J. Giordano, J. J. Berry, D. Nordlund, G. T. Seidler, J.-L. Brédas, S. R. Marder, J. E. Pemberton, D. S. Ginger, Orientation of Phenylphosphonic Acid Self-Assembled Monolayers on a Transparent Conductive Oxide: A Combined NEXAFS, PM-IRRAS, and DFT Study*, Langmuir*, 29, 2166, **2013**.

[159] P. C. Rusu, G. Brocks, Surface Dipoles and Work Functions of Alkylthiolates and Fluorinated Alkylthiolates on Au(111)*, The Journal of Physical Chemistry B*, 110, 22628, **2006**.

[160] X. Ji, K. T. Lee, L. F. Nazar, A highly ordered nanostructured carbon–sulphur cathode for lithium–sulphur batteries*, Nature materials*, 8, 500, **2009**.

[161] B. Zhang, X. Qin, G. R. Li, X. P. Gao, Enhancement of long stability of sulfur cathode by encapsulating sulfur into micropores of carbon spheres, *Energy & Environmental Science*, 3, 1531, **2010**.

[162] Y. Yang, M. T. McDowell, A. Jackson, J. J. Cha, S. S. Hong, Y. Cui, New Nanostructured Li2S/Silicon Rechargeable Battery with High Specific Energy, *Nano Letters*, 10, 1486, **2010**.

[163] G. Hui, L. Zheng, S. Li, G. Wenhua, G. Wei, C. Lijie, R. Amrita, Q. Weijin, V. Robert, M. A. Pulickel, Synthesis of S-doped graphene by liquid precursor, *Nanotechnology*, 23, 275605, **2012**.

[164] P. Avouris, Graphene: Electronic and Photonic Properties and Devices, *Nano Letters*, 10, 4285, **2010**.

[165] S. Pisana, M. Lazzeri, C. Casiraghi, K. S. Novoselov, A. K. Geim, A. C. Ferrari, F. Mauri, Breakdown of the adiabatic Born–Oppenheimer approximation in graphene, *Nature materials*, 6, 198, **2007**.

[166] Y. Zhang, V. W. Brar, F. Wang, C. Girit, Y. Yayon, M. Panlasigui, A. Zettl, M. F. Crommie, Giant phonon-induced conductance in scanning tunnelling spectroscopy of gate-tunable graphene, *Nature Physics*, 4, 627, **2008**.

[167] P. A. Khomyakov, G. Giovannetti, P. C. Rusu, G. Brocks, J. van den Brink, P. J. Kelly, First-principles study of the interaction and charge transfer between graphene and metals, *Physical Review B*, 79, 195425, **2009**.

[168] M. Vanin, J. J. Mortensen, A. K. Kelkkanen, J. M. Garcia-Lastra, K. S. Thygesen, K. W. Jacobsen, Graphene on metals: A van der Waals density functional study, *Physical Review B*, 81, 081408, **2010**.

[169] J. Park, S. B. Jo, Y.-J. Yu, Y. Kim, J. W. Yang, W. H. Lee, H. H. Kim, B. H. Hong, P. Kim, K. Cho, K. S. Kim, Single-Gate Bandgap Opening of Bilayer Graphene by Dual Molecular Doping, *Advanced Materials*, 24, 407, **2012**.

[170] J. W. Yang, G. Lee, J. S. Kim, K. S. Kim, Gap Opening of Graphene by Dual FeCl3-Acceptor and K-Donor Doping, *The Journal of Physical Chemistry Letters*, 2, 2577, **2011**.

[171] H. Ma, O. Acton, D. O. Hutchins, N. Cernetic, A. K. Y. Jen, Multifunctional phosphonic acid self-assembled monolayers on metal oxides as dielectrics, interface modification layers and semiconductors for low-voltage high-performance organic field-effect transistors, *Physical Chemistry Chemical Physics*, 14, 14110, **2012**.

[172] J. Zou, C.-Z. Li, C.-Y. Chang, H.-L. Yip, A. K. Y. Jen, Interfacial Engineering of Ultrathin Metal Film Transparent Electrode for Flexible Organic Photovoltaic Cells, *Advanced Materials*, 26, 3618, **2014**.

[173] S. K. Hau, H.-L. Yip, O. Acton, N. S. Baek, H. Ma, A. K. Y. Jen, Interfacial modification to improve inverted polymer solar cells, *Journal of Materials Chemistry*, 18, 5113, **2008**.

[174] A. Abrusci, S. D. Stranks, P. Docampo, H.-L. Yip, A. K. Y. Jen, H. J. Snaith, High-Performance Perovskite-Polymer Hybrid Solar Cells via Electronic Coupling with Fullerene Monolayers, *Nano Letters*, 13, 3124, **2013**.

[175] Y. Zang, C.-Z. Li, C.-C. Chueh, S. T. Williams, W. Jiang, Z.-H. Wang, J.-S. Yu, A. K. Y. Jen, Integrated Molecular, Interfacial, and Device Engineering towards High-Performance Non-Fullerene Based Organic Solar Cells, *Advanced Materials*, 26, 5708, **2014**.

[176] N. Beaumont, I. Hancox, P. Sullivan, R. A. Hatton, T. S. Jones, Increased efficiency in small molecule organic photovoltaic cells through electrode modification with self-assembled monolayers, *Energy & Environmental Science*, 4, 1708, **2011**.

[177] Y. Zhao, L. Duan, D. Zhang, G. Dong, J. Qiao, L. Wang, Y. Qiu, Systematic Investigation of Surface Modification by Organosiloxane Self-Assembled on Indium–Tin Oxide for Improved Hole Injection in Organic Light-Emitting Diodes, *ACS Applied Materials & Interfaces*, 6, 4570, **2014**.

[178] J. S. Park, B. R. Lee, J. M. Lee, J.-S. Kim, S. O. Kim, M. H. Song, Efficient hybrid organic-inorganic light emitting diodes with self-assembled dipole molecule deposited metal oxides, *Applied Physics Letters*, 96, 243306, **2010**.

[179] S. G. J. Mathijssen, P. A. van Hal, T. J. M. van den Biggelaar, E. C. P. Smits, B. de Boer, M. Kemerink, R. A. J. Janssen, D. M. de Leeuw, Manipulating the Local Light Emission in Organic Light-Emitting Diodes by using Patterned Self-Assembled Monolayers, *Advanced Materials*, 20, 2703, **2008**.

[180] J. G. C. Veinot, T. J. Marks, Toward the Ideal Organic Light-Emitting Diode. The Versatility and Utility of Interfacial Tailoring by Cross-Linked Siloxane Interlayers, *Accounts of Chemical Research*, 38, 632, **2005**.

[181] S. A. DiBenedetto, A. Facchetti, M. A. Ratner, T. J. Marks, Molecular Self-Assembled Monolayers and Multilayers for Organic and Unconventional Inorganic Thin-Film Transistor Applications, *Advanced Materials*, 21, 1407, **2009**.

[182] S. Yogev, R. Matsubara, M. Nakamura, U. Zschieschang, H. Klauk, Y. Rosenwaks, Fermi Level Pinning by Gap States in Organic Semiconductors, *Physical Review Letters*, 110, 036803, **2013**.

[183] D. Liu, X. Xu, Y. Su, Z. He, J. Xu, Q. Miao, Self-Assembled Monolayers of Phosphonic Acids with Enhanced Surface Energy for High-Performance Solution-Processed N-Channel Organic Thin-Film Transistors, *Angewandte Chemie International Edition*, 52, 6222, **2013**.

[184] D. Liu, Z. He, Y. Su, Y. Diao, S. C. B. Mannsfeld, Z. Bao, J. Xu, Q. Miao, Self-Assembled Monolayers of Cyclohexyl-Terminated Phosphonic Acids as a General Dielectric Surface for High-Performance Organic Thin-Film Transistors, *Advanced Materials*, 26, 7190, **2014**.

[185] M. Halik, A. Hirsch, The Potential of Molecular Self-Assembled Monolayers in Organic Electronic Devices, *Advanced Materials*, 23, 2689, **2011**.

[186] H.-T. Rong, S. Frey, Y.-J. Yang, M. Zharnikov, M. Buck, M. Wühn, C. Wöll, G. Helmchen, On the Importance of the Headgroup Substrate Bond in Thiol Monolayers: A Study of Biphenyl-Based Thiols on Gold and Silver, *Langmuir*, 17, 1582, **2001**.

[187] F. Garnier, R. Hajlaoui, A. El Kassmi, G. Horowitz, L. Laigre, W. Porzio, M. Armanini, F. Provasoli, Dihexylquaterthiophene, A Two-Dimensional Liquid Crystal-like Organic Semiconductor with High Transport Properties, *Chemistry of Materials*, 10, 3334, **1998**.

[188] S. A. Ponomarenko, O. V. Borshchev, T. Meyer-Friedrichsen, A. P. Pleshkova, S. Setayesh, E. C. P. Smits, S. G. J. Mathijssen, D. M. de Leeuw, S. Kirchmeyer, A. M. Muzafarov, Synthesis of Monochlorosilyl Derivatives of Dialkyloligothiophenes for Self-Assembling Monolayer Field-Effect Transistors, *Organometallics*, 29, 4213, **2010**.

[189] J. Noh, H. S. Kato, M. Kawai, M. Hara, Surface and Adsorption Structures of Dialkyl Sulfide Self-Assembled Monolayers on Au(111), *The Journal of Physical Chemistry B*, 106, 13268, **2002**.

[190] Y. S. Park, A. C. Whalley, M. Kamenetska, M. L. Steigerwald, M. S. Hybertsen, C. Nuckolls, L. Venkataraman, Contact Chemistry and Single-Molecule Conductance: A Comparison of Phosphines, Methyl Sulfides, and Amines, *Journal of the American Chemical Society*, 129, 15768, **2007**.

[191] D. O. Hutchins, O. Acton, T. Weidner, N. Cernetic, J. E. Baio, G. Ting, D. G. Castner, H. Ma, A. K. Y. Jen, Spin cast self-assembled monolayer field effect transistors, *Organic Electronics*, 13, 464, **2012**.

[192] Q.-J. Sun, Z. Xu, S.-L. Zhao, F.-J. Zhang, L.-Y. Gao, Y.-S. Wang, The performance improvement in pentacene organic thin film transistors by inserting C60/MoO3 ultrathin layers, *Synthetic Metals*, 160, 2239, **2010**.

[193] M. Kitamura, Y. Kuzumoto, S. Aomori, M. Kamura, J. H. Na, Y. Arakawa, Threshold voltage control of bottom-contact n-channel organic thin-film transistors using modified drain/source electrodes, *Applied Physics Letters*, 94, 083310, **2009**.

[194] S. Das, H.-Y. Chen, A. V. Penumatcha, J. Appenzeller, High Performance Multilayer MoS2 Transistors with Scandium Contacts, *Nano Letters*, 13, 100, **2013**.

[195] M. Tachibana, K. Yoshizawa, A. Ogawa, H. Fujimoto, R. Hoffmann, Sulfur−Gold Orbital Interactions which Determine the Structure of Alkanethiolate/Au(111) Self-Assembled Monolayer Systems, *The Journal of Physical Chemistry B*, 106, 12727, **2002**.

[196] D. O. Bellisario, A. D. Jewell, H. L. Tierney, A. E. Baber, E. C. H. Sykes, Adsorption, Assembly, and Dynamics of Dibutyl Sulfide on Au{111}*, The Journal of Physical Chemistry C*, 114, 14583, **2010**.

[197] H.-J. Himmel, A. Terfort, C. Wöll, Fabrication of a Carboxyl-Terminated Organic Surface with Self-Assembly of Functionalized Terphenylthiols: The Importance of Hydrogen Bond Formation*, Journal of the American Chemical Society*, 120, 12069, **1998**.

[198] D. A. Outka, J. Stöhr, J. P. Rabe, J. D. Swalen, The orientation of Langmuir–Blodgett monolayers using NEXAFS*, The Journal of Chemical Physics*, 88, 4076, **1988**.

[199] Y. Xu, R. Gwoziecki, I. Chartier, R. Coppard, F. Balestra, G. Ghibaudo, Modified transmission-line method for contact resistance extraction in organic field-effect transistors*, Applied Physics Letters*, 97, 063302, **2010**.

[200] Y. Zhang, H. Dong, Q. Tang, Y. He, W. Hu, Mobility dependence on the conducting channel dimension of organic field-effect transistors based on single-crystalline nanoribbons*, Journal of Materials Chemistry*, 20, 7029, **2010**.

VITA

Nathan Cernetic was born in Phoenix, AZ. In 2010 he earned a Bachelor of Science in Materials Science and Engineering from Arizona State University. In 2016 he earned a Doctor of Philosophy at the University of Washington in Materials Science and Engineering.